Title

Insights into Acidity-Driven Surface Chemistry and Kinetics of Aqueous Aerosols

Author

Angle, Kyle

Publication Date

2022

Peer reviewed|Thesis/dissertation

UNIVERSITY OF CALIFORNIA SAN DIEGO

Insights into Acidity-Driven Surface Chemistry and Kinetics of Aqueous Aerosols

A Dissertation submitted in partial satisfaction of the requirements
for the degree Doctor of Philosophy

in

Chemistry

by

Kyle Angle

Committee in charge:

Professor Vicki Grassian, Chair
Professor Lihini Aluwihare
Professor Robert Pomeroy
Professor Amitabha Sinha

2022

The Dissertation of Kyle Angle is approved, and it is acceptable in quality and form for publication on microfilm and electronically.

University of California San Diego

2022

DEDICATION

To my family, Kelsey, Jenny, and Jim, for their continuous love and support.

EPIGRAPH

The ultimate test of a moral society is the kind of world that it leaves to its children.

Dietrich Bonhoeffer

TABLE OF CONTENTS

LIST OF FIGURES

LIST OF TABLES

ACKNOWLEDGEMENTS

I want to thank my advisor, Dr. Vicki Grassian, for taking me on for an early summer rotation and for supporting me throughout my doctoral work. Dr. Grassian has pushed me while also giving me space to grow as a scientist. She is always very fast in responding to inquiries and requests for meetings, and I know my work is important to her. She has also been supportive of my outreach efforts and allowing me to be an instructor of record in the summer. I am grateful for the repeated confidence she has expressed in my future career and count myself fortunate to have had her as my scientific advisor and mentor.

I would like to thank my committee for their comments and questions pertaining to my research. I thank Dr. Sinha and Dr. Aluwihare for teaching me about quantum mechanics and marine chemistry, respectively. I especially thank Dr. Pomeroy for personal advice, serving as my mentor for summer teaching, connecting me with outreach activities, and allowing me to use the auto titrator in his lab to test out a potential project. I also thank Dr. Weare, now retired, for his helpful input on the use of convention in defining pH.

I thank my parents for endless support in so many ways. They have provided their love and encouragement throughout my time at UCSD. I was always greatly refreshed after they visited me here and talking with them each weekend helped keep me going. I also thank my sister for all of her advice and for making me feel heard. I always knew I could go to her with any problem, and she reminded me to laugh every day and keep my feet on the ground.

I owe thanks to the entire Grassian group for their help and kindness. I especially thank Stephanie Mora Garcia and Deborah Kim for their friendship and encouragement from our early summer rotation together through the end. It strengthened me to know I always had allies. I also

thank Ellen Coddens and Man Luo for their mentorship and for showing me how to use research instruments. I thank Mariana Rivas for helpful discussions and for suggesting I study lactic acid for the research presented in Chapter 5. I thank Victor Or for training me on the MOUDI and his advice in applying for the ARCS scholarship. Finally, I thank all my mentees, including Erin Neal, Christopher Nowak, Aakash Davasam, "Suds" Srinivasan, Mahum Farhan, Hannah Primiano, Alexis Wright, and Justin Wang for their kindness and for staying adaptable as we navigated complex scientific projects.

Thank you to the Achievement Rewards for College Scientists (ARCS) Foundation, Carol and George Lattimer, and the UCSD Department of Chemistry & Biochemistry for awarding me personal funds in support of my research career.

I owe gratitude to the Center for Aerosol Impacts on Chemistry of the Environment for connecting me with many different scientists and enabling collaborations. In particular I would like to thank Dr. Chris Lee for support, and Dr. Gil Nathanson and Dr. Heather Allen for their positive feedback on my presentations and for helpful discussions. I also thank Dr. Jeanette Starpine for organizing numerous outreach opportunities and for personal advice.

Thank you to all of my GCF friends for making this journey enjoyable and thank you Greg Ehlert for spiritual counseling and ongoing support.

Chapter 3, in part, is a reprint of the material published by The Proceedings of the National Academy of Sciences of the United States of America in: Angle, Kyle; Crocker, Daniel; Simpson, Rebecca; Mayer, Kathryn; Garofalo, Lauren; Moore, Alexia; Mora Garcia, Stephanie; Or, Victor; Srinivasan, Sudarshan; Farhan, Mahum; Sauer, Jon; Lee, Christopher; Pothier, Matson; Farmer, Delphine; Martz, Todd; Bertram, Timothy; Cappa, Christopher; Prather, Kimberly; Grassian, Vicki, Acidity Across the Interface from the Ocean Surface to Sea

Spray Aerosols in 2020. The dissertation author was the primary investigator and author of this paper.

Chapter 4, in part, is a reprint of the material published by Environmental Science and Technology in: Angle, Kyle; Neal, Erin; Grassian, Vicki, Enhanced Rates of Transition-Metal-Ion-Catalyzed Oxidation of S(IV) in Aqueous Aerosols: Insights into Sulfate Aerosol Formation in the Atmosphere in 2021. The dissertation author was the primary investigator and author of this paper.

Chapter 5, in part, is a reprint of material submitted to Environmental Science: Atmospheres in: Angle, Kyle; Nowak, Christopher; Grassian, Vicki, Organic Acid Evaporation Kinetics From Aqueous Aerosols: Implications for Aerosol Buffering Capacity in the Atmosphere in 2022. The dissertation author was the primary investigator and author of this paper.

Chapter 6, in full, contains original research that will be submitted for publication to Communications Chemistry in: Angle, Kyle; Li, Meng; Grassian, Vicki, Direct Quantification of Nitrate and Chloride Depletion Kinetics from Single Levitated Aerosols in 2023. The dissertation author was the primary investigator and author of this paper.

Chapter 7, in part, is a reprint of the material published by the Journal of Physical Chemistry Letters in: Angle, Kyle; Nowak, Christopher; Davasam, Aakash; Dommer, Abigail; Wauer, Nicholas; Amaro, Rommie; Grassian, Vicki, Amino Acids Are Driven to the Interface by Salts and Acidic Environments in 2022. The dissertation author was the primary investigator and author of this paper.

VITA

2014 Bachelor of Science in Chemistry, Truman State University

2018 Master of Science in Chemistry, University of California San Diego

2022 Doctor of Philosophy in Chemistry, University of California San Diego

PUBLICATIONS

Abayaweera, Gayani; Wang, Hongwang; Shrestha, Tej; Yu, Jing; **Angle, Kyle**; Thapa, Prem; Malalasekera, Aruni; Maurmann, Leila; Troyer, Deryl; Bossmann, Stefan. (2017). Synergy of Iron Chelators and Therapeutic Peptide Sequences Delivered via a Magnetic Nanocarrier. *Journal of Functional Biomaterials*, 8 (3), 23.

Coddens, Ellen; **Angle, Kyle**; Grassian, Vicki. (2019). Titration of Aerosol pH through Droplet Coalescence. *Journal of Physical Chemistry Letters*, 10 (15), 4476.

Luo, Man; Wauer, Nicholas; **Angle, Kyle**; Dommer, Abigail; Song, Meishi; Nowak, Christopher; Amaro, Rommie; Grassian, Vicki. (2020). Insights into the Behavior of Nonanoic Acid and its Conjugate Base at the Air/Water Interface through a Combined Experimental and Theoretical Approach. *Chemical Science*, 11 (39), 10647.

Angle, Kyle; Crocker, Daniel; Simpson, Rebecca; Mayer, Kathryn; Garofalo, Lauren; Moore, Alexia; Mora Garcia, Stephanie; Or, Victor; Srinivasan, Sudarshan; Farhan, Mahum; Sauer, Jon; Lee, Christopher; Pothier, Matson; Farmer, Delphine; Martz, Todd; Bertram, Timothy; Cappa, Christopher; Prather, Kimberly; Grassian, Vicki. (2020). Acidity Across the Interface from the Ocean Surface to Sea Spray Aerosols. *Proceedings of the National Academy of Sciences of the United States of America*, 118 (2), e2018397118.

Angle, Kyle; Neal, Erin; Grassian, Vicki. (2021). Enhanced Rates of Transition-Metal-Ion-Catalyzed Oxidation of S(IV) in Aqueous Aerosols: Insights into Sulfate Aerosol Formation in the Atmosphere. *Environmental Science and Technology* 55 (15), 10291.

Angle, Kyle; Grassian, Vicki; Ault, Andrew. (2022). The Rapid Acidification of Sea Spray Aerosols. *Physics Today* 75 (1), 58.

Angle, Kyle; Nowak, Christopher; Davasam, Aakash; Dommer, Abigail; Wauer, Nicholas; Amaro, Rommie; Grassian, Vicki. (2022). Amino Acids Are Driven to the Interface by Salts and Acidic Environments. *Journal of Physical Chemistry Letters* 13 (12), 2824.

FIELDS OF STUDY

Major field: Chemistry

Studies in crystallization, NMR kinetics, and organic synthesis
Professors Amy Fuller and Timothy Humphry

Studies in biochemistry
Professor Stefan Bossmann

Studies in inorganic chemistry
Professor Janet Blumel

Studies in analytical and atmospheric chemistry
Professor Vicki Grassian

ABSTRACT OF THE DISSERTATION

Insights into Acidity-Driven Surface Chemistry and Kinetics of Aqueous Aerosols

by

Kyle Angle

Doctor of Philosophy in Chemistry

University of California San Diego, 2022

Professor Vicki Grassian, Chair

Atmospheric aerosols are generated by the millions globally from the bursting of ocean bubbles, the action of wind on dust, burning processes, and many other sources. Aerosol particles have high surface area to volume ratios and typically contain chemicals in significantly greater concentrations compared to the bulk source. From serving as the seeds for clouds to promoting multiphase chemistry and interacting with cells, aerosols have profound impacts on

the climate and human health. Among the many properties of aerosols, one of the most important is pH, a measure of the particle's acidity. Low pH aerosols have detrimental effects on the lungs, and many atmospheric transformations exhibit pH dependence. Although aerosol pH is critically important, it is challenging to measure due to the very small volumes individual aerosols occupy. As a result, prior to the work presented here, the pH of nascent sea spray aerosol (the largest source of aqueous particles globally) was unknown. Here, a novel method for the determination of aerosol pH and its application to the measurement of sea spray aerosol acidity is presented. It is found that, in just two minutes, these aerosols are acidified to pH levels ranging from 2 to 4 depending on particle size. Following this result, several key causes and effects of aerosol pH are discussed. Acidity is shown to impact the extent of acceleration of S(IV) oxidation in aerosols, an important chemical reaction for the fate of sulfur dioxide emissions and air quality. A unique type of buffering to aerosols is presented next, where the titration of the particle results in a decrease in the organic content of the aerosol, instead of a drop in pH, due to partitioning of acids. Following this, the kinetics of nitrate and chloride depletion for single aerosols is shown for the first time. These processes both modulate aerosol pH and change particle hygroscopicity, which is a central parameter for atmospheric cloud formation. Finally, the link between aerosol acidity and surface chemistry is shown by an exploration of the pH-dependent surface propensity of amino acids in aqueous environments. Together, these studies shed light on the drivers of aerosol pH and the kinetics of critical aerosol-phase reactions. Ultimately, this research improves understanding of the complex ocean-climate system and how invisible particles present health challenges for populations globally.

CHAPTER 1 INTRODUCTION

1.1 Atmospheric Aerosols

1.1.1 Physical Properties

Aerosols are suspensions of solids or liquids in a gas phase. In the atmosphere, air is the gas phase, and aerosols can vary in size from diameters of a few nanometers to several hundred microns. Due to this small size, individual aerosols are invisible to the human eye. Accumulations of aerosols, however, can be observed due to their scattering and absorption of radiation, particularly solar rays. An observer on the beach facing the ocean may notice that the air in the immediate surroundings appears clear, while the air in the distance to the left and right appears hazy. This is due in part to the presence of sea spray aerosols (hereafter, SSA).

SSA are generated when waves break and bubbles burst in the ocean.[1,2] When a bubble breaks at the sea surface, the energy associated with the surface tension of water can be converted to kinetic energy that creates a jet directed up into the atmosphere. In addition, the resulting gap in air from the space the bubble formerly occupied is filled by a rush of water, which can reinforce the jet. Ultimately, somewhere between one and ten aerosols are usually produced, with smaller bubbles producing more aerosols.[3] Since these aerosols originate from a jet of water, they have been termed "jet drops". Jet drops can vary in size, producing both supermicron (> 1 μm diameter) and submicron (< 1 μm diameter) SSA.[4]

The bursting of a bubble film also creates smaller SSA that have been termed "film drops". A proposed mechanism for film drop formation has been described in depth.[2] Generally, film drops are submicron and are larger in number than jet drops, such that the number concentration of SSA peaks near 200 nm. In addition to jet and film drops, when wind speeds are sufficiently high, spume

drops can also be produced.[5] These are the largest of SSA particles, often > 8 μm in diameter, and are the result of the mechanical action of wind on wave crests. It has been shown that the maximum number of spume drops may occur between wind speeds of 16 to 22 meters per second, since at higher speeds, the spume drops may be scavenged by larger seawater droplets.[6]

Together, jet, film, and spume drops compose SSA. SSA are the largest component of marine aerosols and are the largest natural source of aerosols.[7,8] It is important to know the size of SSA particles, as this will impact their interaction with radiation. In general, aerosols can change size in response to relative humidity (hereafter, RH). When SSA are first formed in the marine boundary layer, the surrounding RH is high, likely between 70 and 90%.[9] When the SSA travel through the atmosphere, they may decrease in size as RH decreases.[10] At low RH, the viscosity can increase and the phase state can transition from liquidlike to semisolid-like and even solidlike.[11,12] Heterogeneous aerosols can also have varying mixing states, such as a core-shell morphology, with a hydrophobic exterior and hydrophilic interior.[13] As a final note on physical properties, although a still and homogeneous aerosol may be assumed to be spherical, the action of wind or presence of hydrophobic components could distort an aerosol's shape.[14,15]

1.1.2 Chemical Properties

Although SSA were once called "sea salt aerosols", they are composed of far more than water and salts. In particular, organic molecules are enriched in SSA.[16] These include biogenic molecules, particularly components of microbial lipids, saccharides, and amino acids.[17–19] There has even been detection of enzymes that retain activity in SSA.[20] In general, molecules with higher surface propensity are more likely to be enriched, and ions are more likely to be transferred if they are paired with a molecule such as an acid.[21,22] Enrichment is often calculated by computing the ratio of the analyte to Na^+ in both the aerosol phase and bulk seawater.[18] It is important to

remember that all aerosol components become more concentrated as an aerosol loses water, so in another sense, Na^+ itself is concentrated in SSA compared to the sea. Due to this concentration, as well as substantial enrichment of components such as Mg^{2+} and particularly Ca^{2+}, the ionic strength of SSA can exceed 5 m.[23,24] In short, aerosols are highly concentrated environments.

Aerosols dynamically exchange chemicals with the surrounding atmosphere. Molecules can evaporate from aerosols as gases, and gases can condense onto aerosols. Together, these processes are termed "partitioning". Partitioning is highly important for predicting aerosol chemical composition and the formation of new organic aerosols from existing aerosols, which are called Secondary Organic Aerosols (SOA).[25] At equilibrium, partitioning is controlled by Henry's Law, given in equation 1.1:

$$c = H * p \tag{1.1}$$

Here, c is the concentration of the analyte in the aqueous phase, H is the constant of proportionality, and p is the partial pressure of the analyte in the gas phase. Henry's Law constants have been compiled by Sander, who notes that different conventions are used in various publications (in particular, H is sometimes placed on the other side of the equation, so the units must be carefully checked).[26] While equation 1.1 is simple, the prediction of aerosol concentrations given a surrounding atmosphere is not. Gases can be salted in or salted out, and this effect is non-negligible for the high ionic strengths of aerosols.[27–29] Additionally, for highly viscous aerosols, diffusion limitation may prevent aerosols from reaching the analyte concentrations predicted by equation 1.1.[30]

The nature of chemical reactions within aerosols is discussed later in this chapter. Next, we consider one of the most important chemical properties of aerosols, which is pH.

1.2 Aerosol Acidity

1.2.1 Definitions of pH

Acidity values span many orders of magnitude in systems of interest. As a result, the pH scale is used, where pH is the negative base 10 logarithm of proton concentration. This scale, while useful, has led to a number of misconceptions about acidity. For example, some illustrations imply pH is restricted to the 0 to 14 range, and misinterpretations of the leveling effect have reinforced this incorrect assumption. The fact that pH can be outside this range is particularly relevant to aerosol pH, which has repeatedly been calculated to be < 0.[31] It is also sometimes assumed that all water has a pH of exactly 7. In fact, the pH of water is near 7 at temperatures near 298 K, but the dissolution of atmospheric CO_2 into water and the subsequent formation of carbonic acid can lower the pH of water below 6. Unfortunately, due to the logarithmic nature of the pH scale, the importance of small changes in pH units can be overlooked. For example, a decrease in ocean pH from 8.2 to 8.1 represents a ca. 23% increase in acidity. Finally, there are a few technical problems with the quantification of "acidic proton concentration". Individual ion activities cannot be measured, so they must be defined by a convention (such as the average activity of a cation-anion pair e.g. H^+ and Cl^-), however, the choice of convention becomes unclear when the system has a substantial organic fraction.[32,33] It may also be misleading to refer to this as "proton" activity, when the structure may be an Eigen-type, Zundel-type, or even $H_{13}O_6^+$.[34] These last two issues, while important to basic science, are beyond the scope of this chapter.

Additional confusion around pH calculations stem from different definitions that all use the term "pH". Since the activity of a chemical species is sensitive to ionic strength, it is generally agreed that activities, instead of concentrations, should be used. Even within the domain of activities, however, at least three definitions are in use.[35]

$$pH_x = -\log (f_H x_H) \quad (1.2)$$

$$pH_c = -\log (\frac{\gamma_H c_H}{c^o}) \quad (1.3)$$

$$pH_m = -\log (\frac{\gamma_H m_H}{m^o}) \quad (1.4)$$

In order, these equations represent pH in terms of mole fraction, molarity, and molality. Here, f_H is the mole fraction activity coefficient, x_H is the mole fraction, y_H is the molarity-based activity coefficient, c_H is the molarity, γ_H is the molality-based activity coefficient, and m_H is the molality, all pertaining to the acidic proton. The quantities c^o and m^o represent unity molarity and molality, respectively, and are used to prevent the log quantity from having units.

The differences between equations 1.2 to 1.4 are non-trivial. For example, when water is the only solvent, pH_m is by definition 1.74 units lower than pH_x.[35] Conversion between molality and molarity becomes more substantial at higher concentrations, since molarity has the volume of the solution in the denominator while molality has the mass of only the *solvent* in the denominator. Therefore, it is highly recommended that the pH definition is specified clearly. In this dissertation, except where otherwise indicated, pH_m is used.

1.2.2 Direct Measurement of Aerosol pH

Individual aerosol particles have volumes on the order of femtoliters to picoliters, making measurement of acidity challenging. Collection of aerosols onto filters and measurement of acidity at a later time should be avoided due to the presence of acidic atmospheric species that can interact with the sample, as well as potential degassing from the sample. An early measure of SSA pH by Winkler involved collecting SSA into a known volume of water and calculating acidity based on dilution.[36] He found smaller SSA to be more acidic.[36,37] In addition to H^+ concentration, the concentrations of other ions can be obtained when aerosols are collected into controlled amounts of water, in a process sometimes termed particle-into-liquid sampling (PILS). While PILS can give

a useful measure of the "strong acidity" (i.e. the sum of free H^+, sulfuric acid, and bisulfate), the original liquid water content of the aerosol is not captured, precluding determination of H^+ activity.[38]

The influence of pH on indicator dyes has long been used for titrations and pH paper measurements of bulk solutions. This same principle was applied to haze, cloud, and fog droplets semi-quantitatively, and it was found that smaller aerosols were more acidic.[39] The process has been improved upon by various investigators.[40–43] A discussion of the use of pH paper for pH measurement is given in Chapter 2. The interaction of acidic particles with a substrate also occurs when aerosols are deposited on a polymer that degrades at low pH. This fact has been combined with atomic force microscopy to give another method for aerosol pH measurement.[44]

Spectroscopy can also be used to measure aerosol pH in-situ. The ratio of conjugate acid and base peaks in a Raman spectrum can allow calculation of acidity if the pK_a is known.[45] This method was applied to single, levitated particles, illustrating that the pH of an individual aerosol can be tracked through coalescence events and hence controlled.[46] Due to the high concentration of ions in aerosols, it is necessary to go beyond the Debye-Hückel equation and use an approach such as Specific Ion Interaction Theory (SIIT) or the Pitzer equations to determine activities of water, H^+, and the conjugate acid and base. This can be accomplished through the use of models which are discussed further in the next section. The total concentration of the aerosol should also be known if bulk calibration curves are used for aerosol pH calculations.[47] Other uses of spectroscopy include surface-enhanced Raman spectroscopy (SERS) in combination with nanoparticles and fluorescence spectroscopy with quantum dots.[48–50] Different methods span different pH ranges, but it is important to note that H^+ activity is sensitive to the chemical matrix and in particular may be altered by the presence of additional surfaces or ions. Further, any addition

to aerosols that changes hygroscopicity will impact the equilibrium water content, which in turn can change pH via dilution or concentration. For methods where nanoparticles are added to the aerosols, the heat generated at the nanoparticle's surface can increase evaporation, causing additional perturbations to the local chemical environment.[51]

1.2.3 Model Calculations of Aerosol pH

Various models have been developed to assist in the determination of aerosol pH using gas and/or aerosol-phase concentrations as inputs. These models are based on equilibrium, meaning that their applicability to metastable aerosols would not be perfect. In addition, there is no explicit consideration of the aerosol surface or size effects, so processes such as chloride and nitrate depletion (discussed in Chapter 6) are not included. Nevertheless, these models are highly useful for predicting activities, water content, and pH in nonideal solutions and aerosols.

The simplest model for inferring aerosol pH is to sum up all other cations and anions and assume that the missing cations are all H^+. This is referred to as the ion balance method, and is prone to inaccuracies of several pH units within error propagation of typical measurement uncertainties.[52] Thermodynamic models that have constraints from gas phase inputs perform significantly better.[31,52] Among the popular models are the E-AIM, ISORROPIA II, and ACCENT. E-AIM (Extended Aerosol Inorganic Model) can perform single or batch calculations for several different combinations of common inorganic ions.[53–55] Organic species can also be included if the appropriate parameters are known. Electrolyte activity coefficients are calculated via the PSC (Pitzer, Simonson, and Clegg) equations, and uncharged, dissolved organic activity coefficients can be calculated using Raoult's law, the Redlich-Kister equation, or UNIFAC (UNIQUAC Functional group Activity Coefficients).[56,57] ISORROPIA II (ISORROPIA is not an acronym, it comes from the Greek word for equilibrium) performs calculations to partition nitric acid and

ammonia between the aerosol and gas phase, which both impact aerosol pH, and like E-AIM can work at varying temperature and RH conditions.[58] ACCENT (Atmospheric Composition Change the European Network of excellence) calculations can be performed on the same website as E-AIM and, while fewer options are present, the input of CO_3^{2-} is possible. Various comparisons between the performances of the models have been published.[31,59,60] Whether great care should be taken in selecting one model instead of another depends on whether the precise pH of the system needs to be known, but in general, these models highlight the extent to which activity is altered in highly concentrated solutions. In the words of George Box, "All models are wrong but some are useful."[61]

1.2.4 Aerosol Acidity in the Atmosphere

Atmospheric aerosols are typically acidic. Measurements of ambient aerosols include both fresh and aged aerosols, making isolation of nascent aerosol pH challenging.[62] There are a very large number of reports of aged aerosol, however, and these typically span pH -1 to 5.[31,63–70] Atmospheric aerosol lifetimes are sensitive to a number of factors, and are typically longer for smaller particles, which can span from days to weeks.[71] During this time, acidification occurs via titration with acidic gases such as nitric acid, partitioning of ammonia, photochemical reactions, and loss of water. One might assume that interaction with atmospheric bases such as ammonia would raise aerosol pH. Due to multiphase buffering, however, the ammonia/ammonium system actually maintains aerosol pH at acidic levels, in contrast to bulk solutions.[70] Anthropogenic pollution generally leads to more acidic particles.[72] Aerosol pH also can be seasonal with higher pH values but also greater sensitivity to nitric acid found in the winter due to changes in water content.[73] The seasonality is also sensitive to urban heat islands, and temperature changes in

general.[74] Ultimately, the pH evolution of aerosols is important, as this impacts health, climate, and atmospheric chemistry as described in the next three sections.

1.2.5 Health Impacts of Aerosol Acidity

Aerosol particles are inhaled by the thousands and can have significant impacts on lung health. In general, smaller aerosols are considered more harmful as they can penetrate further into the lungs.[75] Once in the lungs, more acidic particles can cause both oxidative stress via metal dissolution and toxic effects from aerosol organic components.[76,77] Since smaller aerosols are generally more acidic, submicron aerosols are particularly harmful. It is difficult to quantify the total impact that acidic aerosols have on human health, given that many areas lack sufficient air quality data and that data is often reported as $PM_{2.5}$ (sum of all particles with diameters smaller than 2.5 μm). Nevertheless, a study drawing from $PM_{2.5}$ data estimated that there are over 3 million premature deaths each year due to air pollution.[78]

Recently, a great deal of attention has been given to the pH-dependence of virus viability, given that aerosols transporting coronaviruses is a major cause of infections. This research is recent enough, and pertains to such a sensitive issue, that it should be interpreted with caution. One study reported more inactivation of SARS-CoV-2 at $pH < 5$.[79] The extent to which respiratory droplets are acidified is under debate, but size and the amount of bicarbonate appear to be important factors.[80,81] In any case, with pH-dependent side chains on the amino acids that compose the spike protein, aerosol acidity is a key parameter for fully understanding this mode of virus transmission. Finally, it is worth noting that low pH could change protein folding at the air-water interface, and given that aerosols have high surface to volume ratios, this may be an important consideration for biological activity in aerosols.[82]

1.2.6 Climate Impacts of Aerosol Acidity

The pH of aerosols also impacts the health of the planet. Global radiation balance is influenced by the extent of cloud formation in the atmosphere, as clouds can increase albedo and decrease the amount of absorbed solar energy. Aerosols serve as the seed for clouds, and the particles that do so are termed cloud condensation nuclei, or CCN. When the aerosol serves as the formation site for an ice crystal, it is called an ice nucleating particle, or INP. CCN has been tentatively positively correlated with aerosol pH, possibly due to the dependence of both of these factors on liquid water content.[83] For cloud water, neutral pH appears to correspond to the optimal INP surface for α-alumina.[84] The same may be true for aerosols. Together, these reports imply the possibility that a more acidic atmosphere may have less cloud formation, but much more research on this topic is warranted.

Aerosol pH also impacts the contents and formation of atmospheric aerosols. High acidity can promote increased brown carbon formation, and brown carbon can absorb solar radiation (including near the UV region).[85] Low initial pH also has the potential to increase SOA formation, organosulfate products, phase separation, viscosity, and semisolid to solid phase transitions.[86,87] It has also been recently shown that protonation state is important when new particles are formed from acid-base chemistry between sulfuric acid and amines or amino acids.[88] In fact, protonation state is important for chemistry in general, and several important reactions are detailed in the next section.

1.2.7 Chemical Impacts of Aerosol Acidity

One key atmospheric process with unique pH sensitivity is the oxidation of S(IV). This reaction is described in depth in Chapter 4. Briefly, SO_2 (g) or an aqueous form of S(IV) can be oxidized into inorganic sulfate, potentially changing the pH and ionic strength of the medium. This

process has been the focus of renewed research interest when it was found that established bulk kinetics significantly underestimated the amount of sulfate formed during haze events in megacities such as Beijing.[89] The kinetic order of H^+ has been suggested at a variety of values (including non-integer values) for different pH ranges; for example, an order of -2 was proposed at low ionic strength in the pH range 4.1 to 6.3.[90] Another critical pH dependence is whether SO_2 (g) can be oxidized directly at the air-water interface. This pathway is only available below pH 4.[91] More details are given in Chapter 4, but clearly, aerosol pH is key to the fate of SO_2 (g).

Aerosol acidity can also impact the rates of parallel reaction pathways. In the case of glycolaldehyde reacting with atmospheric amines and ammonium sulfate, pH controls whether sugar-like trimers and hexamers or nitrogen-containing oligomers are the major product.[92] For the aforementioned sulfate formation process, oxidation by H_2O_2 appears to be the dominant pathway at higher pH, while transition metal ion catalyzed oxidation is more prevalent at low pH.[93] Naturally, acid-catalyzed chemistry such as the hydrolysis of organonitrates is also accelerated by acidity.[94] Additional examples of pH impacts include the speciation of acids, the solubility or insolubility of metals, and the stability of complexes. Undoubtedly, although aerosol acidity is challenging to measure and constrain in climate models, it is a parameter of utmost importance for atmospheric chemistry.

1.3 Aerosol Kinetics and Thermodynamics

1.3.1 Reaction Acceleration

Aerosols present unique environments for chemistry, particularly with their high surface area to volume ratio. While curvature effects are most important for aerosols smaller than 100 nm in radius, differences in surface tension between bulk solutions and droplets have been observed even for supermicron particles.[95] Additionally, molecules in aerosols have much more frequent

access to the interface compared to bulk systems. This can be quantified in terms of a characteristic length (see Chapter 4), which for aerosols can be the particle diameter while the shortest dimension with surface access can be used for a bulk solution (such as height for a small volume in a petri dish).[96] Increased surface access gives the potential for faster reaction kinetics. For example, the activation energy of some reaction steps may be lower in the reduced solvation environment of the air-water interface. Alternately, the reaction may be promoted by a concentration of uncharged components and radicals near the air water interface while charged inhibitors reside in the aerosol core. Finally, chemical gradients may exist in aerosols, enhancing kinetics through different pH or reagent concentrations at different positions in the aerosol. These gradients may be caused by a differing free energy of surface adsorption in the aerosol, and may be associated with specific molecular orientation at the interface.[97]

Due to these factors, one may expect aerosols to accelerate certain chemical reactions by a few orders of magnitude. Indeed, this has been observed for photochemistry, acid-catalyzed degradation, and many more reactions.[98,99] However, there have also been reports of reactions accelerated by six orders of magnitude, including redox processes which are attributed to a spontaneous electric field at the air-water interface.[100,101] In some cases, these numbers may be artificially high due to factors such as solvent evaporation.[102] In addition, while it has been shown that up to 10^4 elementary charges do not impact the degradation of oleic acid in aerosols, other reactions, particularly redox reactions, could be quite sensitive to particle charge.[103] Therefore, care should be taken in comparing rates from electrospray techniques to dilute bulk kinetics. It is also worth noting that counterexamples exist, and one set of experiments illustrated that a Diels-Alder reaction did not proceed in the aerosol in a way comparable to the bulk.[104]

Reaction acceleration has been discussed in terms of green chemistry, as faster kinetics and minimal use of solvent seem useful for efficient industry production of chemicals. It may also be tempting to connect reaction acceleration to origin of life hypotheses. In both applications, it should be remembered that aerosols generated in labs likely will not match the bulk solution from which they are generated, neither in terms of total concentration nor molar ratio of components. An additional point, particularly pertinent to this dissertation, is that the acidity of the microdroplet surface as well as the pH evolution of evaporating aerosols has not been fully established. Further understanding of fundamental surface science and the behavior of molecules near interfaces is necessary to support progress in research of reaction acceleration.

1.3.2 Surface Propensity

A final important property pertinent to particles is surface propensity. An aerosol that is a homogeneous mixture of fatty acids and water would interact with the surrounding atmosphere differently from one covered with a hydrophobic fatty acid shell. In addition to the usual bulk-phase factors that influence surface propensity, the high salt content of aerosols can further impact surface composition. For nonanoic acid, it was shown that both the protonated and deprotonated forms were more stabilized at the air-water interface by NaCl, with a greater stabilization observed for the anion (deprotonated form) compared to the neutral acid.[105] Since the pK_a of an acid can be calculated from the concentrations of these two forms along with $[H^+]$, this could be taken as a "surface pK_a" that was lower than the bulk pK_a. It is important to distinguish that this does not necessarily mean that nonanoic acid is more likely to give up an acidic proton at the air-water interface, but instead this parameter can be used to characterize the ratio of acid and base present at this boundary. Indeed, some evidence shows that acids and bases can cooperatively enhance total surface concentration.[106]

An important question for many areas of science is whether the air-water interface is more acidic or more alkaline than bulk water. The full discussion is beyond the scope of this dissertation. However, one important idea is to avoid a false dichotomy. It is possible that water's dissociation products are *both* enhanced at the air-water interface, making the surface acidity and alkalinity both stronger (i.e. lower pH and pOH). Whether acid-associated cations (such as H_3O^+) and/or the hydroxide anion have strong surface propensity for the air-water interface likely depends on the composition of the solution and what other species are competing for hydration and/or surface access. This would partly explain apparently conflicting results in the literature.[107–112]

1.4 Description of Dissertation Chapters

This chapter has been a brief overview of several key areas of scientific research related to aerosol acidity with a particular emphasis on recent work. The following chapters show research advances this author has made in this field. Chapter 2 covers major experimental methods used in subsequent chapters. Chapter 3 presents results from a sampling intensive that show the pH of fresh SSA. Chapter 4 discusses the isolation of a particular S(IV) oxidation pathway and the pH-dependence of its aerosol-phase acceleration. Chapter 5 illustrates a unique type of buffering that can occur via evaporation of organic acids. Chapter 6 expands and applies this idea to the depletion of nitrate and chloride. Chapter 7 highlights the pH- and salt-dependent propensity of amino acids to reside at the air-water interface, which has implications for heterogeneous atmospheric chemistry. Finally, Chapter 8 summarizes these findings and gives recommendations for future research. A schematic depicting the organization of research ideas is given in Figure 1.1.

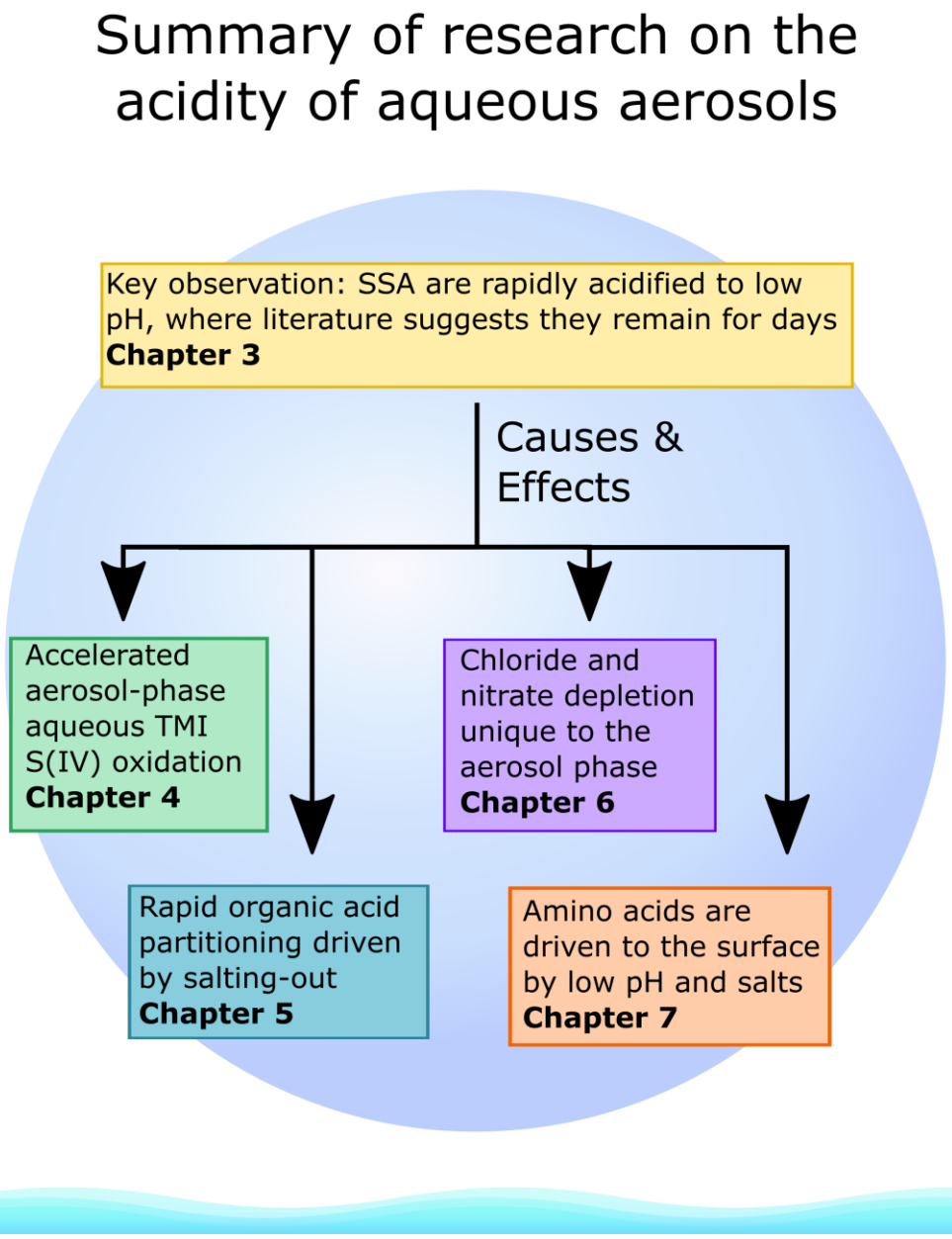

Figure 1.1: Relationships between research projects discussed in this dissertation. As the dominant source of atmospheric aqueous aerosols, SSA were the ideal candidate for studying pH changes early in a particle's lifetime. The subsequent projects helped explain this acidity and/or highlighted important pH-dependent processes in aerosols; some projects, such as the S(IV) work, involved elements of both. In addition, moving from left to right in the figure, the focus moves from largely kinetic to additionally incorporating thermodynamics. Major products of each chapter are written in bold.

1.5 References

(1) Prather, K. A.; Bertram, T. H.; Grassian, V. H.; Deane, G. B.; Stokes, M. D.; DeMott, P. J.; Aluwihare, L. I.; Palenik, B. P.; Azam, F.; Seinfeld, J. H.; Moffet, R. C.; Molina, M. J.; Cappa, C. D.; Geiger, F. M.; Roberts, G. C.; Russell, L. M.; Ault, A. P.; Baltrusaitis, J.; Collins, D. B.; Corrigan, C. E.; Cuadra-Rodriguez, L. A.; Ebben, C. J.; Forestieri, S. D.; Guasco, T. L.; Hersey, S. P.; Kim, M. J.; Lambert, W. F.; Modini, R. L.; Mui, W.; Pedler, B. E.; Ruppel, M. J.; Ryder, O. S.; Schoepp, N. G.; Sullivan, R. C.; Zhao, D. Bringing the Ocean into the Laboratory to Probe the Chemical Complexity of Sea Spray Aerosol. *Proc. Natl. Acad. Sci. U. S. A.* **2013**, *110* (19), 7550–7555.

(2) Jiang, X.; Rotily, L.; Villermaux, E.; Wang, X. Submicron Drops from Flapping Bursting Bubbles. *Proc. Natl. Acad. Sci. U. S. A.* **2022**, *119* (1), e2112924119.

(3) Blanchard, D. C. The Ejection of Drops from the Sea and Their Enrichment with Bacteria and Other Materials: A Review. *Estuaries 1989 123* **1989**, *12* (3), 127–137.

(4) Wang, X.; Deane, G. B.; Moore, K. A.; Ryder, O. S.; Stokes, M. D.; Beall, C. M.; Collins, D. B.; Santander, M. V.; Burrows, S. M.; Sultana, C. M.; Prather, K. A. The Role of Jet and Film Drops in Controlling the Mixing State of Submicron Sea Spray Aerosol Particles. *Proc. Natl. Acad. Sci. U. S. A.* **2017**, *114* (27), 6978–6983.

(5) Wu, J. Production of Spume Drops by the Wind Tearing of Wave Crests: The Search for Quantification. *J. Geophys. Res. Ocean.* **1993**, *98* (C10), 18221–18227.

(6) Pant, V.; Deshpande, C. G.; Kamra, A. K. On the Aerosol Number Concentration–Wind Speed Relationship during a Severe Cyclonic Storm over South Indian Ocean. *J. Geophys. Res. Atmos.* **2008**, *113* (D2), 2206.

(7) Flores, J. M.; Bourdin, G.; Kostinski, A. B.; Altaratz, O.; Dagan, G.; Lombard, F.; Haëntjens, N.; Boss, E.; Sullivan, M. B.; Gorsky, G.; Lang-Yona, N.; Trainic, M.; Romac, S.; Voolstra, C. R.; Rudich, Y.; Vardi, A.; Koren, I. Diel Cycle of Sea Spray Aerosol Concentration. *Nat. Commun.* **2021**, *12* (1), 1–12.

(8) Saliba, G.; Chen, C. L.; Lewis, S.; Russell, L. M.; Rivellini, L. H.; Lee, A. K. Y.; Quinn, P. K.; Bates, T. S.; Haëntjens, N.; Boss, E. S.; Karp-Boss, L.; Baetge, N.; Carlson, C. A.; Behrenfeld, M. J. Factors Driving the Seasonal and Hourly Variability of Sea-Spray Aerosol Number in the North Atlantic. *Proc. Natl. Acad. Sci. U. S. A.* **2019**, *116* (41), 20309–20314.

(9) Saltzman, E. S. *Marine Aerosols*; Le Quere, C., Saltzman, E., Eds.; American Geophysical Union, 2009.

(10) Li-Jones, X.; Maring, H. B.; Prospero, J. M. Effect of Relative Humidity on Light Scattering by Mineral Dust Aerosol as Measured in the Marine Boundary Layer over the Tropical Atlantic Ocean. *J. Geophys. Res. Atmos.* **1998**, *103* (D23), 31113–31121.

(11) Tumminello, P. R.; James, R. C.; Kruse, S.; Kawasaki, A.; Cooper, A.; Guadalupe-Diaz,

I.; Zepeda, K. L.; Crocker, D. R.; Mayer, K. J.; Sauer, J. S.; Lee, C.; Prather, K. A.; Slade, J. H. Evolution of Sea Spray Aerosol Particle Phase State across a Phytoplankton Bloom. *ACS Earth Sp. Chem.* **2021**, *5* (11), 2995–3007.

(12) Baboomian, V. J.; Crescenzo, G. V.; Huang, Y.; Mahrt, F.; Shiraiwa, M.; Bertram, A. K.; Nizkorodov, S. A. Sunlight Can Convert Atmospheric Aerosols into a Glassy Solid State and Modify Their Environmental Impacts. *Proc. Natl. Acad. Sci.* **2022**, *119* (43), e2208121119.

(13) Kaluarachchi, C. P.; Or, V. W.; Lan, Y.; Madawala, C. K.; Hasenecz, E. S.; Crocker, D. R.; Morris, C. K.; Lee, H. D.; Mayer, K. J.; Sauer, J. S.; Lee, C.; Dorce, G.; Malfatti, F.; Stone, E. A.; Cappa, C. D.; Grassian, V. H.; Prather, K. A.; Tivanski, A. V. Size-Dependent Morphology, Composition, Phase State, and Water Uptake of Nascent Submicrometer Sea Spray Aerosols during a Phytoplankton Bloom. *ACS Earth Sp. Chem.* **2022**, *6* (1), 116–130.

(14) Raabe, O. G. Aerosol Aerodynamic Size Conventions For Inertial Sampler Calibration. *J. Air Pollut. Control Assoc.* **1976**, *26* (9), 856–860.

(15) Reid, J. P.; Dennis-Smither, B. J.; Kwamena, N. O. A.; Miles, R. E. H.; Hanford, K. L.; Homer, C. J. The Morphology of Aerosol Particles Consisting of Hydrophobic and Hydrophilic Phases: Hydrocarbons, Alcohols and Fatty Acids as the Hydrophobic Component. *Phys. Chem. Chem. Phys.* **2011**, *13* (34), 15559–15572.

(16) Cochran, R. E.; Jayarathne, T.; Stone, E. A.; Grassian, V. H. Selectivity across the Interface: A Test of Surface Activity in the Composition of Organic-Enriched Aerosols from Bubble Bursting. *J. Phys. Chem. Lett.* **2016**, *7* (9), 1692–1696.

(17) Bikkina, P.; Kawamura, K.; Bikkina, S.; Kunwar, B.; Tanaka, K.; Suzuki, K. Hydroxy Fatty Acids in Remote Marine Aerosols over the Pacific Ocean: Impact of Biological Activity and Wind Speed. *ACS Earth Sp. Chem.* **2019**, *3* (3), 366–379.

(18) Jayarathne, T.; Sultana, C. M.; Lee, C.; Malfatti, F.; Cox, J. L.; Pendergraft, M. A.; Moore, K. A.; Azam, F.; Tivanski, A. V.; Cappa, C. D.; Bertram, T. H.; Grassian, V. H.; Prather, K. A.; Stone, E. A. Enrichment of Saccharides and Divalent Cations in Sea Spray Aerosol During Two Phytoplankton Blooms. *Environ. Sci. Technol.* **2016**, *50* (21), 11511–11520.

(19) Triesch, N.; Van Pinxteren, M.; Salter, M.; Stolle, C.; Pereira, R.; Zieger, P.; Herrmann, H. Sea Spray Aerosol Chamber Study on Selective Transfer and Enrichment of Free and Combined Amino Acids. *ACS Earth Sp. Chem.* **2021**, *5* (6), 1564–1574.

(20) Malfatti, F.; Lee, C.; Tinta, T.; Pendergraft, M. A.; Celussi, M.; Zhou, Y.; Sultana, C. M.; Rotter, A.; Axson, J. L.; Collins, D. B.; Santander, M. V.; Anides Morales, A. L.; Aluwihare, L. I.; Riemer, N.; Grassian, V. H.; Azam, F.; Prather, K. A. Detection of Active Microbial Enzymes in Nascent Sea Spray Aerosol: Implications for Atmospheric Chemistry and Climate. *Environ. Sci. Technol. Lett.* **2019**, *6* (3), 171–177.

(21) Song, Y.; Li, J.; Tsona, N. T.; Liu, L.; Du, L. Enrichment of Short-Chain Organic Acids Transferred to Submicron Sea Spray Aerosols. *Sci. Total Environ.* **2022**, *851*, 158122.

(22) Ozgurel, O.; Duflot, D.; Masella, M.; Réal, F.; Toubin, C. A Molecular Scale Investigation of Organic/Inorganic Ion Selectivity at the Air-Liquid Interface. *ACS Earth Sp. Chem.* **2022**, *6* (7), 1698–1716.

(23) Salter, M. E.; Hamacher-Barth, E.; Leck, C.; Werner, J.; Johnson, C. M.; Riipinen, I.; Nilsson, E. D.; Zieger, P. Calcium Enrichment in Sea Spray Aerosol Particles. *Geophys. Res. Lett.* **2016**, *43* (15), 8277–8285.

(24) Bertram, T. H.; Cochran, R. E.; Grassian, V. H.; Stone, E. A. Sea Spray Aerosol Chemical Composition: Elemental and Molecular Mimics for Laboratory Studies of Heterogeneous and Multiphase Reactions. *Chem. Soc. Rev.* **2018**, *47* (7), 2374–2400.

(25) Lv, S.; Wang, F.; Wu, C.; Chen, Y.; Liu, S.; Zhang, S.; Li, D.; Du, W.; Zhang, F.; Wang, H.; Huang, C.; Fu, Q.; Duan, Y.; Wang, G. Gas-to-Aerosol Phase Partitioning of Atmospheric Water-Soluble Organic Compounds at a Rural Site in China: An Enhancing Effect of NH3 on SOA Formation. *Environ. Sci. Technol.* **2022**, *56* (7), 3915–3924.

(26) Sander, R. Compilation of Henry's Law Constants (Version 4.0) for Water as Solvent. *Atmos. Chem. Phys* **2015**, *15*, 4399–4981.

(27) Kampf, C. J.; Waxman, E. M.; Slowik, J. G.; Dommen, J.; Pfaffenberger, L.; Praplan, A. P.; Prévoît, A. S. H.; Baltensperger, U.; Hoffmann, T.; Volkamer, R. Effective Henry's Law Partitioning and the Salting Constant of Glyoxal in Aerosols Containing Sulfate. *Environ. Sci. Technol.* **2013**, *47* (9), 4236–4244.

(28) Shah, D. J.; Tlwari, K. K. Effect of Salt on the Distribution of Acetic Acid between Water and Organic Solvent. *J. Chem. Eng. Data* **1981**, *26*, 57.

(29) Häkkinen, S. A. K.; McNeill, V. F.; Riipinen, I. Effect of Inorganic Salts on the Volatility of Organic Acids. *Environ. Sci. Technol.* **2014**, *48* (23), 13718–13726.

(30) Zaveri, R. A.; Shilling, J. E.; Zelenyuk, A.; Zawadowicz, M. A.; Suski, K.; China, S.; Bell, D. M.; Veghte, D.; Laskin, A. Particle-Phase Diffusion Modulates Partitioning of Semivolatile Organic Compounds to Aged Secondary Organic Aerosol. *Environ. Sci. Technol.* **2020**, *54* (5), 2595–2605.

(31) Pye, H. O. T.; Nenes, A.; Alexander, B.; Ault, A. P.; Barth, M. C.; Clegg, S. L.; Collett, J. L.; Fahey, K. M.; Hennigan, C. J.; Herrmann, H.; Kanakidou, M.; Kelly, J. T.; Ku, I.-T.; Mcneill, V. F.; Riemer, N.; Schaefer, T.; Shi, G.; Tilgner, A.; Walker, J. T.; Wang, T.; Weber, R.; Xing, J.; Zaveri, R. A.; Zuend, A. The Acidity of Atmospheric Particles and Clouds. *Atmos. Chem. Phys.* **2020**, *20*, 4809–4888.

(32) Harvie, C. E.; Møller, N.; Weare, J. H. The Prediction of Mineral Solubilities in Natural Waters: The Na-K-Mg-Ca-H-Cl-SO_4-OH-HCO_3-CO_3-CO_2-H_2O System to High Ionic Strengths at 25°C. *Geochim. Cosmochim. Acta* **1984**, *48* (4), 723–751.

(33) Bates, R. G.; Popovych, O. The Modern Meaning of pH. *CRC Crit. Rev. Anal. Chem.* **1981**, *10* (3), 247–278.

(34) Stoyanov, E. S.; Stoyanova, I. V.; Reed, C. A. The Structure of the Hydrogen Ion (H_{Aq}^{+}) in Water. *J. Am. Chem. Soc.* **2010**, *132* (5), 1484–1485.

(35) Jia, S.; Wang, X.; Zhang, Q.; Sarkar, S.; Wu, L.; Huang, M.; Zhang, J.; Yang, L. Technical Note: Comparison and Interconversion of pH Based on Different Standard States for Aerosol Acidity Characterization. *Atmos. Chem. Phys.* **2018**, *18* (15), 11125–11133.

(36) Winkler, P. Observations on Acidity in Continental and in Marine Atmospheric Aerosols and in Precipitation. *J. Geophys. Res.* **1980**, *85* (C8), 4481–4486.

(37) Winkler, P. Relations between Aerosol Acidity and Ion Balance. In *Chemistry of Multiphase Atmospheric Systems*; Springer Berlin Heidelberg, 1986; pp 269–298.

(38) Xue, J.; Lau, A. K. H.; Yu, J. Z. A Study of Acidity on PM2.5 in Hong Kong Using Online Ionic Chemical Composition Measurements. *Atmos. Environ.* **2011**, *45* (39), 7081–7088.

(39) Ganor, E.; Levin, Z.; Pardess, D. Determining the Acidity and Chemical Composition of Fog, Haze and Cloud Droplets in Israel. *Atmos. Environ. Part A, Gen. Top.* **1993**, *27* (12), 1821–1832.

(40) Craig, R. L.; Peterson, P. K.; Nandy, L.; Lei, Z.; Hossain, M. A.; Camarena, S.; Dodson, R. A.; Cook, R. D.; Dutcher, C. S.; Ault, A. P. Direct Determination of Aerosol pH: Size-Resolved Measurements of Submicrometer and Supermicrometer Aqueous Particles. *Anal. Chem.* **2018**, *90* (19), 11232–11239.

(41) Song, Q.; Osada, K. Direct Measurement of Aerosol Acidity Using pH Testing Paper and Hygroscopic Equilibrium under High Relative Humidity. *Atmos. Environ.* **2021**, *261*, 118605.

(42) Li, G.; Su, H.; Ma, N.; Zheng, G.; Kuhn, U.; Li, M.; Klimach, T.; Pöschl, U.; Cheng, Y. Multifactor Colorimetric Analysis on pH-Indicator Papers: An Optimized Approach for Direct Determination of Ambient Aerosol pH. *Atmos. Meas. Tech.* **2020**, *13* (11), 6053–6065.

(43) Angle, K. J.; Crocker, D. R.; Simpson, R. M. C.; Mayer, K. J.; Garofalo, L. A.; Moore, A. N.; Mora Garcia, S. L.; Or, V. W.; Srinivasan, S.; Farhan, M.; Sauer, J. S.; Lee, C.; Pothier, M. A.; Farmer, D. K.; Martz, T. R.; Bertram, T. H.; Cappa, C. D.; Prather, K. A.; Grassian, V. H. Acidity across the Interface from the Ocean Surface to Sea Spray Aerosol. *Proc. Natl. Acad. Sci.* **2020**, *118* (2), e2018397118.

(44) Lei, Z.; Bliesner, S. E.; Mattson, C. N.; Cooke, M. E.; Olson, N. E.; Chibwe, K.; Albert, J. N. L.; Ault, A. P. Aerosol Acidity Sensing via Polymer Degradation. *Anal. Chem.* **2020**, *92* (9), 6502–6511.

(45) Craig, R. L.; Nandy, L.; Axson, J. L.; Dutcher, C. S.; Ault, A. P. Spectroscopic Determination of Aerosol pH from Acid–Base Equilibria in Inorganic, Organic, and Mixed Systems. *J. Phys. Chem. A* **2017**, *121* (30), 5690–5699.

(46) Coddens, E. M.; Angle, K. J.; Grassian, V. H. Titration of Aerosol pH through Droplet Coalescence. *J. Phys. Chem. Lett.* **2019**, *10* (15), 4476–4483.

(47) Boyer, H. C.; Gorkowski, K.; Sullivan, R. C. In Situ pH Measurements of Individual Levitated Microdroplets Using Aerosol Optical Tweezers. *Anal. Chem.* **2020**, *92* (1), 1089–1096.

(48) Wei, H.; Vejerano, E. P.; Leng, W.; Huang, Q.; Willner, M. R.; Marr, L. C.; Vikesland, P. J. Aerosol Microdroplets Exhibit a Stable pH Gradient. *Proc. Natl. Acad. Sci. U. S. A.* **2018**, *115* (28), 7272–7277.

(49) Li, L.-F.; Chen, Z.; Liu, P.; Zhang, Y.-H. Direct Measurement of pH Evolution in Aerosol Microdroplets Undergoing Ammonium Depletion: A Surface-Enhanced Raman Spectroscopy Approach. *Environ. Sci. Technol.* **2022**, *56* (10), 6274–6281.

(50) Tackman, E. C.; Grady, R. S.; Freedman, M. A. Direct Measurement of the pH of Aerosol Particles Using Carbon Quantum Dots. *Anal. Methods* **2022**, *14* (30), 2929–2936.

(51) Jing, X.; Chen, Z.; Huang, Q.; Liu, P.; Zhang, Y.-H. Spatiotemporally Resolved pH Measurement in Aerosol Microdroplets Undergoing Chloride Depletion: An Application of In Situ Raman Microspectrometry.

(52) Hennigan, C. J.; Izumi, J.; Sullivan, A. P.; Weber, R. J.; Nenes, A. A Critical Evaluation of Proxy Methods Used to Estimate the Acidity of Atmospheric Particles. *Atmos. Chem. Phys.* **2015**, *15* (5), 2775–2790.

(53) Clegg, S. L.; Brimblecombe, P.; Wexler, A. S. Thermodynamic Model of the System H^+–NH_4^+–SO_4^{2-}–NO_3^-–H_2O at Tropospheric Temperatures. *J. Phys. Chem. A* **1998**, *102* (12), 2137–2154.

(54) Clegg, S. L.; Brimblecombe, P.; Wexler, A. S. Thermodynamic Model of the System H^+-NH_4^+-Na^+-SO_4^{2-}-NO_3^--Cl^--H_2O at 298.15 K. *J. Phys. Chem. A* **1998**, *102* (12), 2155–2171.

(55) Wexler, A. S.; Clegg, S. L. Atmospheric Aerosol Models for Systems Including the Ions H^+, NH_4^+, Na^+, SO_4^{2-}, NO_3^-, Cl^-, Br^-, and H_2O. *J. Geophys. Res. Atmos.* **2002**, *107* (14), ACH 14-1.

(56) Clegg, S. L.; Brimblecombe, P.; Wexler, A. S. Extended AIM aerosol thermodynamics model http://www.aim.env.uea.ac.uk/aim/aim.php (accessed May 27, 2020).

(57) Clegg, S. L.; Pitzer, K. S.; Brimblecombe, P. Thermodynamics of Multicomponent, Miscible, Ionic Solutions. 2. Mixtures Including Unsymmetrical Electrolytes. *J. Phys. Chem.* **1992**, *96* (23), 9470–9479.

(58) Fountoukis, C.; Nenes, A. ISORROPIAII: A Computationally Efficient Thermodynamic Equilibrium Model for K^+-Ca^{2+}-Mg^{2+}+-NH_4^+-Na^+-SO_4^{2-}-NO_3^--Cl^--H_2O Aero. *Atmos. Chem. Phys.* **2007**, *7* (17), 4639–4659.

(59) Li, M.; Su, H.; Zheng, G.; Kuhn, U.; Kim, N.; Li, G.; Ma, N.; Pöschl, U.; Cheng, Y. Aerosol pH and Ion Activities of HSO_4^- and SO_4^{2-} in Supersaturated Single Droplets. *Environ. Sci. Technol.* **2022**.

(60) Song, S.; Gao, M.; Xu, W.; Shao, J.; Shi, G.; Wang, S.; Wang, Y.; Sun, Y.; McElroy, M. B. Fine-Particle pH for Beijing Winter Haze as Inferred from Different Thermodynamic Equilibrium Models. *Atmos. Chem. Phys.* **2018**, *18* (10), 7423–7438.

(61) Box, G. E. P. Robustness in the Strategy of Scientific Model Building. In *Robustness in Statistics*; Launer, R. L., Wilkinson, G. N., Eds.; Academic Press, 1979; pp 201–236.

(62) Angle, K. J.; Grassian, V. H.; Ault, A. P. The Rapid Acidification of Sea Spray Aerosols. *Phys. Today* **2022**, *75* (1), 58.

(63) Weber, R. J.; Guo, H.; Russell, A. G.; Nenes, A. High Aerosol Acidity despite Declining Atmospheric Sulfate Concentrations over the Past 15 Years. *Nat. Geosci.* **2016**, *9* (4), 282–285.

(64) Guo, H.; Weber, R. J.; Nenes, A. High Levels of Ammonia Do Not Raise Fine Particle pH Sufficiently to Yield Nitrogen Oxide-Dominated Sulfate Production. *Sci. Rep.* **2017**, *7* (1).

(65) Von Glasow, R.; Sander, R. Variation of Sea Salt Aerosol pH with Relative Humidity. *Geophys. Res. Lett.* **2001**, *28* (2), 247–250.

(66) Shi, G.; Xu, J.; Peng, X.; Xiao, Z.; Chen, K.; Tian, Y.; Guan, X.; Feng, Y.; Yu, H.; Nenes, A.; Russell, A. G. pH of Aerosols in a Polluted Atmosphere: Source Contributions to Highly Acidic Aerosol. *Environ. Sci. Technol.* **2017**, *51* (8), 4289–4296.

(67) Fridlind, A. M.; Jacobson, M. Z. A Study of Gas-Aerosol Equilibrium and Aerosol pH in the Remote Marine Boundary Layer during the First Aerosol Characterization Experiment (ACE 1). *J. Geophys. Res. Atmos.* **2000**, *105* (D13), 17325–17340.

(68) Bougiatioti, A.; Nikolaou, P.; Stavroulas, I.; Kouvarakis, G.; Weber, R.; Nenes, A.; Kanakidou, M.; Mihalopoulos, N. Particle Water and pH in the Eastern Mediterranean: Source Variability and Implications for Nutrient Availability. *Atmos. Chem. Phys* **2016**, *16*, 4579–4591.

(69) Kroll, J. H.; Cross, E. S.; Hunter, J. F.; Pai, S.; Wallace, L. M. M.; Croteau, P. L.; Jayne, J. T.; Worsnop, D. R.; Heald, C. L.; Murphy, J. G.; Frankel, S. L. Atmospheric Evolution of Sulfur Emissions from Kilauea: Real-Time Measurements of Oxidation, Dilution, and Neutralization within a Volcanic Plume. *Environ. Sci. Technol.* **2015**, *49* (7), 4129–4137.

(70) Zheng, G.; Su, H.; Wang, S.; Andreae, M. O.; Pöschl, U.; Cheng, Y. Multiphase Buffer Theory Explains Contrasts in Atmospheric Aerosol Acidity. *Science* **2020**, *369* (6509),

1374–1377.

(71) Haszpra, T. Intricate Features in the Lifetime and Deposition of Atmospheric Aerosol Particles. *Chaos An Interdiscip. J. Nonlinear Sci.* **2019**, *29* (7), 071103.

(72) Ruan, X.; Zhao, C.; Zaveri, R. A.; He, P.; Wang, X.; Shao, J.; Geng, L. Simulations of Aerosol pH in China Using WRF-Chem (v4.0): Sensitivities of Aerosol pH and Its Temporal Variations during Haze Episodes. *Geosci. Model Dev.* **2022**, *15* (15), 6143–6164.

(73) Arangio, A. M.; Shahpoury, P.; Dabek-Zlotorzynska, E.; Nenes, A. Seasonal Aerosol Acidity, Liquid Water Content and Their Impact on Fine Urban Aerosol in SE Canada. *Atmosphere (Basel).* **2022**, *13* (7), 1012.

(74) Nah, T.; Lam, Y. H. Influence of Urban Heat Islands on Seasonal Aerosol Acidity and Aerosol Liquid Water Content in Humid Subtropical Hong Kong, South China. *Atmos. Environ.* **2022**, *289*, 119321.

(75) Kim, K. H.; Kabir, E.; Kabir, S. A Review on the Human Health Impact of Airborne Particulate Matter. *Environ. Int.* **2015**, *74*, 136–143.

(76) Fang, T.; Guo, H.; Zeng, L.; Verma, V.; Nenes, A.; Weber, R. J. Highly Acidic Ambient Particles, Soluble Metals, and Oxidative Potential: A Link between Sulfate and Aerosol Toxicity. *Environ. Sci. Technol.* **2017**, *51* (5), 2611–2620.

(77) Ghio, A. J.; Carraway, M. S.; Madden, M. C. Composition of Air Pollution Particles and Oxidative Stress in Cells, Tissues, and Living Systems. *J. Toxicol. Environ. Heal. Part B* **2011**, *15* (1), 1–21.

(78) Lelieveld, J.; Evans, J. S.; Fnais, M.; Giannadaki, D.; Pozzer, A. The Contribution of Outdoor Air Pollution Sources to Premature Mortality on a Global Scale. *Nature* **2015**, *525* (7569), 367–371.

(79) Ahlawat, A.; Mishra, S. K.; Herrmann, H.; Rajeev, P.; Gupta, T.; Goel, V.; Sun, Y.; Wiedensohler, A. Impact of Chemical Properties of Human Respiratory Droplets and Aerosol Particles on Airborne Viruses’ Viability and Indoor Transmission. *Viruses* **2022**, *14* (7), 1497.

(80) Klein, L. K.; Luo, B.; Bluvshtein, N.; Krieger, U. K.; Schaub, A.; Glas, I.; David, S. C.; Violaki, K.; Motos, G.; Pohl, M. O.; Hugentobler, W.; Nenes, A.; Stertz, S.; Peter, T.; Kohn, T. Expiratory Aerosol pH Is Determined by Indoor Room Trace Gases and Particle Size. *Proc. Natl. Acad. Sci.* **2022**, *119* (39), e2212140119.

(81) Oswin, H. P.; Haddrell, A. E.; Otero-Fernandez, M.; Mann, J. F. S.; Cogan, T. A.; Hilditch, T. G.; Tian, J.; Hardy, D.; Hill, D. J.; Finn, A.; Davidson, A. D.; Reid, J. P. Reply to Klein et Al.: The Importance of Aerosol pH for Airborne Respiratory Virus Transmission. *Proc. Natl. Acad. Sci.* **2022**, *119* (39), e2212556119.

(82) Lu, H.; Bellucci, L.; Sun, S.; Qi, D.; Rosa, M.; Berger, R.; Corni, S.; Bonn, M. Acidic PH Promotes Refolding and Macroscopic Assembly of Amyloid β (16-22) Peptides at the Air-Water Interface. *J. Phys. Chem. Lett.* **2022**, *13* (29), 6674–6679.

(83) Duan, J.; Lyu, R.; Wang, Y.; Xie, X.; Wu, Y.; Tao, J.; Cheng, T.; Liu, Y.; Peng, Y.; Zhang, R.; He, Q.; Ga, W.; Zhang, X.; Zhang, Q. Particle Liquid Water Content and Aerosol Acidity Acting as Indicators of Aerosol Activation Changes in Cloud Condensation Nuclei (CCN) during Pollution Eruption in Guangzhou of South China. *Aerosol Air Qual. Res.* **2019**, *19*, 2662–2670.

(84) Ren, Y.; Soni, A.; Bertram, A.; Patey, G. The Influence of pH on Ice Nucleation by Alpha-Alumina. In *EGU General Assembly 2022*; Copernicus Meetings, 2022.

(85) Mitra, K.; Mishra, H. R.; Pei, X.; Pathak, R. K. Secondary Organic Aerosol (SOA) from Photo-Oxidation of Toluene: 1 Influence of Reactive Nitrogen, Acidity and Water Vapours on Optical Properties. *Atmos. 2022, Vol. 13, Page 1099* **2022**, *13* (7), 1099.

(86) Lei, Z.; Chen, Y.; Zhang, Y.; Cooke, M. E.; Ledsky, I. R.; Armstrong, N. C.; Olson, N. E.; Zhang, Z.; Gold, A.; Surratt, J. D.; Ault, A. P. Initial pH Governs Secondary Organic Aerosol Phase State and Morphology after Uptake of Isoprene Epoxydiols (IEPOX). *Environ. Sci. Technol.* **2022**, *56* (15), 10596–10607.

(87) Zhang, Y.; Chen, Y.; Lei, Z.; Olson, N.; Riva, M.; Koss, A. R.; Zhang, Z.; Gold, A.; Jayne, J. T.; Worsnop, D. R.; Onasch, T. B.; Kroll, J. H.; Turpin, B. J.; Ault, A. P.; Surratt, J. D. Joint Impacts of Acidity and Viscosity on the Formation of Secondary Organic Aerosol from Isoprene Epoxydiols (IEPOX) in Phase Separated Particles. *ACS Earth Sp. Chem.* **2019**, *3* (12), 2646–2658.

(88) Bready, C. J.; Vanovac, S.; Odbadrakh, T. T.; Shields, G. C. Amino Acids Compete with Ammonia in Sulfuric Acid-Based Atmospheric Aerosol Prenucleation: The Case of Glycine and Serine. *J. Phys. Chem. A* **2022**, *126* (31), 5195–5206.

(89) Wang, Y.; Zhang, Q.; Jiang, J.; Zhou, W.; Wang, B.; He, K.; Duan, F.; Zhang, Q.; Philip, S.; Xie, Y. Enhanced Sulfate Formation during China's Severe Winter Haze Episode in January 2013 Missing from Current Models. *J. Geophys. Res. Atmos.* **2014**, *119* (17), 10,425-10,440.

(90) Connick, R. E.; Zhang, Y.-X.; Lee, S.; Adamic, R.; Chieng, P. Kinetics and Mechanism of the Oxidation of HSO_3^- by O_2. 1. the Uncatalyzed Reaction. *Inorg. Chem.* **1995**, *34* (18), 4543–4553.

(91) Hung, H. M.; Hsu, M. N.; Hoffmann, M. R. Quantification of SO_2 Oxidation on Interfacial Surfaces of Acidic Micro-Droplets: Implication for Ambient Sulfate Formation. *Environ. Sci. Technol.* **2018**, *52* (16), 9079–9086.

(92) Rodriguez, A. A.; Rafla, M. A.; Welsh, H. G.; Pennington, E. A.; Casar, J. R.; Hawkins, L. N.; Jimenez, N. G.; De Loera, A.; Stewart, D. R.; Rojas, A.; Tran, M. K.; Lin, P.; Laskin, A.; Formenti, P.; Cazaunau, M.; Pangui, E.; Doussin, J. F.; De Haan, D. O.

Kinetics, Products, and Brown Carbon Formation by Aqueous-Phase Reactions of Glycolaldehyde with Atmospheric Amines and Ammonium Sulfate. *J. Phys. Chem. A* **2022**.

(93) Gao, J.; Shi, G.; Zhang, Z.; Wei, Y.; Tian, X.; Feng, Y.; Russell, A. G.; Nenes, A. Targeting Atmospheric Oxidants Can Better Reduce Sulfate Aerosol in China: H_2O_2 Aqueous Oxidation Pathway Dominates Sulfate Formation in Haze. *Environ. Sci. Technol.* **2022**, *56* (15), 10608–10618.

(94) Rindelaub, J. D.; Borca, C. H.; Hostetler, M. A.; Slade, J. H.; Lipton, M. A.; Slipchenko, L. V.; Shepson, P. B. The Acid-Catalyzed Hydrolysis of an α -Pinene-Derived Organic Nitrate: Kinetics, Products, Reaction Mechanisms, and Atmospheric Impact. *Atmos. Chem. Phys.* **2016**, *16* (23), 15425–15432.

(95) Bzdek, B. R.; Reid, J. P.; Malila, J.; Prisle, N. L. The Surface Tension of Surfactant-Containing, Finite Volume Droplets. *Proc. Natl. Acad. Sci.* **2020**, *117* (15), 8335–8343.

(96) Wilson, K. R.; Prophet, A. M.; Rovelli, G.; Willis, M. D.; Rapf, R. J.; Jacobs, M. I. A Kinetic Description of How Interfaces Accelerate Reactions in Micro-Compartments. *Chem. Sci.* **2020**, *11* (32), 8533–8545.

(97) Qian, Y.; Brown, J. B.; Huang-Fu, Z. C.; Zhang, T.; Wang, H.; Wang, S. Y.; Dadap, J. I.; Rao, Y. In Situ Analysis of the Bulk and Surface Chemical Compositions of Organic Aerosol Particles. *Commun. Chem.* **2022**, *5* (1), 1–7.

(98) Li, K.; Gong, K.; Liu, J.; Ji, M.; Valev, V. K.; Zhang, L. Significantly Accelerated Photochemical and Photocatalytic Reactions in Microdroplets. *Cell Reports Phys. Sci.* **2022**, *3*, 100917.

(99) Crawford, E. A.; Esen, C.; Volmer, D. A. Real Time Monitoring of Containerless Microreactions in Acoustically Levitated Droplets via Ambient Ionization Mass Spectrometry. *Anal. Chem.* **2016**, *88* (17), 8396–8403.

(100) Zhang, D.; Yuan, X.; Gong, C.; Zhang, X. High Electric Field on Water Microdroplets Catalyzes Spontaneous and Ultrafast Oxidative C-H/N-H Cross-Coupling. *J. Am. Chem. Soc.* **2022**, *2022*.

(101) Wei, Z.; Li, Y.; Cooks, R. G.; Yan, X. Accelerated Reaction Kinetics in Microdroplets: Overview and Recent Developments. *Annu. Rev. Phys. Chem.* **2020**, *71* (1), 31–51.

(102) Rovelli, G.; Jacobs, M. I.; Willis, M.; Rapf, R. J.; Prophet, A. M.; Wilson, K. R. A Critical Analysis of Electrospray Techniques for the Determination of Accelerated Rates and Mechanisms of Chemical Reactions in Droplets. *Chem. Sci.* **2020**, *11* (48), 13026.

(103) Parmentier, E. A.; Corral Arroyo, P.; Gruseck, R.; Ban, L.; David, G.; Signorell, R. Charge Effects on the Photodegradation of Single Optically Trapped Oleic Acid Aerosol Droplets. *J. Phys. Chem. A* **2022**, *126* (27), 4456–4464.

(104) Banerjee, S.; Gnanamani, E.; Yan, X.; Zare, R. N. Can All Bulk-Phase Reactions Be Accelerated in Microdroplets? *Analyst* **2017**, *142* (9), 1399–1402.

(105) Luo, M.; Wauer, N. A.; Angle, K. J.; Dommer, A. C.; Song, M.; Nowak, C. M.; Amaro, R. E.; Grassian, V. H. Insights into the Behavior of Nonanoic Acid and Its Conjugate Base at the Air/Water Interface through a Combined Experimental and Theoretical Approach. *Chem. Sci.* **2020**, *11* (39), 10647–10656.

(106) Rajagopal, R.; Hong, M. K.; Ziegler, L. D.; Erramilli, S.; Narayan, O. Conjugate Acid-Base Interaction Driven Phase Transition at a 2D Air-Water Interface. *J. Phys. Chem. B* **2021**, *125* (23), 6330–6337.

(107) Bai, C.; Herzfeld, J. Surface Propensities of the Self-Ions of Water. *ACS Cent. Sci.* **2016**, *2* (4), 225–231.

(108) Björneholm, O.; Hansen, M. H.; Hodgson, A.; Liu, L. M.; Limmer, D. T.; Michaelides, A.; Pedevilla, P.; Rossmeisl, J.; Shen, H.; Tocci, G.; Tyrode, E.; Walz, M. M.; Werner, J.; Bluhm, H. Water at Interfaces. *Chem. Rev.* **2016**, *116* (13), 7698–7726.

(109) Tse, Y. L. S.; Chen, C.; Lindberg, G. E.; Kumar, R.; Voth, G. A. Propensity of Hydrated Excess Protons and Hydroxide Anions for the Air-Water Interface. *J. Am. Chem. Soc.* **2015**, *137* (39), 12610–12616.

(110) Das, S.; Imoto, S.; Sun, S.; Nagata, Y.; Backus, E. H. G.; Bonn, M. Nature of Excess Hydrated Proton at the Water-Air Interface. *J. Am. Chem. Soc.* **2020**, *142* (2), 945–952.

(111) Duignan, T. T.; Parsons, D. F.; Ninham, B. W. Hydronium and Hydroxide at the Air–Water Interface with a Continuum Solvent Model. *Chem. Phys. Lett.* **2015**, *635*, 1–12.

(112) Andino, R. S.; Liu, J.; Miller, C. M.; Chen, X.; Devlin, S. W.; Hong, M. K.; Rajagopal, R.; Erramilli, S.; Ziegler, L. D. Anomalous pH-Dependent Enhancement of p-Methyl Benzoic Acid Sum-Frequency Intensities: Cooperative Surface Adsorption Effects. *J. Phys. Chem. A* **2020**, *124* (16), 3064–3076.

CHAPTER 2 EXPERIMENTAL METHODOLOGY

2.1 Sample Preparation

Aqueous solutions were prepared using ultrapure ("milli-Q") water with resistivity ≥ 18.1 MΩ. Solutions were prepared by mass and recorded in molality units (m), as these units are independent of solution temperature. As an example, for the preparation of a 1 m NaCl solution, an empty scintillation vial would first be labeled and weighed on an analytical balance that reports mass to the nearest 0.1 mg. The vial would be removed, the desired amount of NaCl would be added, and the vial would be weighed again (if a highly hygroscopic material such as $CaCl_2$ was weighed, an immediate reading was used to prevent an artificially high reading from condensing water). The vial would then be removed a second time for the addition of water and weighed a final time to determine the mass of water that had been added. Additional time for equilibration of the sealed vial or bottle to lab temperature (ca. 23 °C) was allowed in cases where the vial would become cold (such as from $NaNO_3$) or hot (such as from $MgCl_2$) from the dissolution of solid. In all cases, the final concentration would be calculated from the mass measurements, and the resulting concentration would be used for all analysis. For example, in preparation of a 1 m NaCl solution, the final concentration may be 1.04 m. The value of 1.04 m would thus be used in plotting figures, performing calculations, and reporting data in data packages.

For use in experiments sensitive to the presence of organics, salts such as NaCl and Na_2SO_4 were first baked in an oven at 200 °C for at least 24 hours before use. For experiments requiring knowledge of solution pH, pH was measured using either a Corning 430 pH meter or an Oakton 700 pH meter. The pH meter would be calibrated by two buffers bracketing the anticipated pH of

the solution, unless the pH was < 1.68 or > 10, in which case the two nearest available buffers were used.

2.2 Measurements of Levitated Droplets

Individual aerosols can be suspended in a substrate-free environment through use of optical tweezing. There are a variety of tweezing techniques, but here we focus on the case where a laser beam with a Gaussian intensity profile is directed upward at a single aqueous particle. There has been discussion on whether light exerts a push or pull on dielectric media, but it can be helpful to conceptualize the interaction of light with single particles via two forces.[1] One is the scattering force, F_s, which results from the backscattering of photons at the base of the particle. The other is the gradient force, F_g, resulting from the gradient of intensity across the beam profile. Photons exiting the droplet effectively exert a force on the droplet in the opposite direction of their final exit velocity. Since a Gaussian beam has greater intensity at the beam center, if the aerosol drifts laterally away from the beam center, photons originating closer to the center of the beam exert greater force than those originating from the edge of the beam, which creates a restoring force pushing the aerosol back to the beam center.[2] A stable droplet requires that $F_g > F_s$, and these forces sum to a net force, F_n, depicted in Figure 2.1. From the figure, one can deduce that both the

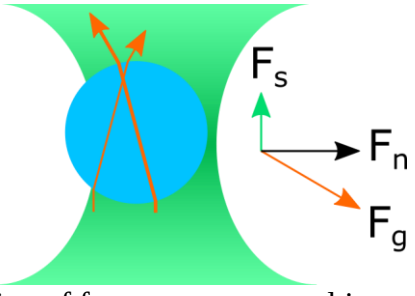

Figure 2.1: Artistic representation of forces on an aerosol in an optical trap (not to scale). The orange arrows crossing the aerosol depict the paths of photons from the laser. The thicker line for the right of these two arrows indicates the greater intensity of the photon originating closer to the center of the Gaussian-profile laser. The net force restores the aerosol to an equilibrium position in the laser, just above the laser's focal point.

power of the laser and the refractive index of the aerosol impact the velocity of photons exiting the aerosol, which impacts F_g, indicating that the appropriate laser power should be used for an aerosol of a given refractive index. The profiles of these forces have been calculated analytically and numerically in the literature.[3] For an approximation, Equation 2.1 can be used.[4]

$$F_n = F_g + F_s \approx \frac{\alpha}{2}\nabla E^2 + (n_p - n_m)^2 * r^6 * I \quad (2.1)$$

Here, α is the polarizability of the particle, E is the incident electric field, n_p and n_m are the refractive indices of the particle and medium, respectively, r is the particle radius, and I is the intensity of the laser beam. In Equation 2.1, the spin-curl force is omitted, which is appropriate as it is small compared to the other forces in most cases.[5]

A Biral Inc. Aerosol Optical Tweezers 100 (hereafter, AOT) was used to perform experiments on individual aerosols. A 532 nm laser was used to suspend the aerosol, create Mie resonances (termed Whispering Gallery Modes, hereafter WGM's), and excite the chemicals within the aerosol to virtual states resulting in Raman spectra upon molecular relaxation. The WGM's are useful as the spacing between them allows calculation of the aerosol's radius, r, and refractive index, n_p, as given in Equation 2.2.[6]

$$2\pi * n_p * r = \lambda * m \quad (2.2)$$

Here, λ is the wavelength of the light circling within the optical cavity and constructively interfering with itself, and m is an integer relating to the number of number of wave maxima in one internal cycle through the aerosol. Given multiple WGM's, therefore, n_p and r can simultaneously determined with precision set by the uncertainty in WGM position. WGM's change in response to aerosol size and thus can be observed to move across the Raman spectrum as the aerosol equilibrates to the cell relative humidity (RH), growing or shrinking. The RH around the aerosol can be controlled and aerosol heating from the laser is expected to be on the order of 10-

100 mK.[7] The radius of the trapped aerosol can range from ca. 2 to 8 μm. The aerosols were typically most stable when high RH (> 75%) and high ionic strength (> 2 m) were used. In order to safely perform experiments with highly acidic aerosols, an additional attachment was created for the AOT (Figure 2.2).

When an aerosol is trapped in the AOT, it can be coalesced with another aerosol to change its composition, including change in pH. This method is described extensively in Coddens, Angle, and Grassian 2019.[8] Briefly, a mouthpiece is added to the nebulizer (MicroAIR U22, OMRON) to increase the probability of the coalescing aerosol being smaller than the existing aerosol. A video recording of the CCD camera feed that tracks the trapped aerosol is turned on. The vacuum

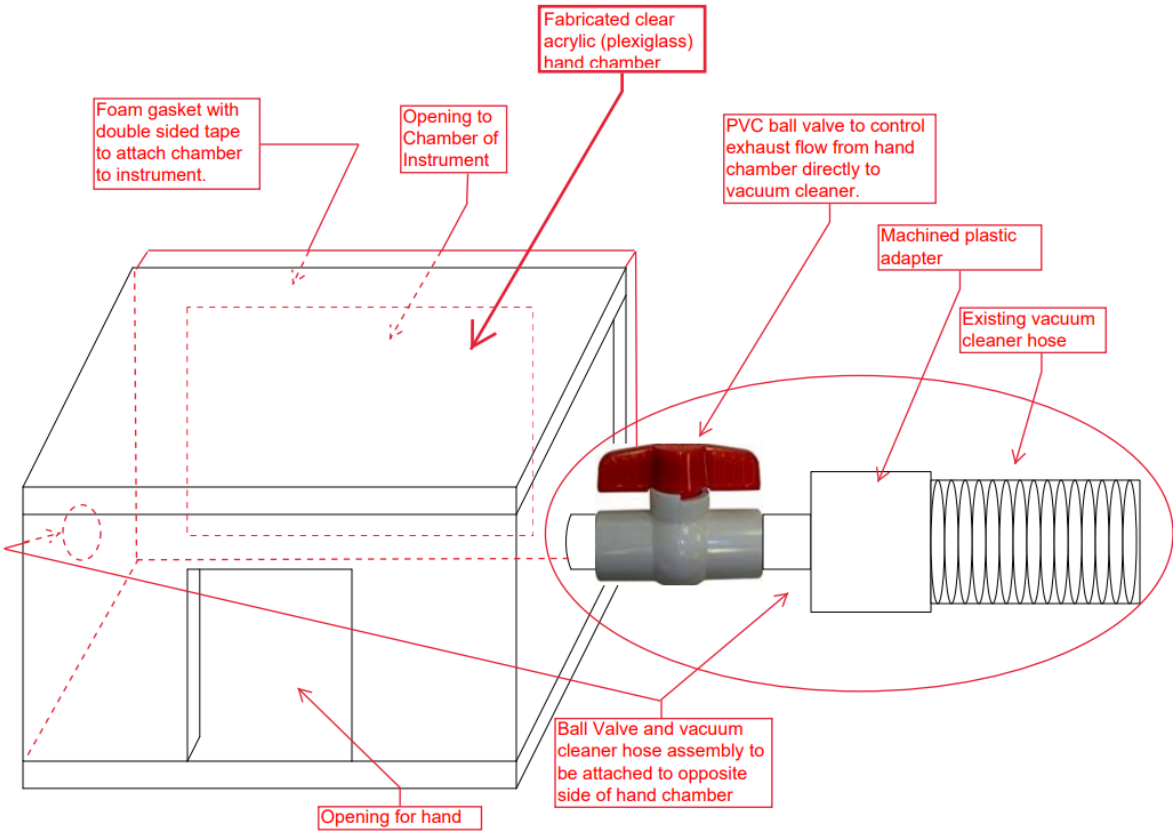

Figure 2.2: Schematic of additional safety attachment designed for the AOT feature. The vacuum cleaner hose feeds into an airline that is ventilated to chemical waste.

attached to the AOT is powered on, and new aerosols are nebulized into the trapping chamber until a coalescence occurs. The occurrence of the coalescence can be confirmed by both the video and by comparing the radius of the aerosol before and after coalescence.

The Raman data from the AOT is reported as a series of separate, ordered text files of wavelength, intensity, and time. Since analysis frequently involved thousands of these files, a MATLAB script written with contributions from Michael Alves was employed. The MATLAB code is available in Appendix A. Briefly, the program collects all of the data, converts the wavelengths to wavenumbers, performs background subtraction and baseline correction based on user inputs, and allows averaging of consecutive windows of spectra for analysis of reaction kinetics. Data from this program was frequently used with the peak fitting algorithms in Igor (Wavemetrics) to enable calculation of peak area over time. Separate MATLAB programs were also written to assist in the extraction of refractive index and radius data from WGM peaks (used for spectra of the water band with the instrument using 1200 grooves per mm centered at 645 nm) as well as detection and removal of interfering WGM peaks (used for spectra of useful peaks such as sulfate or nitrate bands). Additional details on calculations involving WGM's are given in the Methods section of Chapter 4.

2.3 Measurements with Confocal Raman Spectrometer

For comparison to optically levitated aerosols, it is often useful to compare results to bulk solutions and/or substrate-deposited aerosols. The confocal Raman spectrometer (Horiba) was used with the LabSpec 8 software suite. A custom MATLAB script was used to automate the periodic collection of spectra. Experiments were performed with the 1800 grooves per mm grating setting to maximize resolution.

For bulk experiments, the desired solution was added to a petri dish. Two independent methods could be used to focus the laser on the sample. The real time display feature could be used to collect spectra every second, with the spectra centered on a peak known to be intense (such as the water band or the nitrate peak). The stage holding the petri dish could then be raised or lowered incrementally to obtain the maximum signal. Alternatively, a video feed could be used to focus the microscope on a Kimwipe fiber on the sample surface. Either method could be appropriate depending on the duration of the experiment. For long experiments, either periodic refocusing of the laser or use of large amounts of sample are preferred to prevent the Raman intensities from decreasing excessively due to evaporation.

For substrate-deposited experiments, aerosols were deposited on hydrophobic substrates (such as a glass slide coated with Rain-X). The substrate with the aerosol was then placed in an environmental cell, initially set to 50% RH and 298 K, which could then be varied as previously described.[9] A live video was then used to locate an aerosol of the appropriate size for measurement. Similarly to AOT data analysis, a custom MATLAB script (available in the Appendix) was used to compile data for processing.

2.4 Measurements of Acidity with pH Paper

The acidity of aerosols and bulk solutions can be measured with pH paper. Often, the pH paper is designed to measure bulk volumes of buffered, moderate ionic strength solutions. To apply this method to aerosols, sufficient volume must be used (see Chapter 3 for many additional details). In addition, because the pH paper is made from dyes that may have equilibrium constants sensitive to ionic strength, calibrations and control experiments were used to compare the reading of pH paper and pH probes for high ionic strength bulk solutions. Once correction factors were known, the method could be applied to aerosols. These aerosols could be generated from the nebulizer

used for AOT experiments in which case the measurements were performed to *estimate* the initial acidity of the levitated particles. The aerosols could alternately be obtained from a Micro Orifice Uniform Deposit Impactor (MOUDI) as described in Chapter 3.

In either case, the pH paper was photographed with a smartphone and the images were processed in Fuji (an updated version of ImageJ) to extract R, G, and B values for desired locations on the pH paper and the color scale included in the photograph.[10] These RGB values were then used to calculate pH as described in the corresponding MATLAB code (see Appendix A). There have been various proposals for the optimal combination of pH paper and calibration curve to precisely determine acidity.[11–13] Ultimately, the choice of pH paper depends on the identity of the analyte as well as the quantity available. When pH paper requires more mass loading for an accurate reading, it will be less sensitive to trace gases and contaminants, but also take longer for a reading from an accumulation of aerosols, during which the color may fade. In addition, calibration curves can be calculated directly from RGB values, linear combinations of RBG values, or the hue value. When no light box is available to standardize lighting, a calibration curve based on the difference between two different values among R, G, and B has the advantage of subtracting out differences in lighting. Finally, since pH is a logarithmic measure of proton concentration, it is not advised to force a linear relationship between pH and image color.

2.5 Infrared Reflection Absorption Spectroscopy

Infrared Reflection Absorption Spectroscopy (IRRAS), also termed Reflection Absorption Infrared Spectroscopy (RAIRS), refers to the process of bouncing an infrared beam off of an interface and quantifying the small fraction of radiation that reaches a detector. This information can be used to make inferences about surface composition. Importantly, however, recent work has cautioned against using IRRAS peaks for linear calibration curves, since intensity can be lost in

the baseline.[14] With this in mind, IRRAS is better employed for qualitative comparisons. For aqueous samples, it is also important to subtract out contributions of water, as small fluctuations in water vapor can dominate the spectrum.

The IRRAS apparatus employed has been described previously.[15] Briefly, an IR beam from a Bruker Tensor 37 spectrometer is reflected off of two gold mirrors onto a petri dish containing an aqueous solution at an optimized height. The entire system is inside a box that can be purged to minimize water vapor interference. Purge times longer than 30 minutes were used for both a background spectrum and the spectrum of the desired solution. Typically, IRRAS data is presented as Reflectance-Absorbance, *RA*, versus wavenumber, where *RA* is defined in Equation 2.3.[16]

$$\mathrm{RA} = -\log\left(\frac{\mathrm{R}}{\mathrm{R}_0}\right) \tag{2.3}$$

Here, R is the reflectance of the sample of interest and R_0 is the reflectance of the subphase (in this case, an aqueous solution at given salt and pH conditions) in the absence of the surfactant (in this case, the amino acid). For the work described in this dissertation, peaks of interest were in higher wavenumber ranges, so baseline correction was performed by creating a linear baseline from 2831 to 2981 cm^{-1}, extrapolating across the spectrum and subtracting from the data.

2.6 Surface Tension Measurements

Surface tension, γ, was measured using an AquaPi tensiometer (Kibron) with Teflon sample cups. The dyne rod was periodically cleaned with ethanol, water, and the flame of a butane torch. The tensiometer was calibrated for milliQ water to have a reading of 72.8 mN/m at lab temperature. When γ, rather than surface pressure, is measured, temperature correction at typical lab temperatures can be achieved by linear interpolation of the two bracketing (Temperature, γ) data points between (18 °C, 73.0 mN/m), (20 °C, 72.8 mN/m), and (25 °C, 72.0 mN/m). The first reading of the tensiometer is intended to be discarded, and additional readings were taken until

readings agreed (instrumental precision is 0.1 mN/m). When a series of solutions were measured, they were measured in order of increasing concentration. In between measurements, the sample cup was rinsed with the next solution to be measured, not milliQ water, to minimize dilution.

Surface tension data can be used to calculate surface pressure, defined in Equation 2.4

$$\pi = \gamma_0 - \gamma \tag{2.4}$$

Here, π is surface pressure, γ_0 is the surface tension of a sample without a given analyte, and γ is the surface tension of a sample with an analyte. Thus, if π is positive, then the analyte lowered the surface tension, as is the case for surfactants. If π is negative, the analyte raised the surface tension, which frequently occurs for solutes. An advantage to the calculation of π is that factors that contribute equally to γ_0 and γ subtract out. As an example, consider the case where the analyte is an amino acid and the matrix is an aqueous salt solution. Many organic trace contaminants are removed from the salts used to make the aqueous solution during the baking pre-treatment process, but those that are not will make an approximately equal contribution to γ_0 and γ. The contribution may not be identical if the analyte strongly concentrates at the air-water interface, as the contaminants could potentially compete for surface adsorption sites; for amino acids, surface adsorption is relatively sparse (see Chapter 7) and this is less of a concern.

2.7 Refractive Index Measurements

The refractive index of aerosols can be calculated from WGM data as discussed previously. Due to software misidentification of reagent peaks as WGM's, refractive index data from the AOT often contains numerous data points that do not correspond to the refractive index of the aerosol. These data are sometimes obviously identified, as all the correct data falls along a predictable line while misidentifications are far from this line. Once these data are removed, the refractive index

at a given point can be calculated by averaging several values in the area of interest. For an aqueous sample, the refractive index can then be converted to concentrations using Equation 2.5.

$$R_w + x(R_s - R_w) = \frac{n^2 - 1}{n^2 + 2} * x\left(M_w + (M_s - M_w)\right) * \frac{1}{d_0 + \sum_i A_i * x^i} \qquad (2.5)$$

Here, n is the refractive index, x is the mole fraction of the solute, R_w, R_s, M_w, and M_s are the refractivities and molar masses of water and the average solute, respectively, d_0 is the density of pure water and A_i are density polynomial coefficients for the solute.[18,19] This equation has no analytical solution, so instead a series of possible concentrations can be tested until the solution producing the least difference between the left and right sides of the equation (while still being physically realistic i.e. $0 < x < 1$) is identified. Further details regarding this calculation are given in Chapter 4 and the MATLAB script that performs this calculation can be found in Appendix A.

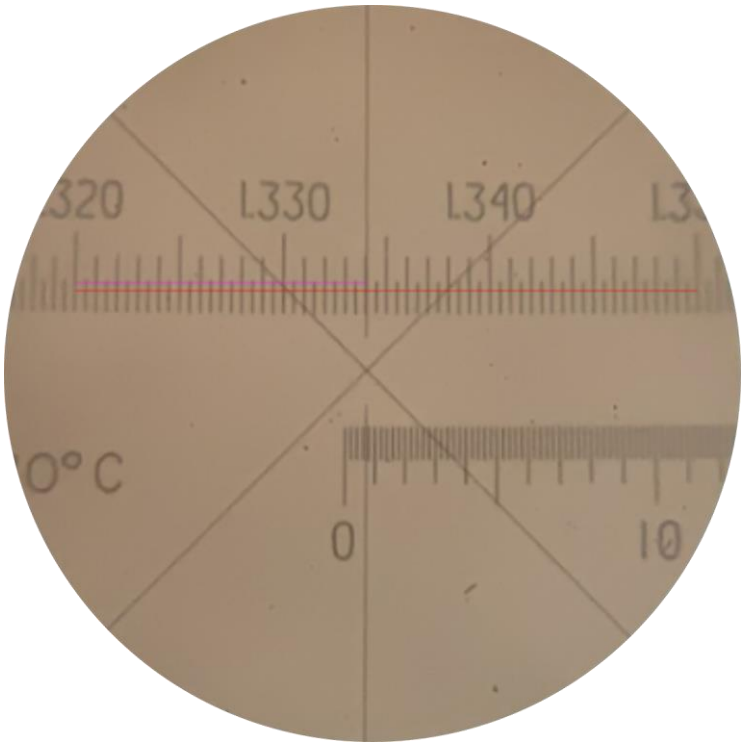

Figure 2.3: Example refractometer reading. The red line (bottom horizontal line) is drawn to determine the number of pixels in 0.03 refractive index units. The number of pixels in the fuchsia (top horizontal line) can then be used to determine the number of refractive index units to add to 1.320 to get the sample refractive index.

For bulk solutions, an ABBE-3L refractometer (Bausch & Lomb) was used. For this instrument, small volumes of solution are pipetted onto a prism and illuminated with a sodium lamp. The sample can then be aligned with a scale for a reading of refractive index. To minimize error, this process was made more quantitative by the dissertation author by taking pictures of the illuminated image with a smartphone camera. The images were then processed in Inkscape, where the pixels per refractive index unit could be determined. An example is given in Figure 2.3.

2.7 References

(1) Rafferty, A.; Preston, T. C. Trapping Positions in a Dual-Beam Optical Trap. *J. Appl. Phys.* **2021**, *130* (18), 183105.

(2) Wills, J. B.; Knox, K. J.; Reid, J. P. Optical Control and Characterisation of Aerosol. *Chem. Phys. Lett.* **2009**, *481* (4–6), 153–165.

(3) Du, J.; Yuen, C. H.; Li, X.; Ding, K.; Du, G.; Lin, Z.; Chan, C. T.; Ng, J. Tailoring Optical Gradient Force and Optical Scattering and Absorption Force. *Sci. Reports 2017 71* **2017**, *7* (1), 1–7.

(4) Mitchem, L.; Reid, J. P. Optical Manipulation and Characterisation of Aerosol Particles Using a Single-Beam Gradient Force Optical Trap. *Chem. Soc. Rev.* **2008**, *37* (4), 756–769.

(5) Pesce, G.; Jones, P. H.; Maragò, O. M.; Volpe, G. Optical Tweezers: Theory and Practice. *Eur. Phys. J. Plus 2020 13512* **2020**, *135* (12), 1–38.

(6) Symes, R.; Sayer, R. M.; Reid, J. P. Cavity Enhanced Droplet Spectroscopy: Principles, Perspectives and Prospects. *Phys. Chem. Chem. Phys.* **2004**, *6* (3), 474–487.

(7) Rafferty, A.; Gorkowski, K.; Zuend, A.; Preston, T. C. Optical Deformation of Single Aerosol Particles. *Proc. Natl. Acad. Sci. U. S. A.* **2019**, *116* (40), 19880–19886.

(8) Coddens, E. M.; Angle, K. J.; Grassian, V. H. Titration of Aerosol pH through Droplet Coalescence. *J. Phys. Chem. Lett.* **2019**, *10* (15), 4476–4483.

(9) Mael, L. E.; Peiker, G.; Busse, H. L.; Grassian, V. H. Temperature-Dependent Liquid Water Structure for Individual Micron-Sized, Supercooled Aqueous Droplets with Inclusions. *J. Phys. Chem. A* **2021**, *125* (51), 10742–10749.

(10) Rueden, C. T.; Schindelin, J.; Hiner, M. C.; DeZonia, B. E.; Walter, A. E.; Arena, E. T.; Eliceiri, K. W. ImageJ2: ImageJ for the next Generation of Scientific Image Data. *BMC Bioinformatics* **2017**, *18* (1).

(11) Craig, R. L.; Peterson, P. K.; Nandy, L.; Lei, Z.; Hossain, M. A.; Camarena, S.; Dodson, R. A.; Cook, R. D.; Dutcher, C. S.; Ault, A. P. Direct Determination of Aerosol pH: Size-Resolved Measurements of Submicrometer and Supermicrometer Aqueous Particles. *Anal. Chem.* **2018**, *90* (19), 11232–11239.

(12) Song, Q.; Osada, K. Direct Measurement of Aerosol Acidity Using pH Testing Paper and Hygroscopic Equilibrium under High Relative Humidity. *Atmos. Environ.* **2021**, *261*, 118605.

(13) Li, G.; Su, H.; Ma, N.; Zheng, G.; Kuhn, U.; Li, M.; Klimach, T.; Pöschl, U.; Cheng, Y. Multifactor Colorimetric Analysis on pH-Indicator Papers: An Optimized Approach for Direct Determination of Ambient Aerosol pH. *Atmos. Meas. Tech.* **2020**, *13* (11), 6053–6065.

(14) Carter-Fenk, K. A.; Carter-Fenk, K.; Fiamingo, M. E.; Allen, H. C.; Herbert, J. M. Vibrational Exciton Delocalization Precludes the Use of Infrared Intensities as Proxies for Surfactant Accumulation on Aqueous Surfaces. *Chem. Sci.* **2021**, *12* (24), 8320–8332.

(15) Shrestha, M.; Luo, M.; Li, Y.; Xiang, B.; Xiong, W.; Grassian, V. H. Let There Be Light: Stability of Palmitic Acid Monolayers at the Air/Salt Water Interface in the Presence and Absence of Simulated Solar Light and a Photosensitizer. *Chem. Sci.* **2018**, *9* (26), 5716–5723.

(16) Prosser, A. J.; Franses, E. I. Infrared Reflection Absorption Spectroscopy (IRRAS) of Aqueous Nonsurfactant Salts, Ionic Surfactants, and Mixed Ionic Surfactants. *Langmuir* **2002**, *18* (24), 9234–9242.

(17) Luo, M. Structure, Properties, Dynamics, and Photochemical Behavior of Organic and Biological Species in Marine-Relevant Environments, University of California, San Diego, 2021.

(18) Tang, I. N.; Tridico, A. C.; Fung, K. H. Thermodynamic and Optical Properties of Sea Salt Aerosols. *J. Geophys. Res. Atmos.* **1997**, *102* (19), 23269–23275.

(19) Tang, I. N.; Munkelwitz, H. R. Water Activities, Densities, and Refractive Indices of Aqueous Sulfates and Sodium Nitrate Droplets of Atmospheric Importance. *J. Geophys. Res.* **1994**, *99* (D9), 18801–18808.

CHAPTER 3 ACIDITY ACROSS THE INTERFACE FROM THE OCEAN SURFACE TO SEA SPRAY AEROSOL

3.1 Abstract

Aerosols impact climate, human health and the chemistry of the atmosphere and aerosol pH plays a major role in the physicochemical properties of the aerosol. However, there remains uncertainty as to whether aerosols are acidic, neutral, or basic. In this research, we show that the pH of freshly emitted (nascent) sea spray aerosols is significantly lower than that of sea water (approximately four pH units, with pH being a log scale value) and that smaller aerosol particles below 1 micron in diameter have pH values that are even lower. These measurements of nascent sea spray aerosol pH, performed in a unique ocean-atmosphere facility, provide convincing data to show that acidification occurs "across the interface" within minutes, when aerosols form from ocean surface waters and become airborne. We also show there is a correlation between aerosol acidity and dissolved carbon dioxide but no correlation with marine biology within the seawater. We discuss the mechanisms and contributing factors to this acidity and its implications on atmospheric chemistry.

3.2 Introduction

Sea spray aerosol (SSA) profoundly impact climate; however, aerosol-cloud interactions currently remain the largest source of uncertainty in climate modeling.[1] With oceans covering approximately 71% of Earth's surface, SSA significantly affect cloud properties and lifetime. Particle acidity has been shown to impact radiative forcing.[2] Aerosol pH impacts the rates of multiphase reactions, including the oxidation of aqueous SO_2 by ozone and the formation of isoprene-derived secondary organic aerosol.[3,4] Furthermore, highly acidic aerosols can increase

lung oxidative stress and adversely impact health.[5,6] Aerosol pH is difficult to measure, due to its dynamic nature and rapid response to changing environmental conditions such as relative humidity (RH). As such there have been very few direct measurements of nascent SSA pH.

Atmospheric submicron SSA pH was first reported by Winkler, who collected ambient aerosols in water, diluted, measured pH and conductivity, and extrapolated to airborne aerosol pH assuming 90% RH.[7] Depending on the extent of buffering, the resulting pH values fell between 1 and 3. Since this early study, there have been very few studies that directly measured SSA pH. This is likely due to the increasing use of thermodynamic models to calculate acidity from other measurements, as well as the difficulty of directly probing aerosol pH.[8–10] However, models predict a wide range of aerosol pH values and can be highly sensitive to experimental uncertainties such as the error associated with ammonium measurements.[11,12] For example, reports applying model calculations to field data have reported SSA pH ranging from greater than 8 to below 0 depending on the location, meteorological conditions, and assumptions used in the model.[13,14] Furthermore, ambient aerosols are a mixture of nascent and aged particles. Thus, the acidity of nascent aerosols is unknown, and direct measurements are needed. Specifically, size-resolved measurements of SSA pH are needed, since averaging pH in different particle size-fractions can lead to pH variations of up to 3 pH units.[6,15]

It is often assumed that sea spray aerosol has the same pH as seawater (~8)[16,17] and then can become acidified via mechanisms such as the uptake of acidic gases, water loss, and atmospheric aging reactions with sulfur dioxide (SO_2). Each of these processes proceeds on different timescales, with water loss occurring in seconds whereas some aging processes can take days.[18,19] Therefore, measuring the pH of *nascent* SSA is important since composition and pH vary with age. Here, we operationally define "nSSA" (nascent SSA) as SSA that has been airborne for

less than 2 minutes. To our knowledge, this is the first investigation into nSSA, and as such our study will give insight into the acidity of particles freshly emitted from the ocean.

Colorimetric pH strips have been successfully employed to sample aerosol pH but results for ambient measurements have typically been semi-quantitative at best. Ganor *et al.* (1993) were limited to the resolution of 0.5 pH units provided by the pH paper manufacturer.[20] Craig *et al.* (2018) improved the method by using quantitative image analysis, although paper color for some field samples was incompatible with their analysis script.[21] We optimized and thoroughly validated pH paper as a method to determine real world aerosol pH, and applied this technique to a sampling intensive called SeaSCAPE (Sea Spray Chemistry and Particle Evolution) where isolated sea spray aerosols were produced in a unique ocean-atmosphere facility. This study was carried out at the Hydraulics Laboratory at the Scripps Institution of Oceanography, using a sealed wave flume filled with coastal Pacific Ocean seawater obtained at 2 meters of depth from the end of the Scripps pier. A paddle mechanically generates waves that break on a simulated beach within the flume, and it has been shown this process produces a bubble size-distribution similar to that of the real ocean.[22] This facility allows for measurements of realistic nSSA in a clean and controlled environment devoid of other aerosols produced from pollution sources. Using a Micro-Orifice Uniform Deposit Impactor (MOUDI) and filters to aerodynamically distinguish aerosols in different size ranges and impacting the aerosols onto pH strips, the size-resolved acidity of nSSA has been, for the first time, directly assessed.

3.3 Methods

For size-resolved measurements, pH strips (Hydrion) were attached to aluminum foil discs with double-sided tape, then affixed to 110-R MOUDI (MSP) pucks using the associated metal rings. The MOUDI was connected to the wave channel (Hydraulics Laboratory, La Jolla CA) and

operated with rotation at 30 liters per minute. The wave channel generated nSSA. Collection of these SSA into the MOUDI typically proceeded for 1-2 hours. After collection, the MOUDI was disassembled and photographs of the pH strips were taken immediately. Images were processed using calibration curves (see Figure 3.4). For TSP measurements, the procedure was the same except filter holders were used in place of a MOUDI, a flow rate of 5.5 liters per minute was used, and collection times typically ranged 30 to 60 minutes. Sea surface microlayer pH was measured by both pH paper and a pH probe using samples obtained by dipping a glass plate in the wave channel. A suite of sensors were used to measure SSW properties including Temperature, Salinity, Chlorophyll-A (SeaBird Scientific SBE16 with Eco-Triplet BBFL2); pH (Honeywell Durafet), dissolved oxygen (Aanderaa Data Instruments 3835 Optode), pCO_2 and total dissolved inorganic carbon ("Burke-o-lator" custom IR analyzer). A high-resolution time-of-flight aerosol mass spectrometer (AMS) provided bulk speciated aerosol mass concentrations.[23] The AMS was operated in V ion path (m/ Δm) = 2500) in mass spectra (MS) and particle time of flight (PTOF) modes.

3.4 Results and Analysis

3.4.1 Results

The size dependence of nSSA pH is shown in Figure 3.1. These data are based on 106 measurements and show the general relationship of pH with aerosol aerodynamic diameter. The four leftmost bars are the results from MOUDI-separated nSSA collected at RH = 83 ± 5%, where particles from 0.1 to 1.0 microns in diameter were found to have pH values between 1.5 and 2.6. The bar labeled "TSP" (Total Suspended Particles) is the average result from filter-based measurements that collected all SSA sizes at RH = 86 ± 6%. Although strictly speaking this is a measurement of the entire SSA ensemble pH, the results are far more reflective of supermicron

pH than submicron pH since for this intensive TSP was ca. 88% supermicron nSSA by mass. Therefore, we refer to TSP as supermicron. Note that the error bars in this figure represent one standard deviation for each type of respective measurement pooled across the sampling intensive. For example, for TSP measurements, the error bar shows the standard deviation calculated from the set of all TSP measurements. Even though these are not truly replicate measurements, since the flume water composition evolved over time, showing the error bars this way gives a visual representation of the range of values obtained over the course of the intensive.

For this study, extensive control experiments were performed to verify that the pH readings from the intensive were representative of nSSA, rather than a result of experimental artifacts (e.g. Figure 3.5). Factors tested include the impact of variable salt concentration on pH paper color, the fading of pH paper color over time, the influence of gases on pH paper color, the mass loading needed for a pH reading, and the response of pH paper to various control aerosols. Notably, we

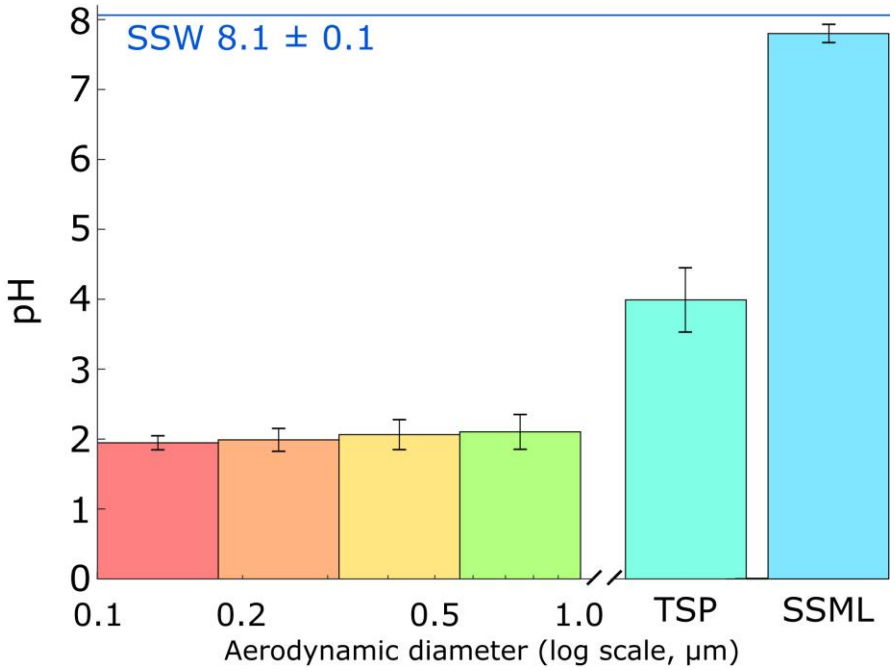

Figure 3.1: Relationship between size and pH for SSA that is then compared to the SSML and bulk SSW. Error bars and the SSW uncertainty represent 1 SD for the respective measurements across the duration of the intensive. Note that TSP is predominantly a measure of supermicron SSA pH.

found that even a 6 M change in NaCl concentration only changes the calculated submicron pH by at most 0.25 units, which is important considering that SSA of different sizes can have substantially different salt fractions.[24] Excluding this factor, the precision of the technique is ± 0.17 pH units.

Although variation of pH with size is small between the submicron size bins, the difference between supermicron and submicron pH is significant (p = 7 x 10^{-8}, 1-tailed t-test). Since submicron and supermicron SSA can have different salt concentrations, the t-test was repeated assuming the maximum possible error by adding 0.7 pH units to every submicron value and subtracting 0.7 pH units from every supermicron value. The p value resulting from the t-test is 0.001, indicating a statistically significant difference at 98%.

The pH of the sea surface microlayer (SSML) was also measured throughout the sampling intensive. The average pH was 7.8 with a standard deviation of 0.1 pH units. These results are generally consistent with past literature on SSML pH with a slight decrease versus the SSW pH of 8.1 ± 0.1, which was attributed to contact with atmospheric CO_2.[25] Calculating a paired t-test for SSML pH and SSW pH averaged during the time of SSML collection (8:30-10:30 A.M. PT) gives a p value of 3 x 10^{-8}, showing the SSML is more acidic than the SSW. Given the air velocity in the wave flume and the distance from breaking waves to sampling ports in this study, and given the controls performed to account for paper color change after deposition, for these conditions, acidification of SSA appears to occur in less than two minutes. Thus, considering that the pH of the SSML is 7.8, substantial acidification occurs rapidly to increase the activity of H^+ in these aerosols by nearly 6 orders of magnitude in this short timescale.

A notable relationship is the correlation of SSA pH with SSW partial pressure of CO_2 (pCO_2) and pH (Figure 3.2). This correlation is logical, since bulk water acidity is determined by the dissolved inorganic carbonate system, and given that there were not significant changes in temperature or salinity, the similarity in R^2 values is unsurprising. However, the slope of 4.5 pH units in SSA pH per unit change in SSW pH indicates that the relationship must be controlled by acid-base systems other than carbonic acid. The correlation is likely indicative of how both SSA and SSW pH change in response to an underlying factor. In addition, this relationship is only obtained using data points from the beginning of a phytoplankton bloom up until the flume was inoculated by the addition of separate, biologically dense water that had been obtained by the same method but kept out in sunlight to help induce biological activity. This inoculation turned the flume water greener and had a substantial impact on SSW chemical composition including a SSW $[H^+]$ decrease of over 30% from the average pre-inoculation levels. When data points from this perturbation are included, the R^2 correlation coefficients of nSSA pH with pCO_2 and SSW pH become 0.03 and 0.04, respectively. Therefore, we tentatively hypothesize that nSSA pH is more

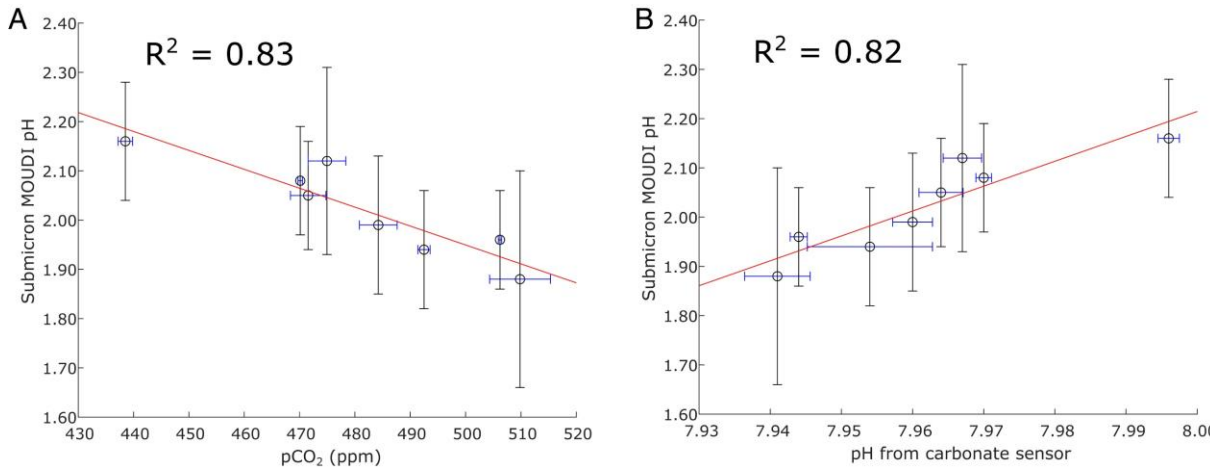

Figure 3.2: (A) Inverse correlation between SSA pH and pCO_2; (B) correlation between SSA pH and seawater pH as calculated from pCO_2, dissolved inorganic carbon, temperature, and salinity. Data span from the addition of new seawater to the flume to perturbation by external inoculation. Horizontal error bars show 1 SD from minute averages during the corresponding MOUDI sampling time. Vertical error bars show 1 SD in nSSA pH calculated from different spots on the same pH strip.

predictable from CO_2 levels and ion concentrations when biological activity is minimal, while water with dense biological activity features more complicated pH relationships. Furthermore, as CO_2 levels increase in the atmosphere, these data show for the first time the potential for aerosols produced from ocean waters to be even more acidic.

At this time, we have not identified a single biological parameter that is predictive of nSSA pH. Further, while the microbial loop may impact aerosol pH, the impact is relatively small, as shown by the general stability of nSSA pH across substantial changes in phytoplankton and microbial activity as estimated by chlorophyll-a concentrations (Figure 3.3).

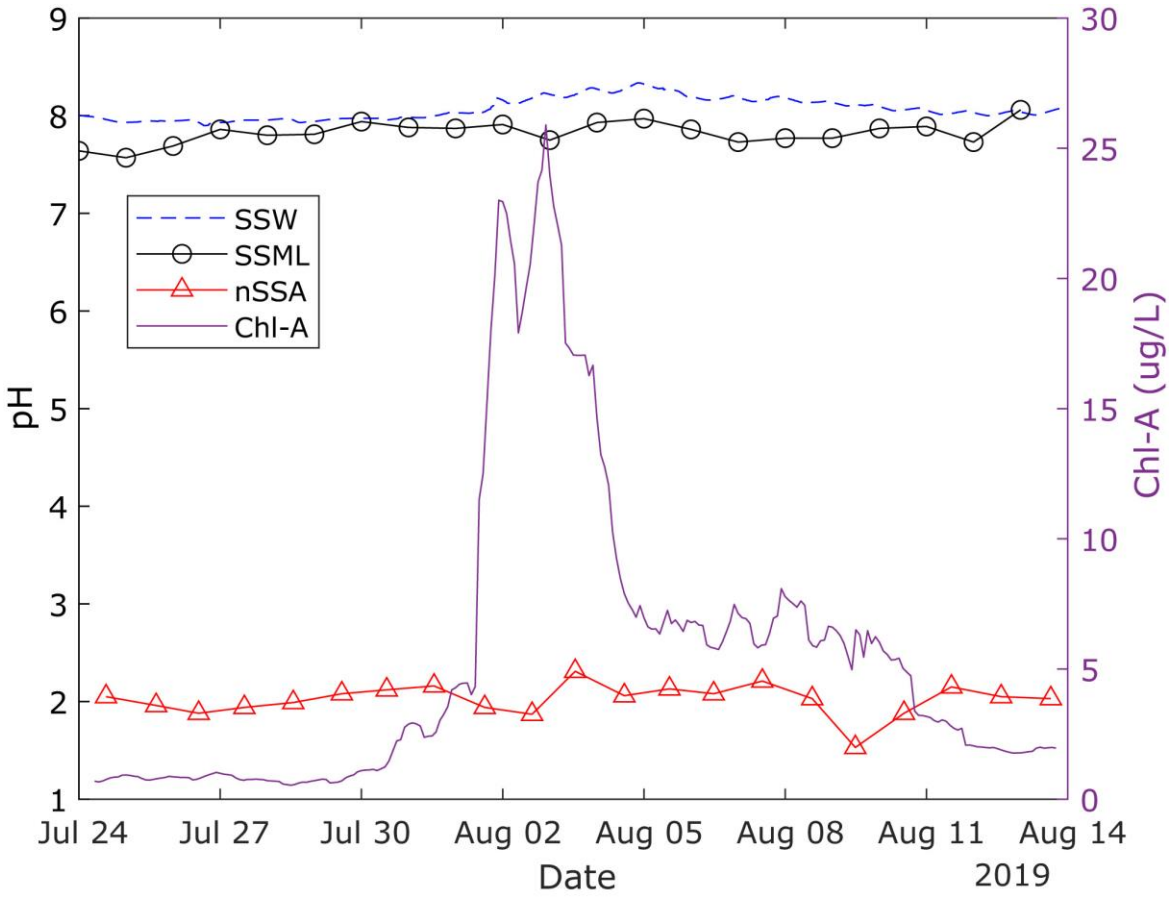

Figure 3.3: Time series of pH and chlorophyll a (Chl-a) measurements. Bulk seawater (SSW) pH, SSML pH, and nSSA pH from MOUDI stage 7 are plotted on the left-hand axis, and Chl-a concentration is plotted on the right-hand axis. The SSW and Chl-a traces reflect averages over every minute and 2 h, respectively, while symbols denote SSML and nSSA measurements.

3.4.2 Acidity Across the Interface

The results obtained here indicate that submicron aerosols obtain low pH rapidly after ejection from the ocean into the atmosphere. It has been suggest that this acidity in remote marine areas occurs in less than 15 minutes and perhaps even as fast as seconds.[26–28] Here using a unique ocean-wave facility, we can definitively conclude that nSSA is acidic within the timescale of two-minute and that the acidity is volume (size) dependent.

The large change in acidity from supermicron to submicron SSA has been previously discussed. Fridlind and Jacobson (2000) calculated for a model marine boundary layer that *sub*micron SSA comes to equilibrium with acidic gases within seconds, while hours are required for equilibrium with bases; for *super*micron SSA, the opposite is true.[29] The difference in acidity also follows from consideration of the surface area to volume (SA:V) ratios of these SSA. The buffering capacity of a single SSA is proportional to its volume, while the rate of acid uptake (assuming a constant accommodation coefficient) is related to its surface area. Therefore, the buffering capacity is overwhelmed more rapidly for high SA:V and hence submicron SSA are more quickly acidified. The different mechanisms of formation also likely contribute to the acidity difference. Supermicron SSA are mainly formed from jet drops, while submicron are mainly formed from both film and jet drops, with film drops having a greater enrichment of organic acids.[30] It is possible that the submicron SSA collected here were an external mixture of low pH (0-2) film drops and higher pH (2-4) jet drops, but future studies are needed to isolate these phenomena.[31] We also emphasize that higher pH values would be observed in regions where dust or ammonia make a substantial contribution and neutralizes SSA acidity.[32,33]

It is worth noting that all submicron size bins had similar pH averages. Although Figure 3.1 shows an apparent trend of slightly decreasing pH with diameter, the differences are not

statistically significant at 95% confidence. Past investigators have found that at pH = 2, the rates of acid uptake and HCl release are nearly equal for SSA, effectively buffering the aerosols at this pH.[29] These results were obtained from a model of a remote marine boundary layer, removing the effects of further acidifying pollution and neutralizing mineral dust, and hence are similar to the conditions created here.[13,14,26] It has also recently been shown by Zheng *et al.* (2020) that the sulfate/bisulfate system buffers at pH ~2 in aqueous solutions as well as aerosols, which could further contribute to buffering at this level.[33]

Quantification of SSA pH is key to understanding various atmospheric chemical transformations. For example, hydrolysis of organic nitrates also occurs faster at lower pH.[34] By contrast, the brown-carbon-forming reaction of glyoxal with amines is influenced by the proportion of unprotonated amines, leading to slower rates at lower pH.[35] Many other examples exist, and it is clear that reactions that are important at the basic pH of seawater may be negligible at the highly acidic pH of submicron nSSA, and vice versa.[12] For example, one particularly important atmospheric process with pH-dependence is the oxidation of SO_2. This reaction produces sulfate and hence is important for predicting radiative forcing, and the fate of SO_2 depends strongly on the acidity of its environment. First, the effective Henry's law coefficient of SO_2 is over 6 orders of magnitude larger (in units of M/atm) at pH 8 vs pH 2, indicating it will partition into submicron nSSA to a significantly lesser extent than previously thought.[19] Combining Henry's law coefficient variability with kinetic parameters, Liang and Jacobson (1999) calculated that for pH = 8 SSA, 100 times more sulfate would be formed in the aqueous phase than the gas phase; for the same liquid water content at pH = 2, more sulfate would be formed in the gas phase instead.[36] Second, the aqueous-phase oxidation of SO_2 has a highly-complex pH dependence, proceeding by entirely different mechanisms for pH < 5 than for pH > 5.[37]

Additionally, a rapid pathway of interfacial oxidation of SO_2 has been identified for aerosols with pH < 3.5.[38] Our data thus indicates this pathway is possible for submicron nSSA within minutes after its formation. Therefore, given the substantial contribution of SSA to atmospheric particulate mass and the pH-dependence of the key SO_2 oxidation reaction, knowledge of the high acidity of nSSA is critical to accurately calculating the pathway and extent of sulfate formation and the subsequent impact on climate properties.

A compilation of pH ranges for marine aerosols is given in Table 3.1.

Table 3.1: Compilation of selected submicron and supermicron marine aerosol pH values.

Description	Sub-µm pH	Super-µm pH	Ref.
Aerosol leeching solutions from Hamburg, measured after dilution	1-3	4-8	7
Southern Ocean, calculated by an equilibrium model	0-2	2-5	29
Moderately polluted Bermuda, measured with minimal dilution	-1.1-3.2	1.2 to ≥ 5.6	14
Hawaiian marine boundary layer, inferred from phase partitioning	2.6-5.3	4.5-5.4	28
Hawaiian after volcanic plume, measurement-constrained ISORROPIA	-0.8-3.0	N/A	39
Eastern Mediterranean, calculated from measurement of LWC	-0.2-1.1	~7†	13
Various Southern Ocean locations, $PM_{2.5}$, calculated by ISORROPIA	N/A	0.5-4.1	40
This work	1.5-2.6	3.5-4.7	41

† = PM_{10}; reported as less quantitative than the corresponding sub-µm measurement.

These values span similar ranges to our findings, however, these other results are obtained from mixtures of nascent, atmospherically aged, and secondary marine aerosols. The low pH of aged SSA is often attributed to anthropogenic pollution, radicals, and oxidation of dimethyl sulfide to sulfur dioxide and sulfuric acid,[13,14,16,42] but those factors do not contribute to conditions here. Instead, the results shown here indicate acidification happens much more quickly. The prior studies, from field measurements, were not able to isolate nascent SSA due to the nature of the

measurements whereas here we measured real world samples in a controlled environment by bringing the "ocean into the lab" as described in Prather et al.[22] This allows for the determination that there are most likely *several* contributing mechanisms to the observed acidity of nSSA.

3.4.3 Factors Contributing to Low nSSA pH

Relative humidity is an important factor in assessing aerosol pH. Using readings from RH sensors before the MOUDI inlet and near the TSP filters, it was found that measured RH does not correlate ($R^2 = 0.01$) with submicron pH. By contrast, the pH of supermicron SSA does correlate ($R^2 = 0.65$) with RH. Past calculations have indicated that submicron marine boundary layer aerosol pH only weakly corresponds to RH, where supermicron aerosol pH has a stronger dependence, which is in agreement with the findings here.[29] This does not necessarily mean that RH plays no role in submicron aerosol pH, but rather, that there are additional factors impacting pH.[43,44] It is also worth noting that the RH range in question as measured at the MOUDI only spans 72-89%, so at much lower RH, clearer trends of submicron SSA pH with water loss may be observed. The average RH values for the MOUDI, filters, and flume near particle generation were 83%, 86%, and 93% respectively. Based on a typical growth factor curve for sodium chloride, the pH impact due to water loss moving from the site of generation to sampling was calculated. For the MOUDI and TSP filters, the pH of the measured nSSA before decreasing due to water loss would have been 0.3 and 0.2 units higher, respectively.[45] Since RH data were only available for approximately half of the pH data points, and because this change is small, this correction was not applied to the data shown in Figure 3.1 for consistency. However, for SSA over the real ocean, this factor may be more significant, as some of the lowest pH values (0 to -4) have been reported for conditions of low RH and high sulfate or organic concentrations.[12,13]

A second cause of acidic pH for nSSA to consider is the lowering of droplet pH by acidic gases. The headspace air used for SeaSCAPE was passed through chemical and particulate filters designed to scrub volatile organic compounds, nitrogen oxides, and particulates including non-nSSA aerosols, however they were unable to remove these species entirely (averaged over MOUDI collection times, the concentrations of NOx and O_3 were 0.9±0.8 and 20±7 ppbv, respectively). It has been shown from model calculations that levels of HCl in the hundreds of part per trillion range can acidify SSA pH by several units at 95% RH.[29] Acidic gases at typical coastal concentrations could quickly bring nSSA to pH ~2-4, and the timescales associated with these processes are generally on the order of seconds to minutes for submicron SSA.[19,26,29,32,46,47] Calculations show that 3-4 ppb total acidic gases would be sufficient to account for the pH values reported in this study. Due to logistical limitations, nitric acid and HCl concentrations were not measured, so the extent that acidic gases (or N_2O_5 converted to HNO_3) contributed to nSSA pH remains unknown. Additionally, controls were performed to rule out the changing of pH paper color due to direct interactions between the paper and the gases from the flume.

Another source of acidity that may be particularly relevant to submicron aerosol pH is the dissociation of organic acids.[24,31] Surface active species, particularly organics, are enriched in the aerosol phase, predominately in smaller particles.[48] For a 200 nm diameter SSA with a surface layer of palmitic acid with a mean molecular area of 22 $Å^2$, only 4.4% acid dissociation is required to lower pH from 8 to 2. Although weak fatty acids typically dissociate only ~1% on their own, high concentrations of NaCl can shift acid pK_a values and increase dissociation as Na^+ ions compete with H^+ for binding.[49,50] Since SSA often have higher concentrations of salt than the SSW and SSML, this cation-assisted dissociation becomes more important as the molecules are transferred across the ocean-air interface.[51] Further, as water is lost after the SSA are emitted from

the ocean, the resulting simultaneous concentration of organic acids and NaCl could enhance this phenomenon and lead to deprotonation that significantly impacts SSA pH. Given that it is known that surface active species are enriched at and across the air/water interface,[48] it is reasonable that this enrichment impacts the change in pH across this interface upon aerosol formation.[49]

Finally, as a point of comparison, we applied the Extended Aerosol Inorganics Model (E-AIM) to data from a High-Resolution Aerosol Mass Spectrometer (HR-AMS) to estimate aerosol pH.[23] We used Inorganic Model II, which uses concentrations of H^+, NH_4^+, SO_4^{2-}, NO_3^- and H_2O as inputs.[43,52,53] The observed NH_4^+ was low and near the limit of detection, and the AMS is unable to quantitatively measure refractory components (i.e. NaCl). To this end, we performed two set of calculations. First, we used the observed values, which gave calculated aerosol pH -0.62 ± 0.07. Separately, we enhanced NH_4^+ to neutralize SO_4^{2-} (to act as a proxy for the unobserved cations; on average this increased the NH_4^+ input by a factor of 2.1) which gave calculated aerosol pH -0.1 ± 0.3. These pH values should not be taken as the quantitative equilibrium acidity of these particles: using E-AIM without gas-phase inputs can yield highly variable results,[8] and we acknowledge that the enhancing NH_4^+ to approximate unmeasured cations is imperfect. Additionally, these pH values may be low because all sulfate is assumed to be inorganic when a fraction may instead originate from organosulfur compounds.[54] Even so, these results emphasize that the AMS observations and associated calculations do support the major conclusion of this work that submicron nSSA are highly acidic.

Combining the sudden drop in pH with the substantial increase in concentration that these aerosols undergo due to water loss, nSSA could serve as micro-reactors for chemical reactions that do not occur in SSW. Further, considering the lifespan of submicron SSA is on the order of days, these aerosols are only alkaline for a nearly negligible portion of their existence immediately after

ejection from the ocean, and subsequently remain highly acidic until further processing such as coalescence or deposition.[55] Therefore, models of submicron SSA should treat nSSA as acidic, rather than pH ca. 8, since the former is a far better representation of the chemical environment inside these aerosols for the vast majority of their atmospheric lifetimes. This in turn will impact the chemical composition both inside the aerosols and in the atmosphere, as particle pH influences aerosol/gas partitioning and the fate of pollutants such as SO_2.[38]

Overall, the pH of isolated nSSA has been directly measured for the first time under controlled conditions. The aerosol is highly acidic, showing that even freshly emitted sea spray aerosol has a substantially lower pH than the bulk seawater. Additionally, these findings show that size-resolved submicron aerosol pH can be measured within hours to help capture variations in pH as other conditions evolve. From seawater to the sea surface microlayer to super and sub-micron aerosol, a trend with pH and volume becomes clear. The increasing acidity with decreasing volume may be due to a variety of phenomena, such enrichment of acidic organic species. Regardless of the cause, this abrupt and clear decrease in pH across the ocean-air interface has important implications for various processes, including acid-catalyzed chemical reactions, S(IV) oxidation, and surface partitioning of gases in the aerosol. Most importantly, these results show nSSA is acidified within minutes of aerosol formation without interaction with high levels of pollution that are typically considered to be important for aerosol acidification. These measurements of nSSA acidity inform models calculating the rate of critical atmospheric chemical transformations.

3.5 Acknowledgements

Chapter 3, in part, is a reprint of the material published by The Proceedings of the National Academy of Sciences of the United States of America in: Angle, Kyle; Crocker, Daniel; Simpson, Rebecca; Mayer, Kathryn; Garofalo, Lauren; Moore, Alexia; Mora Garcia, Stephanie; Or, Victor;

Srinivasan, Sudarshan; Farhan, Mahum; Sauer, Jon; Lee, Christopher; Pothier, Matson; Farmer, Delphine; Martz, Todd; Bertram, Timothy; Cappa, Christopher; Prather, Kimberly; Grassian, Vicki, Acidity Across the Interface from the Ocean Surface to Sea Spray Aerosols in 2020. The dissertation author was the primary investigator and author of this paper.

The authors would like to thank the entire SeaSCAPE team for help and support throughout the sampling intensive with special thanks to Chathuri Kaluarachchi and Hansol Lee for assistance with the MOUDI, Michael Sullivan for assistance in pre-intensive preparation, and Stephanie Smith for setting up the carbonate analyzer. We would also like to thank Dr. Heather Allen and Dr. Gil Nathanson for helpful discussion on the organic acid dissociation calculation. This work was funded by the National Science Foundation (NSF) through the NSF Center for Aerosol Impacts on Chemistry of the Environment (CAICE) under Grant no. CHE-1801971.

3.6 Appendix

Supporting discussions, calculations, figures, tables, and additional controls can be found free of charge in the Supporting Information of the publication corresponding to this chapter.[41]

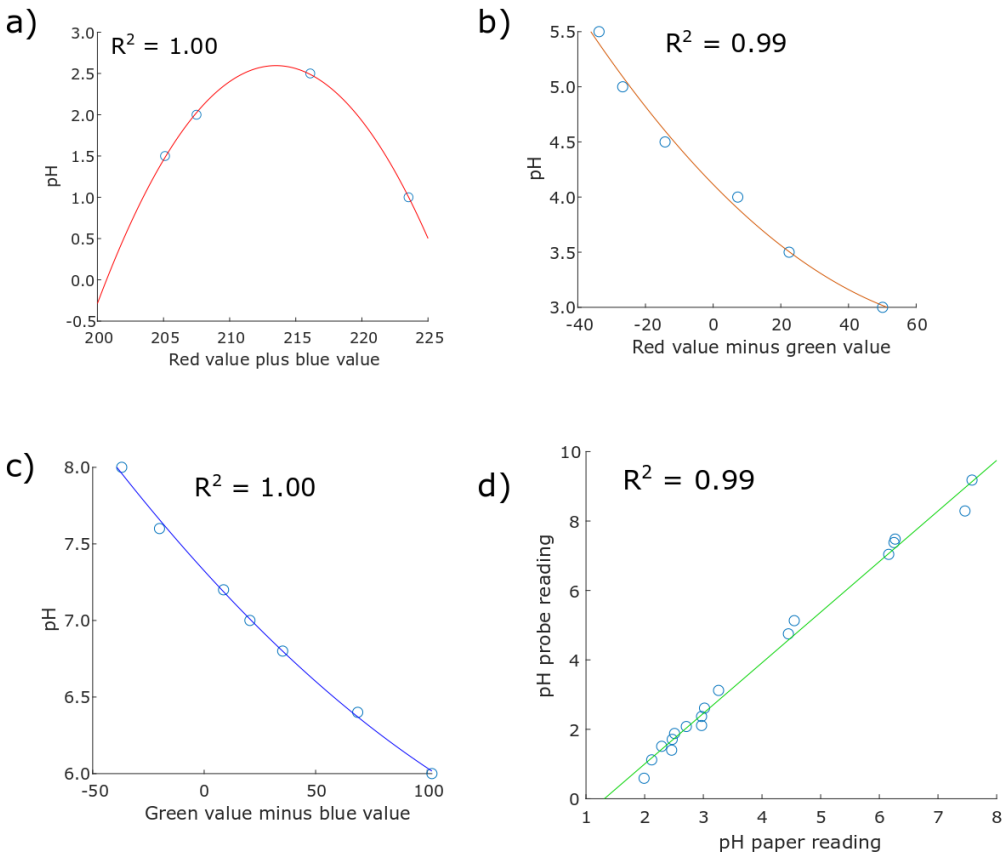

Figure 3.4: Representative calibration curves. Plots (a), (b), and (c) are created from pH papers spanning the pH 1-2.5, 3-5.5, and 6-8 ranges, respectively. A calibration curve of one of these types was created for every image of pH paper using the color scale included in the photograph. Plot (d) is a correction from pH paper reading to true pH as measured for bulk Pacific seawater adjusted to various pH levels.

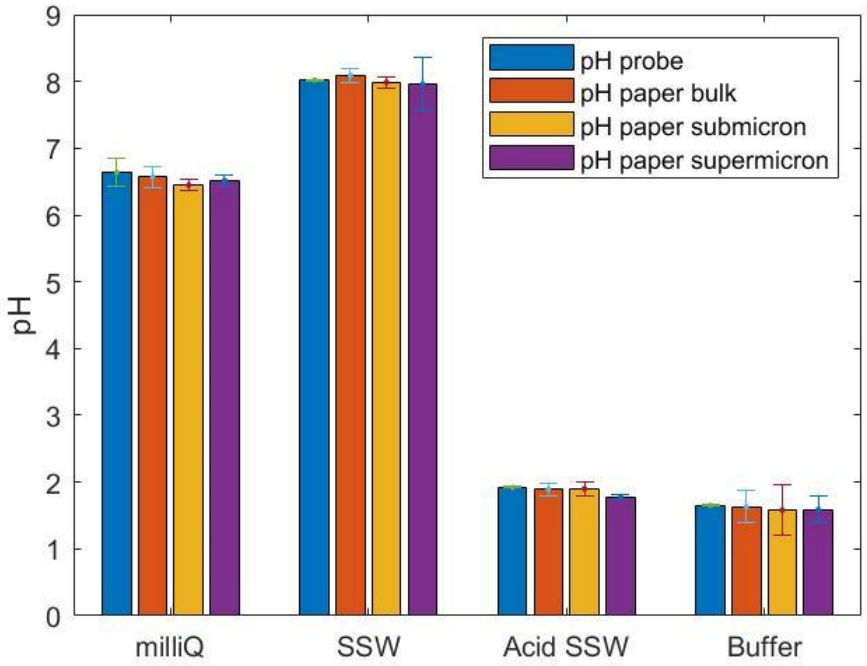

Figure 3.5: Results of control experiments. Four components were investigated: ultrapure milliQ water; subsurface bulk seawater from the wave flume; subsurface water that was acidified to pH 1.92 with HCl; and pH 1.66 buffer. Note the error bar for the pH probe reading of milliQ water has been expanded to account for the fact that KCl had to be added to the sample to stabilize the pH probe reading.

3.7 References

(1) Randall, D.; Artaxo, P.; Bretherton, C.; Feingold, G.; Forster, P.; Kerminen, V.; Kondo, Y.; Liao, H.; Lohmann, U.; Rasch, P.; Satheesh, S.; Sherwood, S.; Stevens, B.; Zhang, X.; Qin, D.; Plattner, G.; Tignor, M.; Allen, S.; Boschung, J.; Nauels, A.; Xia, Y.; Bex, V.; Midgley, P.; Boucher, O.; Randall, D. *Clouds and Aerosols. In: Climate Change 2013: The Physical Science Basis. Contribution of Working Group I to the Fifth Assessment Report of the Intergovernmental Panel on Climate Change*; 2013.

(2) Duan, J.; Lyu, R.; Wang, Y.; Xie, X.; Wu, Y.; Tao, J.; Cheng, T.; Liu, Y.; Peng, Y.; Zhang, R.; He, Q.; Ga, W.; Zhang, X.; Zhang, Q. Particle Liquid Water Content and Aerosol Acidity Acting as Indicators of Aerosol Activation Changes in Cloud Condensation Nuclei (CCN) during Pollution Eruption in Guangzhou of South China. *Aerosol Air Qual. Res.* **2019**, *19*, 2662–2670.

(3) Alexander, B.; Park, R. J.; Jacob, D. J.; Li, Q. B.; Yantosca, R. M.; Savarino, J.; Lee, C. C. W.; Thiemens, M. H. Sulfate Formation in Sea-Salt Aerosols: Constraints from Oxygen Isotopes. *J. Geophys. Res. D Atmos.* **2005**, *110* (10), 1–12.

(4) Zhang, Y.; Chen, Y.; Lei, Z.; Olson, N.; Riva, M.; Koss, A. R.; Zhang, Z.; Gold, A.; Jayne, J. T.; Worsnop, D. R.; Onasch, T. B.; Kroll, J. H.; Turpin, B. J.; Ault, A. P.; Surratt, J. D. Joint Impacts of Acidity and Viscosity on the Formation of Secondary Organic Aerosol from Isoprene Epoxydiols (IEPOX) in Phase Separated Particles. *ACS Earth Sp. Chem.* **2019**, *3* (12), 2646–2658.

(5) Freedman, M. A.; Ott, E.-J. E.; Marak, K. E. Role of pH in Aerosol Processes and Measurement Challenges. *J. Phys. Chem. A* **2019**, *123* (7), 1275–1284.

(6) Fang, T.; Guo, H.; Zeng, L.; Verma, V.; Nenes, A.; Weber, R. J. Highly Acidic Ambient Particles, Soluble Metals, and Oxidative Potential: A Link between Sulfate and Aerosol Toxicity. *Environ. Sci. Technol.* **2017**, *51* (5), 2611–2620.

(7) Winkler, P. Relations between Aerosol Acidity and Ion Balance. In *Chemistry of Multiphase Atmospheric Systems*; Springer Berlin Heidelberg, 1986; pp 269–298.

(8) Hennigan, C. J.; Izumi, J.; Sullivan, A. P.; Weber, R. J.; Nenes, A. A Critical Evaluation of Proxy Methods Used to Estimate the Acidity of Atmospheric Particles. *Atmos. Chem. Phys.* **2015**, *15* (5), 2775–2790.

(9) Coddens, E. M.; Angle, K. J.; Grassian, V. H. Titration of Aerosol pH through Droplet Coalescence. *J. Phys. Chem. Lett.* **2019**, *10* (15), 4476–4483.

(10) Lipfert, F. W.; Morris, S. C.; Wyzga, R. E. Acid Aerosols: The next Criteria Air Pollutant? *Environ. Sci. Technol* **1989**, *23* (11), 1316–1322.

(11) Guo, H.; Nenes, A.; Weber, R. J. The Underappreciated Role of Nonvolatile Cations in Aerosol Ammonium-Sulfate Molar Ratios. *Atmos. Chem. Phys.* **2018**, *18*, 17307–17323.

(12) Pye, H. O. T.; Nenes, A.; Alexander, B.; Ault, A. P.; Barth, M. C.; Clegg, S. L.; Collett, J. L.; Fahey, K. M.; Hennigan, C. J.; Herrmann, H.; Kanakidou, M.; Kelly, J. T.; Ku, I.-T.; Mcneill, V. F.; Riemer, N.; Schaefer, T.; Shi, G.; Tilgner, A.; Walker, J. T.; Wang, T.; Weber, R.; Xing, J.; Zaveri, R. A.; Zuend, A. The Acidity of Atmospheric Particles and Clouds. *Atmos. Chem. Phys.* **2020**, *20*, 4809–4888.

(13) Bougiatioti, A.; Nikolaou, P.; Stavroulas, I.; Kouvarakis, G.; Weber, R.; Nenes, A.; Kanakidou, M.; Mihalopoulos, N. Particle Water and pH in the Eastern Mediterranean: Source Variability and Implications for Nutrient Availability. *Atmos. Chem. Phys* **2016**, *16*, 4579–4591.

(14) Keene, W. C.; Pszenny, A. A. P.; Maben, J. R.; Sander, R. Variation of Marine Aerosol Acidity with Particle Size. *Geophys. Res. Lett.* **2002**, *29* (7), 5.1-5.4.

(15) Ludwig, J.; Klemm, O. Acidity of Size-Fractionated Aerosol Particles. *Water. Air. Soil Pollut.* **1990**, *49* (1–2), 35–50.

(16) Katoshevski, D.; Nenes, A.; Seinfeld, J. H. A Study of Processes That Govern the Maintenance of Aerosols in the Marine Boundary Layer. *J. Aerosol Sci.* **1999**, *30* (4), 503–

532.

(17) Carter-Fenk, K. A.; Allen, H. C. Collapse Mechanisms of Nascent and Aged Sea Spray Aerosol Proxy Films. *Atmosphere (Basel).* **2018**, *9* (12), 1–16.

(18) Rovelli, G.; Miles, R. E. H.; Reid, J. P.; Clegg, S. L. Accurate Measurements of Aerosol Hygroscopic Growth over a Wide Range in Relative Humidity. *J. Phys. Chem. A* **2016**, *120* (25), 4376–4388.

(19) Seinfeld, J. H.; Pandis, S. N. Chemistry of the Atmospheric Aqueous Phase. In *Atmospheric Chemistry and Physics: From Air Pollution to Climate Change*; John Wiley & Sons, Inc.: Hoboken, NJ, 2016.

(20) Ganor, E.; Levin, Z.; Pardess, D. Determining the Acidity and Chemical Composition of Fog, Haze and Cloud Droplets in Israel. *Atmos. Environ. Part A, Gen. Top.* **1993**, *27* (12), 1821–1832.

(21) Craig, R. L.; Peterson, P. K.; Nandy, L.; Lei, Z.; Hossain, M. A.; Camarena, S.; Dodson, R. A.; Cook, R. D.; Dutcher, C. S.; Ault, A. P. Direct Determination of Aerosol PH: Size-Resolved Measurements of Submicrometer and Supermicrometer Aqueous Particles. *Anal. Chem.* **2018**, *90* (19), 11232–11239.

(22) Prather, K. A.; Bertram, T. H.; Grassian, V. H.; Deane, G. B.; Stokes, M. D.; DeMott, P. J.; Aluwihare, L. I.; Palenik, B. P.; Azam, F.; Seinfeld, J. H.; Moffet, R. C.; Molina, M. J.; Cappa, C. D.; Geiger, F. M.; Roberts, G. C.; Russell, L. M.; Ault, A. P.; Baltrusaitis, J.; Collins, D. B.; Corrigan, C. E.; Cuadra-Rodriguez, L. A.; Ebben, C. J.; Forestieri, S. D.; Guasco, T. L.; Hersey, S. P.; Kim, M. J.; Lambert, W. F.; Modini, R. L.; Mui, W.; Pedler, B. E.; Ruppel, M. J.; Ryder, O. S.; Schoepp, N. G.; Sullivan, R. C.; Zhao, D. Bringing the Ocean into the Laboratory to Probe the Chemical Complexity of Sea Spray Aerosol. *Proc. Natl. Acad. Sci. U. S. A.* **2013**, *110* (19), 7550–7555.

(23) DeCarlo, P. F.; Kimmel, J. R.; Trimborn, A.; Northway, M. J.; Jayne, J. T.; Aiken, A. C.; Gonin, M.; Fuhrer, K.; Horvath, T.; Docherty, K. S.; Worsnop, D. R.; Jimenez, J. L. Field-Deployable, High-Resolution, Time-of-Flight Aerosol Mass Spectrometer. *Anal. Chem.* **2006**, *78* (24), 8281–8289.

(24) Bertram, T. H.; Cochran, R. E.; Grassian, V. H.; Stone, E. A. Sea Spray Aerosol Chemical Composition: Elemental and Molecular Mimics for Laboratory Studies of Heterogeneous and Multiphase Reactions. *Chem. Soc. Rev.* **2018**, *47* (7), 2374–2400.

(25) Zhang, Z.; Cai, W.; Liu, L.; Liu, C.; Chen, F. Direct Determination of Thickness of Sea Surface Microlayer Using a pH Microelectrode at Original Location. *Sci. China, Ser. B Chem.* **2003**, *46* (4), 339–351.

(26) Keene, W. C.; Sander, R.; Pszenny, A. A. P.; Vogt, R.; Crutzen, P. J.; Galloway, J. N. Aerosol pH in the Marine Boundary Layer: A Review and Model Evaluation. *J. Aerosol Sci.* **1998**, *29* (3), 339–356.

(27) Salter, M. E.; Hamacher-Barth, E.; Leck, C.; Werner, J.; Johnson, C. M.; Riipinen, I.; Nilsson, E. D.; Zieger, P. Calcium Enrichment in Sea Spray Aerosol Particles. *Geophys. Res. Lett.* **2016**, *43* (15), 8277–8285.

(28) Pszenny, A. A. P.; Moldanová, J.; Keene, W. C.; Sander, R.; Maben, J. R.; Martinez, M.; Crutzen, P. J.; Perner, D.; Prinn, R. G. Halogen Cycling and Aerosol pH in the Hawaiian Marine Boundary Layer. *Atmos. Chem. Phys* **2004**, *4*, 147–168.

(29) Fridlind, A. M.; Jacobson, M. Z. A Study of Gas-Aerosol Equilibrium and Aerosol pH in the Remote Marine Boundary Layer during the First Aerosol Characterization Experiment (ACE 1). *J. Geophys. Res. Atmos.* **2000**, *105* (D13), 17325–17340.

(30) Cochran, R. E.; Laskina, O.; Trueblood, J. V.; Estillore, A. D.; Morris, H. S.; Jayarathne, T.; Sultana, C. M.; Lee, C.; Lin, P.; Laskin, J.; Laskin, A.; Dowling, J. A.; Qin, Z.; Cappa, C. D.; Bertram, T. H.; Tivanski, A. V.; Stone, E. A.; Prather, K. A.; Grassian, V. H. Molecular Diversity of Sea Spray Aerosol Particles: Impact of Ocean Biology on Particle Composition and Hygroscopicity. *Chem* **2017**, *2* (5), 655–667.

(31) Wang, X.; Deane, G. B.; Moore, K. A.; Ryder, O. S.; Stokes, M. D.; Beall, C. M.; Collins, D. B.; Santander, M. V.; Burrows, S. M.; Sultana, C. M.; Prather, K. A. The Role of Jet and Film Drops in Controlling the Mixing State of Submicron Sea Spray Aerosol Particles. *Proc. Natl. Acad. Sci. U. S. A.* **2017**, *114* (27), 6978–6983.

(32) Shi, G.; Xu, J.; Peng, X.; Xiao, Z.; Chen, K.; Tian, Y.; Guan, X.; Feng, Y.; Yu, H.; Nenes, A.; Russell, A. G. pH of Aerosols in a Polluted Atmosphere: Source Contributions to Highly Acidic Aerosol. *Environ. Sci. Technol.* **2017**, *51* (8), 4289–4296.

(33) Zheng, G.; Su, H.; Wang, S.; Andreae, M. O.; Pöschl, U.; Cheng, Y. Multiphase Buffer Theory Explains Contrasts in Atmospheric Aerosol Acidity. *Science* **2020**, *369* (6509), 1374–1377.

(34) Rindelaub, J. D.; Borca, C. H.; Hostetler, M. A.; Slade, J. H.; Lipton, M. A.; Slipchenko, L. V.; Shepson, P. B. The Acid-Catalyzed Hydrolysis of an α -Pinene-Derived Organic Nitrate: Kinetics, Products, Reaction Mechanisms, and Atmospheric Impact. *Atmos. Chem. Phys.* **2016**, *16* (23), 15425–15432.

(35) Sedehi, N.; Takano, H.; Blasic, V. A.; Sullivan, K. A.; De Haan, D. O. Temperature- and PH-Dependent Aqueous-Phase Kinetics of the Reactions of Glyoxal and Methylglyoxal with Atmospheric Amines and Ammonium Sulfate. *Atmos. Environ.* **2013**, *77*, 656–663.

(36) Liang, J.; Jacobson, M. Z. A Study of Sulfur Dioxide Oxidation Pathways over a Range of Liquid Water Contents, pH Values, and Temperatures. *J. Geophys. Res.* **1999**, *104* (D11), 749–762.

(37) Brandt, C.; van Eldik, R. Transition Metal-Catalyzed Oxidation of Sulfur(IV) Oxides: Atmospheric-Relevant Processes and Mechanisms. *Chem. Rev.* **1995**, *95* (1), 119–190.

(38) Hung, H. M.; Hsu, M. N.; Hoffmann, M. R. Quantification of SO_2 Oxidation on Interfacial

Surfaces of Acidic Micro-Droplets: Implication for Ambient Sulfate Formation. *Environ. Sci. Technol.* **2018**, *52* (16), 9079–9086.

(39) Kroll, J. H.; Cross, E. S.; Hunter, J. F.; Pai, S.; Wallace, L. M. M.; Croteau, P. L.; Jayne, J. T.; Worsnop, D. R.; Heald, C. L.; Murphy, J. G.; Frankel, S. L. Atmospheric Evolution of Sulfur Emissions from Kilauea: Real-Time Measurements of Oxidation, Dilution, and Neutralization within a Volcanic Plume. *Environ. Sci. Technol.* **2015**, *49* (7), 4129–4137.

(40) Dall'Osto, M.; Airs, R. L.; Beale, R.; Cree, C.; Fitzsimons, M. F.; Beddows, D.; Harrison, R. M.; Ceburnis, D.; O'Dowd, C.; Rinaldi, M.; Paglione, M.; Nenes, A.; Decesari, S.; Simó, R. Simultaneous Detection of Alkylamines in the Surface Ocean and Atmosphere of the Antarctic Sympagic Environment. *ACS Earth Sp. Chem.* **2019**, *3* (5), 854–862.

(41) Angle, K. J.; Crocker, D. R.; Simpson, R. M. C.; Mayer, K. J.; Garofalo, L. A.; Moore, A. N.; Mora Garcia, S. L.; Or, V. W.; Srinivasan, S.; Farhan, M.; Sauer, J. S.; Lee, C.; Pothier, M. A.; Farmer, D. K.; Martz, T. R.; Bertram, T. H.; Cappa, C. D.; Prather, K. A.; Grassian, V. H. Acidity across the Interface from the Ocean Surface to Sea Spray Aerosol. *Proc. Natl. Acad. Sci.* **2021**, *118* (2), e2018397118.

(42) Wang, S.; Maltrud, M.; Elliott, S.; Cameron-Smith, P.; Jonko, A. Influence of Dimethyl Sulfide on the Carbon Cycle and Biological Production. *Biogeochemistry* **2018**, *138* (1), 49–68.

(43) Clegg, S. L.; Brimblecombe, P.; Wexler, A. S. Thermodynamic Model of the System H^+–NH_4^+–SO_4^{2-}–NO_3^-–H_2O at Tropospheric Temperatures. *J. Phys. Chem. A* **1998**, *102* (12), 2137–2154.

(44) Von Glasow, R.; Sander, R. Variation of Sea Salt Aerosol pH with Relative Humidity. *Geophys. Res. Lett.* **2001**, *28* (2), 247–250.

(45) Pinterich, T.; Spielman, S. R.; Wang, Y.; Hering, S. V; Wang, J. A Humidity-Controlled Fast Integrated Mobility Spectrometer (HFIMS) for Rapid Measurements of Particle Hygroscopic Growth. *Atmos. Meas. Tech* **2017**, *10*, 4915–4925.

(46) Harris, E.; Sinha, B.; Foley, S.; Crowley, J. N.; Borrmann, S.; Hoppe, P. Sulfur Isotope Fractionation during Heterogeneous Oxidation of SO2 on Mineral Dust. *Atmos. Chem. Phys* **2012**, *12*, 4867–4884.

(47) Hoppel, W.; Pasternack, L.; Caffrey, P.; Frick, G.; Fitzgerald, J.; Hegg, D.; Gao, S.; Ambrusko, J.; Albrechcinski, T. Sulfur Dioxide Uptake and Oxidation in Sea-Salt Aerosol. *J. Geophys. Res. Atmos.* **2001**, *106* (D21), 27575–27585.

(48) Cochran, R. E.; Jayarathne, T.; Stone, E. A.; Grassian, V. H. Selectivity across the Interface: A Test of Surface Activity in the Composition of Organic-Enriched Aerosols from Bubble Bursting. *J. Phys. Chem. Lett.* **2016**, *7* (9), 1692–1696.

(49) Zhang, T.; Brantley, S. L.; Verreault, D.; Dhankani, R.; Corcelli, S. A.; Allen, H. C. Effect of pH and Salt on Surface PKa of Phosphatidic Acid Monolayers. *Langmuir* **2018**, *34* (1),

530–539.

(50) Zhang, T.; Cathcart, M. G.; Vidalis, A. S.; Allen, H. C. Cation Effects on Phosphatidic Acid Monolayers at Various pH Conditions. *Chem. Phys. Lipids* **2016**, *200*, 24–31.

(51) Turšič, J.; Grgić, I.; Podkrajšek, B. Influence of Ionic Strength on Aqueous Oxidation of SO_2 Catalyzed by Manganese. *Atmos. Environ.* **2003**, *37* (19), 2589–2595.

(52) Clegg, S. L.; Pitzer, K. S.; Brimblecombe, P. Thermodynamics of Multicomponent, Miscible, Ionic Solutions. 2. Mixtures Including Unsymmetrical Electrolytes. *J. Phys. Chem.* **1992**, *96* (23), 9470–9479.

(53) Wexler, A. S.; Clegg, S. L. Atmospheric Aerosol Models for Systems Including the Ions H^+, NH_4^+, Na^+, SO_4^{2-}, NO_3^-, Cl^-, Br^-, and H_2O. *J. Geophys. Res. Atmos.* **2002**, *107* (14), ACH 14-1.

(54) Chen, Y.; Xu, L.; Humphry, T.; Hettiyadura, A. P. S.; Ovadnevaite, J.; Huang, S.; Poulain, L.; Schroder, J. C.; Campuzano-Jost, P.; Jimenez, J. L.; Herrmann, H.; O'dowd, C.; Stone, E. A.; Ng, N. L. Response of the Aerodyne Aerosol Mass Spectrometer to Inorganic Sulfates and Organosulfur Compounds: Applications in Field and Laboratory Measurements. *Environ. Sci. Technol* **2019**, *53* (9), 5176–5186.

(55) De Leeuw, G.; Andreas, E. L.; Anguelova, M. D.; Fairall, C. W.; Lewis, E. R.; O'Dowd, C.; Schulz, M.; Schwartz, S. E. Production Flux of Sea Spray Aerosol. *Rev. Geophys.* **2011**, *49* (2).

CHAPTER 4 ENHANCED RATES OF TRANSITION METAL ION CATALYZED OXIDATION OF S(IV) IN AQUEOUS AEROSOLS: INSIGHTS INTO SULFATE AEROSOL FORMATION IN THE ATMOSPHERE

4.1 Abstract

The oxidation of S(IV) is a critical step in the fate of sulfur dioxide emissions that determines the amount of sulfate aerosol in the atmosphere. Herein, we measured accelerated S(IV) oxidation rates in micron-sized aqueous aerosols compared to bulk solutions. We have investigated both buffered and unbuffered systems across a range of pH values in the presence of atmospherically relevant transition metal ions and salts and consistently found the oxidation rate to be accelerated by ca. 1-2 orders of magnitude in the aerosol. This enhancement is greater than can be explained by enrichment of species in the aerosol compared to the bulk and indicates that surface effects and potentially aerosol pH gradients play important roles in the S(IV) oxidation process in the aqueous aerosol. In addition, our experiments were performed with dissolved S(IV) ions (SO_3^{2-}/HSO_3^-), allowing us to demonstrate that acceleration occurs in the condensed phase showing that enhanced sulfate formation is not exclusively due to gas-aerosol partitioning or interfacial SO_2 oxidation. Our findings are an important step forward in understanding larger than expected sulfate concentrations observed in the atmosphere and show that inorganic oxidation processes can be accelerated in micron-sized aqueous droplets compared to bulk solution.

4.2 Introduction

The oxidation of S(IV) is a key reaction in atmospheric chemistry. Sulfur dioxide (SO_2) is emitted from individual sources at rates as large as 4000 kilotons per year.[1] The continental background concentration of SO_2 is up to 1 part per billion (ppb) and polluted regions can have levels of several hundred ppb.[2] In the atmosphere, SO_2 dissolves into aqueous systems including aerosols and cloud droplets to form one of several aqueous S(IV) species, including bisulfite

(HSO_3^-), sulfite (SO_3^{2-}), and metabisulfite ($S_2O_5^{2-}$), which hereafter will be collectively termed $S(IV)_{aq}$. These species are oxidized by a variety of pathways into sulfate (SO_4^{2-}). For example, for bisulfite, the oxidation reaction with oxygen can be written as:

$$HSO_3^- + \frac{1}{2}O_2 \rightarrow SO_4^{2-} + H^+ \quad (4.1)$$

This reaction can impact the composition and acidity of atmospheric aerosols. Although the oxidation of S(IV) is relatively slow, this is critically important to environmental chemistry, as the pH of aerosols and cloud droplets influences the rate of acid-catalyzed chemical transformations, the impact of aerosols on human health, and even the ability of aerosols to act as cloud condensation nuclei.[3–5]

The oxidation of $S(IV)_{aq}$ is overall quite complex and notoriously sensitive to reaction conditions. In addition, recent measurements have shown more formation of sulfate during severe pollution events than can be accounted for by current models.[6,7] The process is highly pH-dependent, with different rate laws and mechanisms operative for different pH regimes (acidic, neutral and basic).[8] The reaction is also inhibited by many different chemical species, including organic compounds, ammonia, and even S(IV) itself.[9,10] These all vary with ionic strength, μ, and depending on the exact conditions, higher μ can either accelerate or inhibit the reaction kinetics.[10–12] Furthermore, the reaction can be catalyzed by transition metal ions (TMIs).[10,13] TMI-catalyzed oxidation can, under some circumstances, be the dominant pathway of sulfate formation in the atmosphere.[14] Indeed, one study found the reaction is seven times faster in distilled water versus milli-Q water due to the presence of TMIs in distilled water, despite the fact that these are present in sub-micromolar concentrations.[15]

Since the reaction rate depends on the exact nature of the solution matrix, and more sulfate is being observed in haze events than can be explained by current kinetics data, the current study

focuses on high ionic strengths (μ > 2 M) found in aerosols to help fulfil the need for solute strength-dependent kinetics in this regime.[12,16,17] We also worked in the 0.1-1.5 m $S(IV)_{aq}$ range since the majority of studies on S(IV) oxidation have utilized concentrations on the order of 0.01 m or less (note: "m" refers to molality throughout this report).[10,18,19] Even higher concentrations are not practical since the saturation concentration of Na_2SO_3 is 2.1 M.[20] We employed an Aerosol Optical Tweezers (AOT) to suspend individual droplets in surface-free environments and continuously monitor their composition, size, and refractive index via Raman spectroscopy and Whispering Gallery Modes (WGMs).[21] We used confocal Raman spectroscopy to monitor the same systems in the bulk phase. This allowed us to use our single-aerosol measurements to determine the extent to which oxidation of $S(IV)_{aq}$ catalyzed by transition metal ions and common salts is accelerated in aerosols as well as the pH dependence of this process.

4.3 Methods

All solutions were prepared using milliQ water with a resistivity > 18.1 MΩ. Sodium chloride (Fisher Lot 188772 and 186819) and sodium sulfate (Fisher Lot 161950) were baked at 200 °C for at least 48 hours to remove organic impurities. Buffers were prepared from sodium acetate (Macron Batch 0000227236), imidazole (Sigma-Aldrich Lot WXBC9930V), glacial acetic acid (Fisher Lot 200447) and 1 and 6 N HCl (Fisher Lot 195295 and 183144). The pH of solutions was measured with a pH meter (OAKTON Instruments) and ranged from pH 5.4 to 9.4 ± 0.3 for unbuffered experiments and was either 7.0 or 3.8 ± 0.1 for buffered experiments. For experiments with added Fe and Mn, $FeCl_3 \cdot 6H_2O$ (Aldrich Lot MKBC9551V) and $MnCl_2 \cdot 4H_2O$ (Fisher Lot 162637) were used, respectively. Various sources of S(IV), including $NaHSO_3^-$ (bisulfite), $Na_2S_2O_5$ (metabisulfite), and Na_2SO_3 (sulfite) were used to verify that aerosol phase acceleration was not unique to one lot number. Additional reagents included sodium nitrate (Sigma-Aldrich

Lot MKBW8240V) and sodium perchlorate (Sigma-Aldrich 0401080). Except where otherwise noted, salts were used to adjust the ionic strength to 2.45 m.

For bulk experiments, a confocal Raman spectrometer (Horiba) was used with the LabSpec 8 software suite. Solutions were prepared by first weighing the S(IV) source and any salts such as NaCl into a scintillation vial, then adding milliQ water and acid or buffer as needed to obtain the appropriate pH. Solutions were agitated vigorously to quickly dissolve the solids, and this likely resulted in solutions with dissolved O_2 at saturation for the given temperature (23.5 ± 0.5 °C) and ionic strength. 5 mL of solution was pipetted into a glass petri dish, and Kimwipe (Kimberly-Clark) fibers were gently dusted onto the surface of the solution to aid in laser focusing. Spectra were obtained with 10 second acquisition times and 5 accumulations, typically every 3 minutes for an average of 67 minutes total, using 1800 grooves/millimeter for optimal resolution. For reaction times greater than an hour, the laser occasionally was refocused on the solution surface due to water evaporation. For experiments with sodium nitrate, the nitrate peak was used as an internal standard to track the relative intensity of the spectra over time. By focusing the laser slightly past the surface, the intensity of the signal remains relatively constant for over an hour as the evaporation causes the laser focus to pass through the optimal position and then signal begins to decrease with further evaporation.

For experiments in the aerosol phase, a commercial Aerosol Optical Tweezers 100 (Biral Inc.) was used. Solutions were prepared the same as for the bulk and then aerosolized by an ultrasonic nebulizer (MicroAIR U22, OMRON) resulting in aerosols 3 ± 1 microns in radius. The aerosols were trapped by a laser (532 nm, 50 mW power). Except where stated otherwise, the RH was maintained at 90 ± 8% by controlled flow of wet and dry nitrogen gas (total flow 30 sccm). The amount of O_2 present in the chamber was less than ambient conditions due to the N_2 flow.

Raman spectra were acquired every second at 1200 g/millimeter and averaged in sets of eleven for analysis. Temperature probe readings were 24.6 ± 0.1 °C, and additional heating of the aerosol by the laser is expected to be on the order of 100 mK.[22] The Raman spectrometer wavenumbers were calibrated using standard emission lines from a Hg and Ne/Ar USB light source (Princeton Instruments). Average experiments included 12 minutes of S(IV) containing aerosol data, followed by external standard(s). Calibration of intensity was performed by trapping a ca. 1 m sodium sulfate and/or nitrate aerosol for the acquisition of at least 100 spectra at the end of every experiment and quantifying the aerosol-phase concentration by obtaining refractive index. This allowed determination of the concentration of sulfate in other samples from that experiment via comparison of the integrated area of the sulfate peak (982 cm^{-1}) or nitrate peak (1049 cm^{-1}).

Details of other measurements are given in the SI of the publication associated with this chapter (see Appendix). Briefly, TMI concentrations were quantified using a Thermo Fisher iCAP RQ ICP-MS analyzer. Bulk-phase refractive index measurements were performed using an ABBE-3L refractometer (Bausch & Lomb). Finally, enrichment factors (EFs) were measured by AOT, conductivity probe, and ICP-MS methods.

4.4 Results and Analysis

4.4.1 Spectral Evidence of Acceleration

Representative Raman spectra of the oxidation reaction at acidic pH are given in Figure 4.1. The sulfate band is located at 982 cm^{-1} and has the same location within spectral resolution for both phases. In addition, HSO_3^- and $S_2O_5^{2-}$ peaks are present at higher wavenumbers, 1025 and 1052 cm^{-1}. At high pH (≥7) for bulk spectra there are broad, overlapping SO_3^{2-} bands at 953 and 967 cm^{-1}. By contrast, for aerosol-phase spectra at all pH values, the S(IV) bands have low intensity. This is consistent with our previous work with the SO_4^{2-}/HSO_4^- system, where the latter

had substantially lower intensity relative to sulfate in the aerosol compared to the bulk.[23] The S(IV) bands do appear when sufficient S(IV) is dissolved in the bulk solution and aerosols with high S(IV) concentrations generated from these solutions are trapped.

Figure 4.1 also shows that sulfate peaks are present in the AOT spectra as soon as the micron-sized aerosol is trapped in the optical tweezer and grow in intensity faster than that seen in

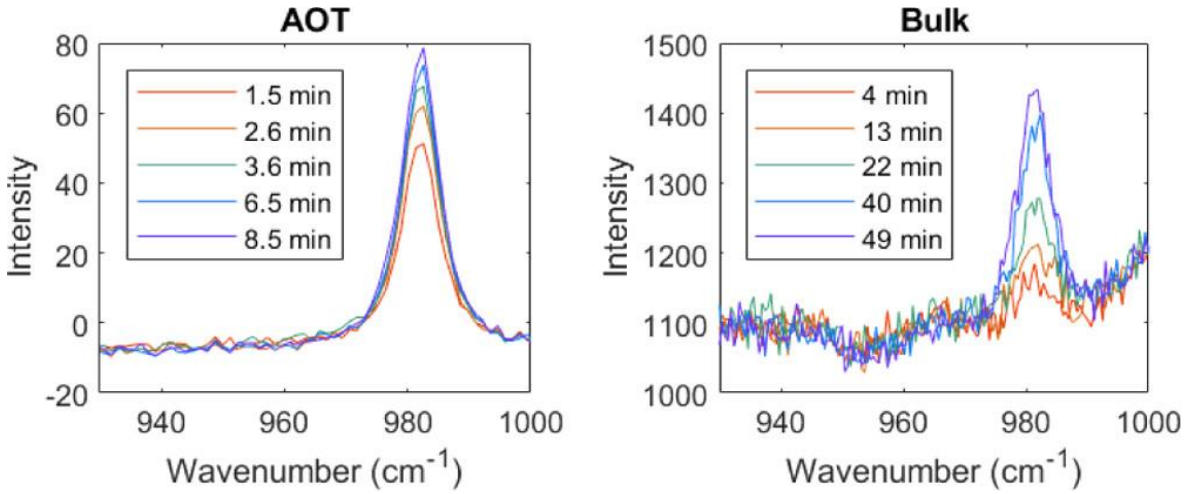

Figure 4.1: Representative sulfate ion spectra as a function of time. Each trace shows Raman spectra following the formation of sulfate in aerosol and bulk phases at pH 5.6. The solutions contained 1.0 m S(IV) and 0.2 m $NaNO_3$. The aerosol was 4.0 μm in radius, and the bulk solution was 5 mL in a glass Petri dish (d = 55 mm) exposed to ambient O_2.

the bulk phase spectra. The aerosol is prepared by nebulization of a bulk solution and is trapped within five minutes of beginning the experiment. Fewer than 30 seconds pass between aerosol trapping and spectral acquisition. It is clear that some of this sulfate formation is occurring during the trapping process. The rate of sulfate formation is then determined using only data after the aerosol is stabilized in the AOT. For example, for the AOT data shown in Figure 4.1, the first data point used in computing rate is obtained from the first spectrum, *not* from [sulfate] = 0. Likewise, for calculating bulk phase rates, the first data point used is obtained from the first spectrum where sulfate peak area can be calculated by Gaussian curve fitting. The advantage of this method is that

it makes the results less sensitive to any sulfate already present in the S(IV) source and it excludes interference from an induction period.[10,24,25]

4.4.2 Quantifying Apparent Acceleration Factors for Various Conditions

For both bulk and aerosol spectra, sulfate concentrations were calculated using calibration curves. We found that sulfate formation is significantly faster in the aerosol phase than the bulk. To quantify this acceleration, we defined an Apparent Acceleration Factor (AAF) as given in Equation 4.2:

$$AAF = \frac{r_a}{r_b} \tag{4.2}$$

Here, r_a and r_b are the rates (in m/min) observed in the aerosol and bulk phases, respectively, where sulfate formation was linear with time. The data included in our rates began with the first spectrum containing a stable, quantifiable sulfate peak and ended after sufficient data was obtained. Representative linear fits are given in Figure 4.2.

A summary of AAFs for different experimental conditions is given in Table 4.1.

Table 4.1: Summary of AAFs for S(IV) oxidation in the aerosol versus bulk phase under different pH conditions.

pH conditions	Number of data sets	[S(IV)] (m)	Avg AAF	AAF range	AAFE range
Acidic unbuffered	18	1.0	19	4-45	7-57
Neutral unbuffered	5	1.0	33	10-55	12-96
Basic unbuffered	10	1.0	41	15-92	21-153
pH 3.8 acetate buffer	4	0.5-1.4	55	41-78	48-89
pH 7.0 imidazole buffer	10	0.2-0.4	33	14-76	16-163

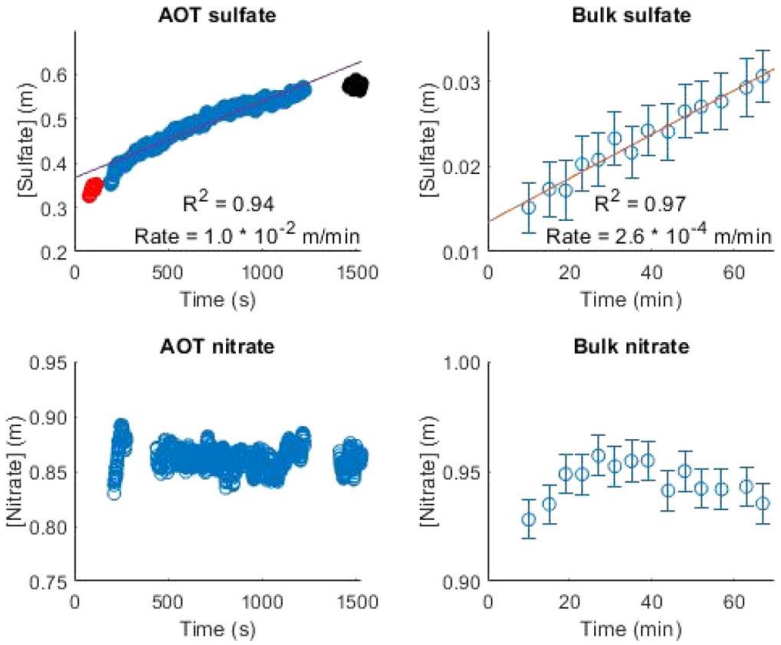

Figure 4.2: Sample sulfate formation data for the aerosol and bulk phases. The data are from pH 9.4 samples with 1 m Na2SO3 and 0.95 m NaNO3 as the internal standard. AOT data show consecutive averages of 11 spectra (e.g., circles show spectra 1−11, 2−12, 3−13, etc.). Gaps in AOT data correspond to interference from WGMs. The aerosol data was collected for longer than a typical experiment to demonstrate the extent of linearity of sulfate formation, and initial data corresponding to aerosol stabilization (red circles) as well as data departing from linearity (black circles) are not included in rate computation. AOT data error bars are not shown for clarity and are ca. ± 0.02 m. Bulk error bars show the error in the sulfate or nitrate band area from peak fitting.

Here, a "data set" is the result from one bulk phase experiment compared to the average of multiple aerosol phase experiments with all parameters held constant. We tested a wide variety of pH conditions to determine the impact of this parameter on the AAF, with particular emphasis on acidic conditions since the majority of atmospheric aerosols are acidic.[3,26] Even for unbuffered experiments, changes in pH during the reaction are expected to be small (< 0.1 pH unit) since the large concentrations of SO_3^{2-} would absorb the majority of protons produced from the oxidation.[27] Ionic strength was controlled using either NaCl or $NaNO_3$, two relevant salts for atmospheric aerosols.[3,12,16] AAFs show the reaction is at least an order of magnitude faster in the aerosol phase. Additionally, we computed an Apparent Acceleration Factor corrected for Enrichment (AAFE) to account for the increased ionic strength and reagent concentrations in the aerosol. In all cases, AAFEs are larger than AAFs by 19 to 477 percent.

For our systems, since we worked at high concentrations of S(IV) and salts, there was sufficient TMI present to catalyze the oxidation as the salt samples contained non-negligible concentrations of TMI. In order to quantify TMI concentrations, Inductively Coupled Plasma Mass Spectrometry (ICP-MS) was employed to measure iron, manganese, copper, and cobalt amounts in our samples. To further probe the nature of TMI catalysis, we performed experiments with explicitly added Fe^{3+} or Mn^{2+} (Figure 4.6). In both cases, S(IV) oxidation remained faster in the aerosol phase than the bulk across the pH range we studied (5.4 to 9.3). It is noteworthy that iron speciation changes considerably over this range, and therefore our results show that S(IV) oxidation acceleration occurs with different TMI species present.[28,29] Table 4.1 also shows that AAFs generally increase with pH for unbuffered systems.

For buffered experiments, pH was maintained constant at either 3.8 or 7.0 with an acetate or imidazole buffer, respectively, and $[S(IV)]_{aq}$ was varied. For the imidazole systems, AAFs went

through a maximum at ca. 0.3 m S(IV). At relatively high S(IV) concentrations (0.4 m), additional S(IV) increases the rate to a lesser extent due to self-inhibition. For the acetate systems, it was necessary to work at higher concentrations so the sulfate Raman band could be used to obtain multiple data points before acetic acid evaporation from the aerosol compromised the buffer pH. At these concentrations, any trend between AAF and [S(IV)] is less obvious. This may also be due to the complexity of the factors involved, namely, acid catalysis and inhibition by acetate.[9,30] Even so, consistent acceleration in the aerosol versus the bulk is observed over a wide range of conditions.

4.4.3 Measurement of Aerosol-Phase Concentrations

Aerosol concentrations were measured by using the refractive index (n) of optically trapped aerosols to calculate their total solute content as has been previously demonstrated.[31] From the position and spacing of WGMs (Figure 4.3), n can be precisely obtained.[21] This enables calculation of molal refractivity (R), and hence mole fraction of solute x as shown in Equations 4.3-4.5

$$R = R_w + x(R_s - R_w) \tag{4.3}$$

$$R = \frac{n^2 - 1}{n^2 + 2} * x\left(M_w + (M_s - M_w)\right) * \frac{1}{d} \tag{4.4}$$

$$d = d_0 + \sum_i A_i * x^i \tag{4.5}$$

Here, R_w, R_s, M_w, and M_s are the refractivities and molar masses of water and the average solute, respectively, d is the density of the solution, d_0 is the density of pure water and A_i are density polynomial coefficients. Refractivities were determined using a refractometer and A_i values were taken from literature.[32,33] When the solute is a salt, the M_s is the weighted average molar mass of its ions. When Eqn. 4.3 and 4.4 are set equal to solve for x, an algebraic solution does not exist. Thus, calculations were performed by checking every possible x in small increments across a

physically realistic range and keeping the solution with the least difference between Equations 4.3 and 4.4.

For a given *n*, there is one possible *x*, allowing calculation of aerosol-phase concentration for systems containing one binary salt. When multiple salts are present, however, these equations do not have a single solution since the enrichments of the salts may be different and hence the salts may be present in different ratios in the aerosol than as prepared in the bulk. Therefore,

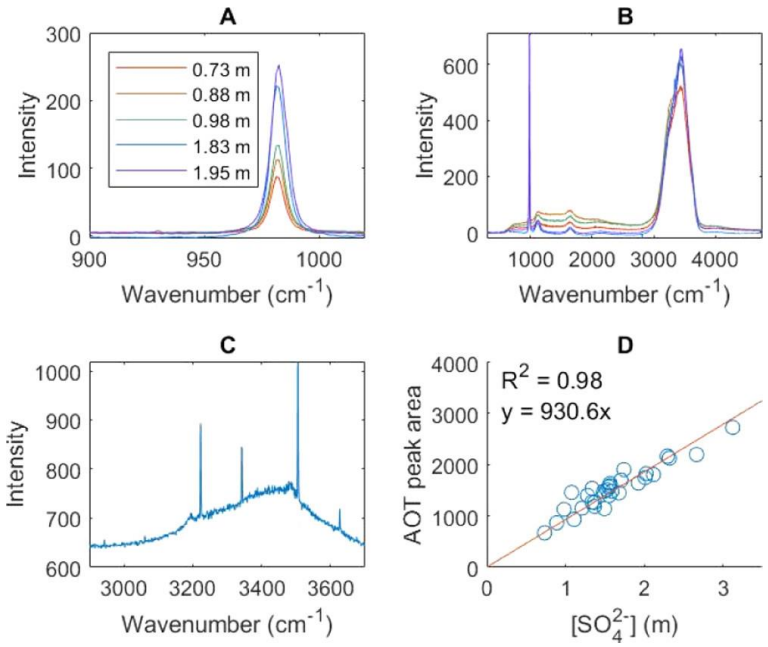

Figure 4.3: (A) sample Na_2SO_4 AOT spectra taken at 1200 grooves/mm in the sulfate region showing the concentration-dependence of the prominent sulfate peak at 982 cm^{-1}; (B) same aerosols as "A" taken at 300 grooves/mm to show the entire spectral range (A,B both show averages of 11 spectra, so WGMs are not visible); (C) single spectrum taken at 1200 grooves/millimeter in the water O–H stretching region showing the WGMs, used to calculate aerosol size and refractive index, that appear on the broader water peak; and (D) calibration curve relating Raman peak area to sulfate ion concentration calculated by refractive index. The fit line has a set intercept of (0, 0).

independent measurements of the concentrations of all but one salt are necessary to uniquely determine the concentration of all species in the aerosol phase. For our work, we used NaCl, Na_2SO_4, and $NaNO_3$, the latter two of which have distinct Raman bands allowing concentration to be determined via calibration curves. From aerosol concentration, an enrichment factor (EF) can

be calculated, which here we simply define as the aerosol-phase concentration of a species divided by the concentration in the bulk from which the aerosol was generated. EFs were also calculated by ICP-MS and conductivity experiments.

4.4.4 Impact of Ionic Strength

Both NaCl and $NaNO_3$ were found to be enriched into the aerosol phase, so it is important to account for the impact this has on the oxidation rate. To this end, we performed several series of bulk phase experiments where salt concentration could be precisely controlled, and the results are given in Figure 4.4. It is clear that increasing [NaCl] or [$NaNO_3$] would not increase the oxidation rate, and in fact their enrichment actually slows the oxidation down. The difference in intercepts for the linear fits is not a concern, since the NaCl experiments used 0.2 m $NaNO_3$ as an internal standard while the $NaNO_3$ experiments used no NaCl. The experiments with NaCl and $NaNO_3$ were also performed in the aerosol phase and indicate the same trend. To determine if this effect was simply due to increased ionic strength, we also tested the impact of sodium perchlorate ($NaClO_4$) on the rate, as this ion is generally considered inert toward these type of reactions.[34] Figure 4.4c shows that $NaClO_4$ has the most negative impact on the rate out of the three salts, with a less linear relationship. Taking the same data and plotting the log of the rate versus an ionic strength parameter defined as $\mu^{1/2}/(1+ \mu^{1/2})$, a more linear result is obtained in Figure 4.4d; this is consistent with previous work on the impact of ionic strength on aqueous TMI-catalyzed S(IV) oxidation.[30]

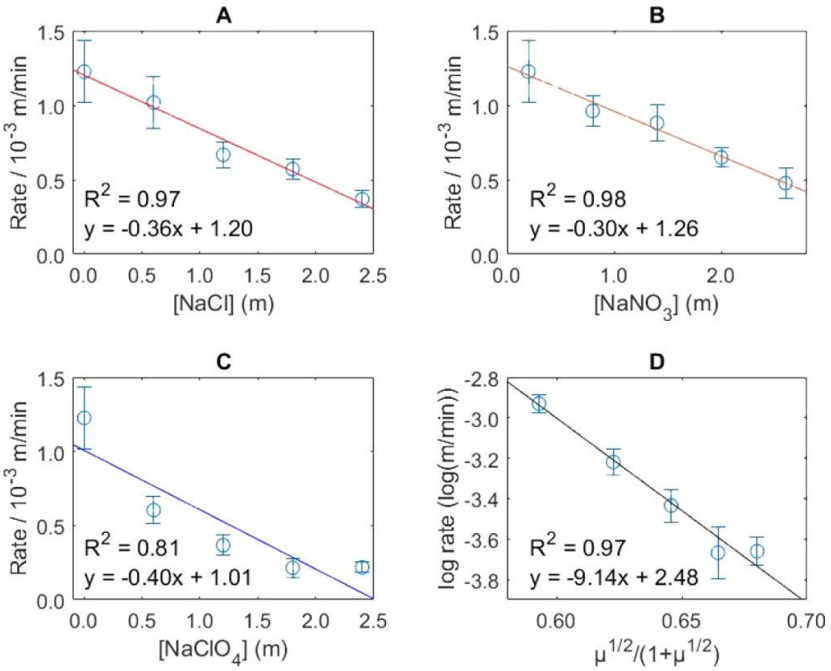

Figure 4.4: Impact of various anions on sulfur oxidation rates in bulk aqueous solutions of (A) [NaCl]; (B) [$NaNO_3$]; and (C,D) [$NaClO_4$]. All solutions were prepared at pH 5.6. Solutions were composed of 1 m S(IV), the salt indicated by the x-axis, and for all data except (B), 0.2 m $NaNO_3$ was used as an internal standard. (C,D) reflect the same data plotted differently. Error bars show 95% confidence intervals from linear regression of [SO_4^{2-}] vs time.

4.4.5 Enrichment

Recent studies have shown the acceleration of reactions in aerosols. This has been the subject of a great deal of interest.[35,36] For reasons that remain not fully understood, the environment of picoliter droplets greatly enhances the kinetics of many chemical transformations.[37] Clarke and Radojevic showed that S(IV) oxidation could be substantially faster in sea spray aerosols than seawater due to catalysis by ions such as Cl^-, although whether this was attributable to the aerosol environment was unclear since the concentrations of Cl^- and H^+ were orders of magnitude larger in their aerosols compared to the bulk.[38] Liu *et al.* used an aerosol flow tube reactor to find that deliquesced, submicron aerosol droplets enhance the rate of S(IV) oxidation by hydrogen peroxide (and by TMIs at pH 2.8, although this effect is inhibited by increasing ionic strength).[30] Zhang *et*

al. measured SO_2 oxidation by Mn^{2+} and Fe^{3+} using a smog chamber and calculated the reaction to be two orders of magnitude faster for oxidation by Mn^{2+} assuming the rate law is the same in the bulk and aerosol phases.[11] The studies by both Liu *et al.* and Zhang *et al.* were performed under conditions using SO_2 as the S(IV) source, so it is unknown whether the accelerated reaction is $S(IV)_{aq}$ oxidation, interfacial SO_2 (g) oxidation, or both. Indeed, experiments with SO_2 (g) are complicated by the solubility of the gas into aerosols, which depends on pH and μ. Therefore, here we used aqueous S(IV) sources at higher pH levels where formation of SO_2 does not occur and $S(IV)_{aq}$ oxidation can be isolated. There is also a recent report by Wang *et al.* demonstrating aerosol phase acceleration for the Mn-catalyzed pathway via chamber studies up to pH 7.[39] We hope to contribute further to understanding of S(IV) reaction acceleration by studying the reaction on a single aerosol particle basis.

Although aerosol-phase acceleration is more easily explained for highly charged droplets created from electrospray ionization, acceleration has been shown for uncharged aqueous droplets as well.[36] We note that differences in rates between the bulk phase and the aerosol observed here are not due to diffusion limitations in the bulk and therefore other mechanisms are needed to explain accelerated sulfate formation. As discussed in more detail, three relevant factors are considered. The first is enrichment of species from the bulk to the aerosol phase. This is quantified by EFs. Second, we will consider the implications of the fact that molecules in the aerosol phase have more access to the surface relative to bulk phase. Third, we will discuss the impact of pH on the oxidation rate. Finally, we briefly describe how the approach used here for these types of reaction acceleration studies is consistent with some recent recommendations.[40]

The increase in oxidation rate could theoretically be due to increased concentrations in the aerosol phase. First, we consider this possibility for the NaCl and $NaNO_3$ salts we used. The

implication of Figure 4.4 is that the inhibiting effect of increasing [NaCl] or [$NaNO_3$] is mainly inhibiting due to increasing μ, but slightly less inhibiting than a totally inert ion due to the weakly catalyzing nature of NaCl and $NaNO_3$. This can be seen by comparing the slopes of Figure 4.4a and 4.4b to Figure 4.4c. However, the overall effect for both ions is still inhibiting, and therefore enrichment of these ions into the aerosol phase would not accelerate the reaction. We performed a similar analysis on the enrichment of S(IV) and TMI's and found that, combined, their enrichment would not even double the reaction rate, far below what is found in Table 4.1. Therefore, other factors must be the main cause of acceleration.

4.4.6 Surface Access

In droplets, molecules have greater access to the interface than in bulk solutions. This is quantified by two characteristic lengths. The first is the length of the compartment in which the molecules are confined, L_{com}, and the second is the average distance a molecule travels before reacting, L_{rxn}.[41]

$$L_{rxn} = \sqrt{D * t} \tag{4.6}$$

Here, *D* is the diffusion coefficient and *t* is the chemical lifetime (the product of the concentration and the inverse of the rate). Using representative values for our system and the diffusion coefficient of sulfite,[42] we found L_{rxn} and L_{com} to be 600 and 8 μm, respectively, for aerosols and 6,200 and 55,000 μm for the bulk. This indicates that molecular species present in the aerosols sample the surface several times before reacting, while in the bulk phase they do not. For this reaction, surface access could accelerate the oxidation process by increasing interaction with ambient O_2 diffusing at the air/water interface. Since the reaction steps proceed at different rates depending on the form of S(IV), surface access could also enhance the process by altering S(IV) speciation.[43] It has been shown that molecules can have distinct surface and bulk pK_a values, so it is reasonable to infer

that various S(IV) equilibria can be different at the interface.[27,44] Generally, the more highly charged an ion is, the greater the energy cost to move it to the air-water interface.[45] For our systems, this indicates that $SO_3^{\bullet-}$ is more likely to be at the surface than SO_4^{2-}. Given that $SO_3^{\bullet-}$ needs to react with O_2 for the oxidation to proceed while sulfate is an inhibitor of S(IV) oxidation, this relative surface propensity of the radical anion creates more favorable reaction conditions at the surface compared to the bulk.[9] Additionally, it has been noted that TMIs themselves can be oxidized or undergo complexation during the S(IV) oxidation process, which would slow down sulfate formation.[19] Since Fe^{3+} and Mn^{2+} are more highly charged than the radicals that propagate the reaction, it is possible that TMIs initiate the process from the core of the aerosol and then an accelerated propagation happens with radicals and O_2 at the aerosol surface. However, the authors emphasize that the complexity of urban aerosols, including very high ionic strengths (> 10 M) and the presence of inhibiting organics may create conditions favoring a different mechanism in the real world.

Another key aspect of surface access is interaction with spontaneously generated hydrogen peroxide. Lee *et al*. showed that supermicron pure water droplets generated ca. 30 μM H_2O_2 without application of an external catalyst or voltage, which they attribute to OH radical action at the interface.[46] Since H_2O_2 is a powerful oxidizer of the S(IV) reaction, even these low concentrations could contribute toward reaction acceleration, especially over timescales of minutes if H_2O_2 is continuously generated. Using H_2O_2 production data from Lee *et al*.,[46] literature S(IV) oxidation rate data at our ionic strength, [47] and assuming the rate law from dilute solutions holds for concentrated S(IV) samples, an oxidation rate of 0.043 m/min could be obtained. Further, the production of H_2O_2 at the interface could be enhanced by the presence of radical intermediates involved in S(IV) oxidation, and the hypothesis that the OH radical plays a role in this H_2O_2

generation is consistent with our observation that AAFs are higher at higher pH since it is proposed that OH radicals can be generated from hydroxide ions.[46]

4.4.7 Aerosol pH

We confirmed the pH of the generated aerosols utilizing substrate deposition onto pH paper as described in previous studies (Figure 4.7),[26,48,49] however, the individual environments within these aerosols may be varied. Indeed, it is possible that a pH gradient exists inside aerosols, creating droplets with more basic cores and more acidic surfaces.[50] Although gradients as large as 3.6 pH units have been reported, given how sensitive the reaction is to changes in pH, even a gradient of less than 1 pH unit could explain aerosol-phase acceleration for $S(IV)_{aq}$ oxidation.[10,50] This is partly due to the greatly enhanced reactivity of $Fe(H_2O)_5(OH)^{2+}$ compared to $Fe(H_2O)_6{}^{+3}$, key complexes for the iron-catalyzed reaction, with the former more present at higher pH.[44] Thus, if a gradient does exist in aerosols, then aerosols are ideal reactors for S(IV) oxidation, since the process at interfaces is faster at low pH, while the process in the bulk is potentially faster at high pH (although conflicting kinetic orders for H^+ at pH above 4 have been reported).[9–11,51]

The existence of an aerosol pH gradient is still under debate,[50,52] but it is worth noting that the investigators who proposed it were working with alkaline aerosols, and here we observe larger AAFs for more basic droplets. It is possible that the gradient is an absolute proton concentration difference between the droplet core and surface. In that case, since pH is a logarithmic scale, the pH gradient would be larger at lower proton concentrations. If protons have an inherent surface propensity, then at lower concentrations a greater fraction of the protons would be able to

accumulate at the surface.[41,53] A visual representation for our hypotheses for aerosol-phase acceleration is given in Figure 4.5.

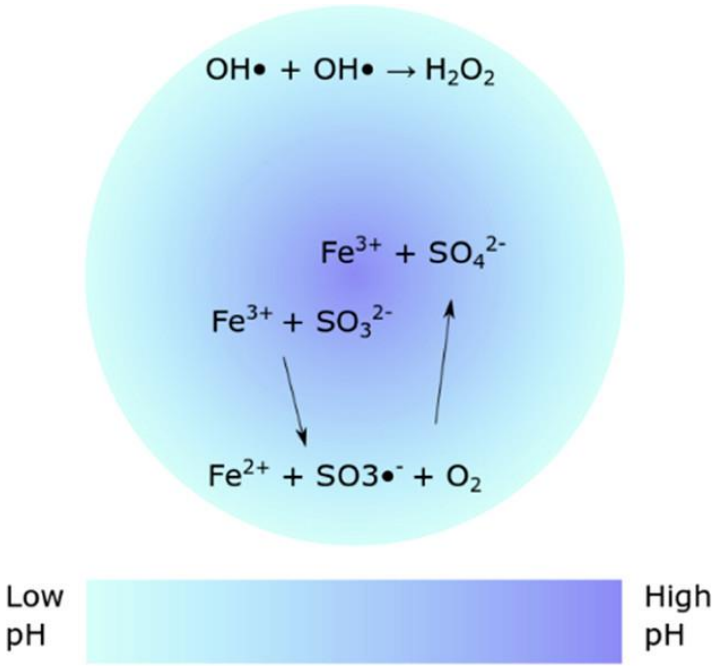

Figure 4.5: Visual representation of the various factors that contribute to aerosol-phase reaction acceleration. H_2O_2 generation is enhanced at the interface. A pH gradient creates a more acidic surface and more basic core, which favors faster reaction conditions (for example, the reaction at the bottom of the aerosol requires a proton to proceed). Highly charged TMIs and inhibiting products are spatially co-located in the aerosol core while lower charged TMIs, radicals and O_2 concentrate and react at the interface. Detailed mechanistic steps are omitted from this conceptual image.

4.4.8 Control of Experimental Variables

There are several precautions that should be taken in reporting droplet-phase reaction acceleration. A recent report by Rovelli *et al*. provided six recommendation for such studies.[40] Our work was consistent with these recommendations as follows. We controlled solvent evaporation by maintaining the relative humidity (RH) in the AOT. Our droplet sizes and reagent concentrations were precisely known by radius and refractive index data derived from the spectral WGMs (which allowed us to determine when enrichment occurred, see Figure 4.8). We performed

experiments on varying concentrations within the range of instrumental detection. The reaction timescale was controlled because the reaction was slow enough that nebulization time was negligible. Online detection of products was obtained by collecting Raman spectra every second. Finally, by working at high pH and not using ionizing nebulizers, we avoided competing gas phase SO_2 reactions. Therefore, while our experimental design does require use of relatively high reagent concentrations, we are able to effectively measure acceleration by obtaining kinetics data for individual droplets in well-controlled environments and circumvent several complications that are more common in electrospray experiments. De Haan *et al.* has shown kinetic enhancement in uncharged drying droplets, and most other studies of reaction acceleration use charged droplets.[35,54] Our results are thus unique in that they demonstrate aerosol-phase rate enhancement in single uncharged droplets maintained at constant, high RH where concentration of reagents over time does not contribute to reaction acceleration.

4.4.9 Atmospheric Implications

S(IV) oxidation has become a topic of renewed interest due to observations of severe haze events that cannot be explained based on current knowledge from bulk phase kinetics parameters.[6,7] Laboratory experiments to explain these field observations are now being reported in the literature. For example, Zhang *et al.* performed smog chamber studies and found that SO_2 oxidation is 2 orders of magnitude faster in aerosol water than the bulk,[11] which is in agreement with the AAFs we report here. Their studies were performed at lower pH values than we used (0.4 to 5.0), using much higher TMI concentrations and ppb level SO_2 concentrations. Therefore, their data reflects a combination of both the interface-driven oxidation of SO_2, which is highly efficient at low pH, and the aqueous phase process.[51] Our data thus confirms that droplet-phase acceleration

occurs for the aqueous phase process in the absence of SO_2 even at high S(IV) concentrations and at the low TMI concentrations found in the atmosphere.

Furthermore, while most previous studies have been performed at low pH, our data for alkaline and neutral droplets shows that accelerated S(IV) oxidation is expected for higher pH aerosols found in some portions of the world.[3,24] By demonstrating that our AAFs exceed what can be obtained from aerosol-phase enrichment alone, we have shown that distinct surface-driven mechanisms may dominate in aerosols and control of surface area to volume ratios is essential in investigating the kinetics of this process. On a more fundamental level, our results show that inorganic oxidation processes can be accelerated in uncharged aerosols. This complements the many recent findings of organic accelerated reactions measured in electrospray experiments and encourages the use of aerosols in green synthesis and industrial catalysis.

We have shown that TMI-catalyzed S(IV) oxidation is significantly accelerated in the aerosol phase. This is a key step forward in understanding the process of atmospheric S(IV) oxidation, as we have decoupled the interfacial and aqueous reactions and definitively shown the latter to be enhanced in the aerosol phase beyond what can be explained by the salting-in of gases. In addition, we have shown how to quantify chemical reaction acceleration in uncharged droplets of constant size measured on a single aerosol particle basis.

4.5 Acknowledgements

Chapter 4, in part, is a reprint of the material published by Environmental Science and Technology in: Angle, Kyle; Neal, Erin; Grassian, Vicki, Enhanced Rates of Transition-Metal-Ion-Catalyzed Oxidation of S(IV) in Aqueous Aerosols: Insights into Sulfate Aerosol Formation in the Atmosphere in 2021. The dissertation author was the primary investigator and author of this paper.

The authors thank Neal Arakawa (Environmental and Complex Analysis Laboratory, UCSD) for ICP-MS assistance and John Weeks (Wavemetrics) for providing support and files for Igor Pro fitting analysis. This material is based upon work supported by the National Science Foundation under Grant AGS1702488. Any opinions, findings, and conclusions or recommendations expressed in this material are those of the authors and do not necessarily reflect the views of the National Science Foundation.

4.6 Appendix

Supporting discussions, methods, calculations, figures, and tables can be found free of charge in the Supporting Information of the publication corresponding to this chapter.[55]

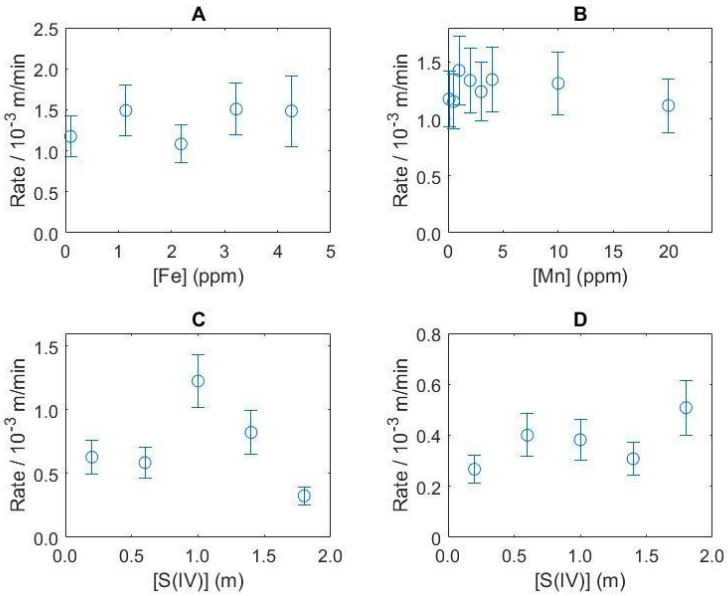

Figure 4.6: Results for bulk-phase experiments determining the impact of (**A**) Fe^{3+} and (**B**) Mn^{2+} concentrations on S(IV) oxidation rate for 1 m S(IV) samples. For Mn^{2+}, no trend is apparent, indicating only a catalytic amount is required. For Fe^{3+}, at most there is a weak postitive correlation, so enrichment of Fe^{3+} into the aerosol phase may partly contribute to reaction acceleration. (**C**) shows the results of increasing S(IV) concentration, which also increased ionic strength. (**D**) reflects experiments where the concentration of $NaClO_4$ was decreased as the concentration of S(IV) increased to maintain constant ionic strength. In both cases, to maintain a constant pH of 5.6, it was necessary to use more HCl, which in turn increased TMI concentration. For all four panels, error bars show 95% confidence intervals derived from the linear fit of sulfate concentration versus time.

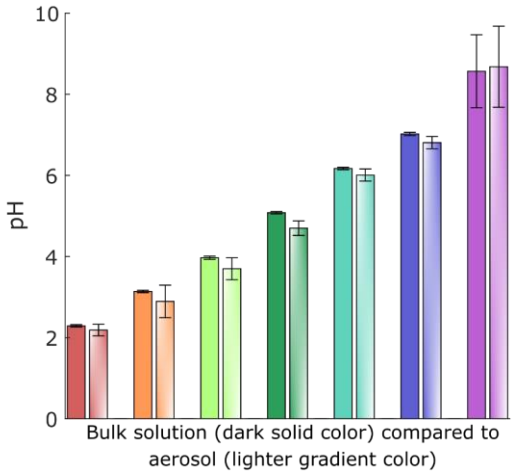

Figure 4.7: Comparison of pH for 1 m $S(IV)_{aq}$ solutions. Each pair shows measurements of the same sample, with the bulk on the left and aerosol on the right. Bulk solutions were prepared from sodium sulfite and acidified with 1 M HCl solution, then measured with both a pH probe and pH paper, with consistent results. Aerosols were impacted onto pH papers in triplicate. Error bars show one standard deviation. It can be seen that these pH values between bulk and aerosol phase are identical for most pH values, but in a few cases, there is slight acidification upon nebulization of the bulk solution to form the aerosol.

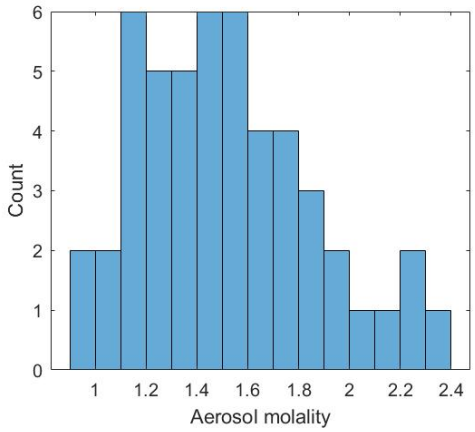

Figure 4.8: Distribution of aerosol-phase concentrations of sulfate when the same solution of 1 m Na_2SO_4 was nebulized into the optical tweezers and aerosols were trapped 50 times with the same laser power of 50 mW. Concentrations were calculated by refractive index as outlined in the Discussion. From this data, EF = 1.5 ± 0.3.

4.7 References

(1) Fioletov, V. E.; Mclinden, C. A.; Krotkov, N.; Li, C.; Joiner, J.; Theys, N.; Carn, S.; Moran, M. D. A Global Catalogue of Large SO_2 Sources and Emissions Derived from the Ozone Monitoring Instrument. *Atmos. Chem. Phys* **2016**, *16*, 11497–11519.

(2) Forbes, P. B. C.; Garland, R. M. Outdoor Air Pollution. *Compr. Anal. Chem.* **2016**, *73*, 73–96.

(3) Pye, H. O. T.; Nenes, A.; Alexander, B.; Ault, A. P.; Barth, M. C.; Clegg, S. L.; Collett, J. L.; Fahey, K. M.; Hennigan, C. J.; Herrmann, H.; Kanakidou, M.; Kelly, J. T.; Ku, I.-T.; Mcneill, V. F.; Riemer, N.; Schaefer, T.; Shi, G.; Tilgner, A.; Walker, J. T.; Wang, T.; Weber, R.; Xing, J.; Zaveri, R. A.; Zuend, A. The Acidity of Atmospheric Particles and Clouds. *Atmos. Chem. Phys.* **2020**, *20*, 4809–4888.

(4) Freedman, M. A.; Ott, E.-J. E.; Marak, K. E. Role of pH in Aerosol Processes and Measurement Challenges. *J. Phys. Chem. A* **2019**, *123* (7), 1275–1284.

(5) Duan, J.; Lyu, R.; Wang, Y.; Xie, X.; Wu, Y.; Tao, J.; Cheng, T.; Liu, Y.; Peng, Y.; Zhang, R.; He, Q.; Ga, W.; Zhang, X.; Zhang, Q. Particle Liquid Water Content and Aerosol Acidity Acting as Indicators of Aerosol Activation Changes in Cloud Condensation Nuclei (CCN) during Pollution Eruption in Guangzhou of South China. *Aerosol Air Qual. Res.* **2019**, *19*, 2662–2670.

(6) Wang, Y.; Zhang, Q.; Jiang, J.; Zhou, W.; Wang, B.; He, K.; Duan, F.; Zhang, Q.; Philip, S.; Xie, Y. Enhanced Sulfate Formation during China's Severe Winter Haze Episode in January 2013 Missing from Current Models. *J. Geophys. Res. Atmos.* **2014**, *119* (17), 10,425-10,440.

(7) Zheng, B.; Zhang, Q.; Zhang, Y.; He, K. B.; Wang, K.; Zheng, G. J.; Duan, F. K.; Ma, Y. L.; Kimoto, T. Heterogeneous Chemistry: A Mechanism Missing in Current Models to Explain Secondary Inorganic Aerosol Formation during the January 2013 Haze Episode in North China. *Atmos. Chem. Phys.* **2015**, *15* (4), 2031–2049.

(8) Connick, R. E.; Zhang, Y.-X.; Lee, S.; Adamic, R.; Chieng, P. Kinetics and Mechanism of the Oxidation of HSO_3^- by O_2. 1. the Uncatalyzed Reaction. *Inorg. Chem.* **1995**, *34* (18), 4543–4553.

(9) Martin, L. R.; Hill, M. W.; Tai, A. F.; Good, T. W. The Iron Catalyzed Oxidation of Sulfur(IV) in Aqueous Solution: Differing Effects of Organics at High and Low PH. *J. Geophys. Res.* **1991**, *96* (D2), 3085.

(10) Brandt, C.; van Eldik, R. Transition Metal-Catalyzed Oxidation of Sulfur(IV) Oxides: Atmospheric-Relevant Processes and Mechanisms. *Chem. Rev.* **1995**, *95* (1), 119–190.

(11) Zhang, H.; Xu, Y.; Jia, L. A Chamber Study of Catalytic Oxidation of SO_2 by Mn^{2+}/Fe^{3+} in Aerosol Water. *Atmos. Environ.* **2021**, *245*, 118019.

(12) Turšič, J.; Grgić, I.; Podkrajšek, B. Influence of Ionic Strength on Aqueous Oxidation of SO_2 Catalyzed by Manganese. *Atmos. Environ.* **2003**, *37* (19), 2589–2595.

(13) Connick, R. E.; Zhang, Y. X. Kinetics and Mechanism of the Oxidation of HSO_3- by O_2. 2. the Manganese(II)-Catalyzed Reaction. *Inorg. Chem.* **1996**, *35* (16), 4613–4621.

(14) Tao, W.; Su, H.; Zheng, G.; Wang, J.; Wei, C.; Liu, L.; Ma, N.; Li, M.; Zhang, Q.; Pöschl, U.; Cheng, Y. Aerosol pH and Chemical Regimes of Sulfate Formation in Aerosol Water during Winter Haze in the North China Plain. *Atmos. Chem. Phys.* **2020**, *20* (20), 11729–11746.

(15) Clarke, A. G.; Radojevic, M. Oxidation of SO_2 in Rainwater and Its Role in Acid Rain Chemistry. *Atmos. Environ.* **1987**, *21* (5), 1115–1123.

(16) Bertram, T. H.; Cochran, R. E.; Grassian, V. H.; Stone, E. A. Sea Spray Aerosol Chemical Composition: Elemental and Molecular Mimics for Laboratory Studies of Heterogeneous and Multiphase Reactions. *Chem. Soc. Rev.* **2018**, *47* (7), 2374–2400.

(17) Liu, T.; Chan, A. W. H.; Abbatt, J. P. D. Multiphase Oxidation of Sulfur Dioxide in Aerosol Particles: Implications for Sulfate Formation in Polluted Environments. *Environmental Science and Technology*. American Chemical Society 2021, p 4242.

(18) Yermakov, A. N.; Purmal, A. P. Iron-Catalyzed Oxidation of Sulfite: From Established Results to a New Understanding. *Prog. React. Kinet. Mech.* **2003**, *28* (3), 189–256.

(19) Warneck, P. The Oxidation of Sulfur(IV) by Reaction with Iron(III): A Critical Review and Data Analysis. *Phys. Chem. Chem. Phys.* **2018**, *20* (6), 4020–4037.

(20) The Merck Index Online - chemicals, drugs and biologicals https://www.rsc.org/merck-index (accessed Apr 22, 2020).

(21) Preston, T. C.; Reid, J. P. Accurate and Efficient Determination of the Radius, Refractive Index, and Dispersion of Weakly Absorbing Spherical Particle Using Whispering Gallery Modes. *J. Opt. Soc. Am. B* **2013**, *30* (8), 2113.

(22) Rafferty, A.; Gorkowski, K.; Zuend, A.; Preston, T. C. Optical Deformation of Single Aerosol Particles. *Proc. Natl. Acad. Sci. U. S. A.* **2019**, *116* (40), 19880–19886.

(23) Coddens, E. M.; Angle, K. J.; Grassian, V. H. Titration of Aerosol pH through Droplet Coalescence. *J. Phys. Chem. Lett.* **2019**, *10* (15), 4476–4483.

(24) Mudgal, P. K.; Sharma, A. K.; Mishra, C. D.; Bansal, S. P.; Gupta, K. S. Kinetics of Ammonia and Ammonium Ion Inhibition of the Atmospheric Oxidation of Aqueous Sulfur Dioxide by Oxygen. *J. Atmos. Chem.* **2008**, *61* (1), 31–55.

(25) Gupta, K. S.; Manoj, S. V.; Mudgal, P. K. Kinetics of Iron(III)-Catalyzed Autoxidation of Sulfur(IV) in Acetate Buffered Medium. *Transit. Met. Chem.* **2008**, *33* (3), 311–316.

(26) Angle, K. J.; Crocker, D. R.; Simpson, R. M. C.; Mayer, K. J.; Garofalo, L. A.; Moore, A. N.; Mora Garcia, S. L.; Or, V. W.; Srinivasan, S.; Farhan, M.; Sauer, J. S.; Lee, C.; Pothier, M. A.; Farmer, D. K.; Martz, T. R.; Bertram, T. H.; Cappa, C. D.; Prather, K. A.; Grassian, V. H. Acidity across the Interface from the Ocean Surface to Sea Spray Aerosol. *Proc. Natl. Acad. Sci.* **2021**, *118* (2), e2018397118.

(27) Beyad, Y.; Burns, R.; Puxty, G.; Maeder, M. A Speciation Study of Sulfur(IV) in Aqueous Solution. *Dalt. Trans.* **2014**, *43* (5), 2147–2152.

(28) Millero, F. J.; Yao, W.; Aicher, J. The Speciation of Fe(II) and Fe(III) in Natural Waters. *Mar. Chem.* **1995**, *50* (1–4), 21–39.

(29) Hem, J. D. Chemical Equilibria Affecting the Behavior of Manganese in Natural Water. *Int. Assoc. Sci. Hydrol. Bull.* **1963**, *8* (3), 30–37.

(30) Liu, T.; Clegg, S. L.; Abbatt, J. P. D. Fast Oxidation of Sulfur Dioxide by Hydrogen Peroxide in Deliquesced Aerosol Particles. *Proc. Natl. Acad. Sci. U. S. A.* **2020**, *117* (3), 1354–1359.

(31) Boyer, H. C.; Gorkowski, K.; Sullivan, R. C. In Situ pH Measurements of Individual Levitated Microdroplets Using Aerosol Optical Tweezers. *Anal. Chem.* **2020**, *92* (1), 1089–1096.

(32) Tang, I. N.; Tridico, A. C.; Fung, K. H. Thermodynamic and Optical Properties of Sea Salt Aerosols. *J. Geophys. Res. Atmos.* **1997**, *102* (19), 23269–23275.

(33) Tang, I. N.; Munkelwitz, H. R. Water Activities, Densities, and Refractive Indices of Aqueous Sulfates and Sodium Nitrate Droplets of Atmospheric Importance. *J. Geophys. Res.* **1994**, *99* (D9), 18801–18808.

(34) Bao, Z. C.; Barker, J. R. Temperature and Ionic Strength Effects on Some Reactions Involving Sulfate Radical [SO_4^-(Aq)]. *J. Phys. Chem.* **1996**, *100* (23), 9780–9787.

(35) Wei, Z.; Li, Y.; Cooks, R. G.; Yan, X. Accelerated Reaction Kinetics in Microdroplets: Overview and Recent Developments. *Annu. Rev. Phys. Chem.* **2020**, *71* (1), 31–51.

(36) Lee, J. K.; Samanta, D.; Nam, H. G.; Zare, R. N. Micrometer-Sized Water Droplets Induce Spontaneous Reduction. *J. Am. Chem. Soc.* **2019**, *141* (27), 10585–10589.

(37) Banerjee, S.; Gnanamani, E.; Yan, X.; Zare, R. N. Can All Bulk-Phase Reactions Be Accelerated in Microdroplets? *Analyst* **2017**, *142* (9), 1399–1402.

(38) Clarke, A. G.; Radojevic, M. Oxidation Rates of SO_2 in Sea-Water and Sea-Salt Aerosols. *Atmos. Environ.* **1984**, *18* (12), 2761–2767.

(39) Wang, W.; Liu, M.; Wang, T.; Song, Y.; Zhou, L.; Cao, J.; Hu, J.; Tang, G.; Chen, Z.; Li, Z.; Xu, Z.; Peng, C.; Lian, C.; Chen, Y.; Pan, Y.; Zhang, Y.; Sun, Y.; Li, W.; Zhu, T.; Tian, H.; Ge, M. Sulfate Formation Is Dominated by Manganese-Catalyzed Oxidation of SO_2 on

Aerosol Surfaces during Haze Events. *Nat. Commun.* **2021**, *12* (1), 1–10.

(40) Rovelli, G.; Jacobs, M. I.; Willis, M.; Rapf, R. J.; Prophet, A. M.; Wilson, K. R. A Critical Analysis of Electrospray Techniques for the Determination of Accelerated Rates and Mechanisms of Chemical Reactions in Droplets. *Chem. Sci.* **2020**, *11* (48), 13026.

(41) Wilson, K. R.; Prophet, A. M.; Rovelli, G.; Willis, M. D.; Rapf, R. J.; Jacobs, M. I. A Kinetic Description of How Interfaces Accelerate Reactions in Micro-Compartments. *Chem. Sci.* **2020**, *11* (32), 8533–8545.

(42) Eriksen, T. Self-Diffusion Studies in Aqueous Sulfite Solutions. *Chem. Eng. Sci.* **1967**, *22*, 727–736.

(43) Das, T. N. Reactivity and Role of $SO_5^{\bullet-}$ Radical in Aqueous Medium Chain Oxidation of Sulfite to Sulfate and Atmospheric Sulfuric Acid Generation. *J. Phys. Chem. A* **2001**, *105* (40), 9142–9155.

(44) Luo, M.; Wauer, N. A.; Angle, K. J.; Dommer, A. C.; Song, M.; Nowak, C. M.; Amaro, R. E.; Grassian, V. H. Insights into the Behavior of Nonanoic Acid and Its Conjugate Base at the Air/Water Interface through a Combined Experimental and Theoretical Approach. *Chem. Sci.* **2020**, *11* (39), 10647–10656.

(45) Ruiz-Lopez, M. F.; Francisco, J. S.; Martins-Costa, M. T. C.; Anglada, J. M. Molecular Reactions at Aqueous Interfaces. *Nat. Rev. Chem.* **2020**, *4* (9), 459–475.

(46) Lee, J. K.; Walker, K. L.; Han, H. S.; Kang, J.; Prinz, F. B.; Waymouth, R. M.; Nam, H. G.; Zare, R. N. Spontaneous Generation of Hydrogen Peroxide from Aqueous Microdroplets. *Proc. Natl. Acad. Sci. U. S. A.* **2019**, *116* (39), 19294–19298.

(47) Maaß, F.; Elias, H.; Wannowius, K. J. Kinetics of the Oxidation of Hydrogen Sulfite by Hydrogen Peroxide in Aqueous Solution: Ionic Strength Effects and Temperature Dependence. *Atmos. Environ.* **1999**, *33* (27), 4413–4419.

(48) Craig, R. L.; Peterson, P. K.; Nandy, L.; Lei, Z.; Hossain, M. A.; Camarena, S.; Dodson, R. A.; Cook, R. D.; Dutcher, C. S.; Ault, A. P. Direct Determination of Aerosol PH: Size-Resolved Measurements of Submicrometer and Supermicrometer Aqueous Particles. *Anal. Chem.* **2018**, *90* (19), 11232–11239.

(49) Li, G.; Su, H.; Ma, N.; Zheng, G.; Kuhn, U.; Li, M.; Klimach, T.; Pöschl, U.; Cheng, Y. Multifactor Colorimetric Analysis on PH-Indicator Papers: An Optimized Approach for Direct Determination of Ambient Aerosol PH. *Atmos. Meas. Tech.* **2020**, *13* (11), 6053–6065.

(50) Wei, H.; Vejerano, E. P.; Leng, W.; Huang, Q.; Willner, M. R.; Marr, L. C.; Vikesland, P. J. Aerosol Microdroplets Exhibit a Stable pH Gradient. *Proc. Natl. Acad. Sci. U. S. A.* **2018**, *115* (28), 7272–7277.

(51) Hung, H. M.; Hsu, M. N.; Hoffmann, M. R. Quantification of SO_2 Oxidation on Interfacial

Surfaces of Acidic Micro-Droplets: Implication for Ambient Sulfate Formation. *Environ. Sci. Technol.* **2018**, *52* (16), 9079–9086.

(52) Colussi, A. J. Can the pH at the Air/Water Interface Be Different from the pH of Bulk Water? *Proc. Natl. Acad. Sci. U. S. A.* **2018**, *115* (34), E7887.

(53) Das, S.; Imoto, S.; Sun, S.; Nagata, Y.; Backus, E. H. G.; Bonn, M. Nature of Excess Hydrated Proton at the Water-Air Interface. *J. Am. Chem. Soc.* **2020**, *142* (2), 945–952.

(54) De Haan, D. O.; Corrigan, A. L.; Smith, K. W.; Stroik, D. R.; Turley, J. J.; Lee, F. E.; Tolbert, M. A.; Jimenez, J. L.; Cordova, K. E.; Ferrell, G. R. Secondary Organic Aerosol-Forming Reactions of Glyoxal with Amino Acids. *Environ. Sci. Technol.* **2009**, *43* (8), 2818–2824.

(55) Angle, K. J.; Neal, E. E.; Grassian, V. H. Enhanced Rates of Transition-Metal-Ion-Catalyzed Oxidation of S(IV) in Aqueous Aerosols: Insights into Sulfate Aerosol Formation in the Atmosphere. *Environ. Sci. Technol.* **2021**, *55* (15), 10291–10299.

CHAPTER 5 ORGANIC ACID EVAPORATION KINETICS FROM AQUEOUS AEROSOLS: IMPLICATIONS FOR AEROSOL BUFFERING CAPACITY IN THE ATMOSPHERE

5.1 Abstract

The acidity of atmospheric aerosols controls their impacts on heterogeneous and multiphase reactions, cloud formation, and human health. Recently, it has been shown that multiphase buffering can shift aerosol pH substantially compared to bulk solutions. Here, we highlight a unique type of multiphase buffering for aerosols that occurs when organic acids partition from aqueous salt aerosols upon acidification with a strong acid. In this case, rather than lowering the pH of the aerosol, titration with strong acids lowers the organic fraction within the aerosol while maintaining constant pH. We investigate evaporation rate for the model system lactic acid as well as other atmospherically-relevant species such as acetic, butyric, and methacrylic acids. We demonstrate that the timescales for evaporation of organic acids from aerosols are on the order of minutes, comparable to acidification rates in the atmosphere. The organic acid evaporation we observe for lactic acid in salt aerosols is enhanced compared to bulk measurements within what is expected based on differences in surface to volume ratios, indicating surface effects are important. In addition, we show that a salting-out effect drives small organic molecules to the surface, where they quickly evaporate, removing acidity and causing a "superbuffering" effect. Our results can explain why aerosols in the acidic pH range from 2 to 4 are able to resist further acidification by strong acids in the atmosphere. Overall, this work highlights unique properties of concentrated aerosols and demonstrates how inorganic ions and organic compounds together control multiphase buffering in the atmosphere.

5.2 Introduction

Aerosol pH is a critical parameter for atmospheric chemistry. The pH of a particle impacts the surface propensity of fatty[1] and amino acids,[2] multiphase chemical reactions,[3,4] and even the likelihood of the aerosol to seed a cloud.[5,6] In addition, highly acidic aerosols have detrimental effects on human health.[7,8] Since it is challenging to directly measure the pH of aerosols, which can have volumes smaller than one femtoliter, aerosol pH is commonly calculated by thermodynamic models which take aerosol and/or gas phase concentrations as inputs.[9,10] These models can be useful, but they assume the aerosol is at equilibrium. Limitations of this assumption can potentially lead to erroneous results. Direct measurements of aerosol pH indicate that particles can be rapidly acidified to pH values of 2 to 4 depending on particle size,[11] and several studies show that atmospherically aged aerosols can become very acidic with pH values < 0 while others remain in the pH 1 to 4 range.[9,12]

Another key aerosol parameter is organic fraction. For example, water-soluble organic compounds impact hygroscopicity of aerosols and in turn cloud condensation nuclei activity.[13] Aerosols with a significant organic fraction can adopt a morphology of a highly viscous outer layer enclosing an aqueous core, which impacts aerosol reactivity.[14] The identity of the organics as speciated by mass spectrometry has frequently been used for source apportionment to give insight into the origin of aerosols from pollution events and natural emissions.[15] It is also important to track what organics partition *from* aerosols back into the atmosphere, as these species can then serve as gas-phase precursors for reactions producing additional secondary organic aerosols.[8]

The partitioning of organic acids influences both aerosol pH and organic fraction. While many studies have been conducted on the uptake of organics by aerosols, the loss of organics through partitioning from the aerosol into the gas phase has received much less attention. A study

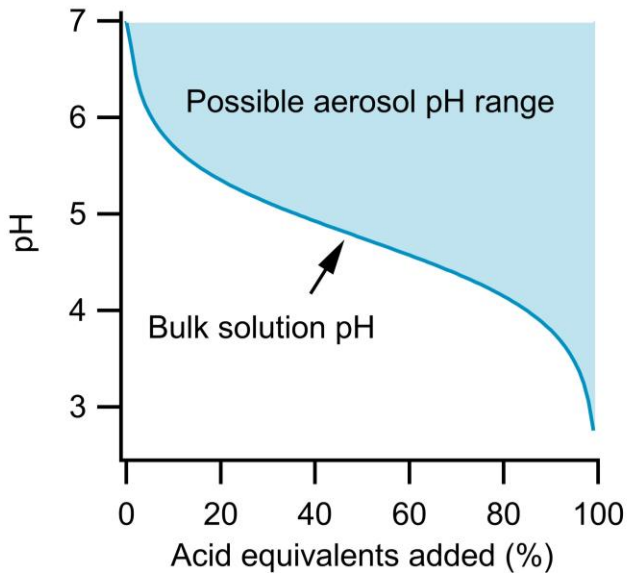

Figure 5.1: Comparison of theoretical titration for bulk solution and aerosol.

by Meng *et al.* used thermodynamic data to show that formic and acetic acids should be found overwhelmingly in the gas phase and are negligible in the aerosol phase.[16] Some data indicates that these acids may be formed by aging aerosols, and thus, we would expect these acids to partition out of the aerosol.[17] This process reduces the organic fraction and increases the pH of the system toward neutral pH by removing the organic acid.

Figure 5.1 illustrates the differences in the titration of a bulk solution and an aerosol. For both phases, the initial system is 1 m sodium acetate. Strong acid is then added to neutralize this conjugate base, according to Equation 5.1.

$$A^-(aq) + H^+ \rightarrow HA\,(aq) \qquad (5.1)$$

For the bulk solution, the pH of the system follows a simple titration curve via the Henderson-Hasselbalch equation, shown by the dark line. The aerosol could follow this same pH profile. However, given that the acetic acid that is formed partitions out of the system, the particle could actually remain neutral if all of the formed acetic acid evaporates, as in Equation 5.2.

$$HA\ (aq) \rightarrow HA\ (g) \qquad (5.2)$$

In fact, the pH of the aerosol could lie anywhere in the shaded area during the titration depending on the rate at which the acetic acid evaporates and the concentration of acetic acid in the gas phase. For example, at 50% acid equivalent added, the pH could be as low as 4.75 (the pK_a of acetic acid) or as high as 7 if all the acidic protons have been taken up by acetate that has then evaporated as acetic acid if the concentration of acetic acid in the surrounding air is low.

Aerosols therefore have potential for a greater buffering capacity than a corresponding bulk solution of identical composition due to the greater importance of Equation 5.2. The difference between bulk and aerosol buffering has previously been highlighted by Zheng *et al*. who showed that the ammonia/ammonium conjugate pair, which buffers bulk solutions at an alkaline pH, has a more acidic peak buffering capacity in aerosols.[18] This assessment was made on the assumption of aerosol equilibrium, but given Figure 5.1, it is also important to consider the kinetics of partitioning as well. Recently, Li *et al.* quantified the kinetics of ammonia depletion for substrate-deposited aerosols mixed with nanoparticles to monitor droplet pH.[19] They found evaporation to take ca. 10 minutes for 20-micron aerosols, showing that the process can be monitored on reasonable timescales with Raman spectroscopy. Kohli *et al.* measured the evaporation of aerosols containing various ethylene glycols and found evaporation on timescales of minutes to hours depending on the conditions.[20] It is also known that small organics such as ethanol evaporate in seconds from single aerosols, and while this can be useful in introducing new species (dissolved in ethanol) to a levitated aerosol and then allowing the ethanol to evaporate, this process is too fast for a detailed kinetics study of organic evaporation.[21]

In this study, we report measurements of the evaporation of organic acids from single, optically levitated micron-sized aqueous salt aerosols. Our aim is to provide insight into the

timescales of processes controlling aerosol pH and aerosol organic mass fraction by studying atmospherically relevant acids. Specifically, we have investigated the evaporation of acetic, butyric and methacrylic acids.[22] We also extensively studied lactic acid as a model system for a more viscous organic acid. Overall, we find that when organic acids volatilize quickly, aerosols exhibit what we have termed a "superbuffering" capacity, where more acidity is removed from the particle (via Equation 5.2) than would occur for a bulk solution.

5.3 Methods

Solutions were prepared using milliQ water with resistivity > 18.1 MΩ. NaCl (Fisher, Certified ACS) and Na_2SO_4 (Fisher, Certified ACS) were baked at 200 °C for at least 48 h to remove organic impurities. Sodium nitrate (Sigma-Aldrich, ReagentPlus), hydrochloric acid (Fisher, Certified 5.95-6.05 N), methacrylic acid (Thermo Scientific, 99+%), acetic acid (Fisher, glacial, Certified ACS), lactic acid (Fisher, 85% w/w in H_2O, Certified ACS), butyric acid (Fisher, >99%), and dimethylamine (Aldrich, 40 wt. % in H_2O) were used without further purification. Samples were created by weighing the solids into a 20 mL scintillation vial with a Teflon cap, then adding the appropriate volume of solvents and dissolving the solids via agitation. Measurements of pH were carried out with a pH meter (OAKTON Instruments) calibrated with pH 4 and 7 buffers.

For aerosol-phase experiments, single micron-sized aerosols were trapped using a commercial Aerosol Optical Tweezers 100 (Biral Inc.). Solutions were nebulized using an ultrasonic nebulizer (MicroAIR U22, OMRON) and self-coalesced in the optical trap to obtain a particle of the appropriate size, typically with a radius of 4 ± 1 μm. Precise control of aerosol size was not necessary since curvature effects have little importance in this micrometer size regime and past studies have indicated evaporation processes to be nearly size-independent even for

submicron aerosols.[23] Relative humidity (RH) was maintained at 80 ± 3% by a 30 sccm flow of a mixture of wet and dry N_2 gas. A faster flow rate was avoided to prevent unnecessary convection, which has previously been recognized as a potential source of degassing acceleration.[19] We also acknowledge that any RH flow (which is necessary to prevent the particle from drying out) may lead to continuous condensation of water onto the aerosol particle, which could have a plasticizing effect, decreasing the time needed for the aerosol to reach equilibrium.[24] Nebulized aqueous salt aerosols are emitted at ca. 100% RH, so water equilibration times to an 80% RH environment are theoretically on the order of milliseconds.[25] Temperature was typically 24.6 ± 0.1 °C and minimal heating from the 532 nm laser is expected.[26] Once aerosols were trapped, Raman spectra were collected every second on the 1200 g/mm setting, with the spectrum centered on either 570 nm to obtain kinetically useful bands or 645 nm to obtain Whispering Gallery Mode (WGM) data for the calculation of aerosol size and refractive index. Raman frequencies were calibrated with standard emission lines from a Ne/Ar and Hg light source (Princeton Instruments). Raman frequencies are labeled for convenience only, and peaks may shift by ca. ± 4 cm^{-1} depending on pH, solute concentrations, and phase. For some experiments, aerosols were coalesced with HCl to lower the pH as has been previously described.[27]

For bulk-phase experiments, a confocal Raman spectrometer (HORIBA, LabRam HR Evolution) was used with the LabSpec 8 software. 6 mL of the given solution was transferred into a glass petri dish (d = 49 mm) and placed on the stage under the microscope. Real time spectra centered at 3400 cm^{-1} were acquired as the height of the stage was adjusted until the maximum signal from the broad water band was observed, and then the stage was moved slightly past this point to maintain optimal signal for as long as possible, as previously discussed.[4] 7 second acquisition times with 5 co-added scans were used on the 1800 g/mm setting, allowing the range

of 400 to 4000 cm^{-1} to be analyzed in less than 10 minutes. Temperature was typically 23 ± 1 °C. A custom MATLAB script was written to initiate spectral collection precisely every 10 minutes until enough data was obtained.

For both types of experiments, spectral data were analyzed with the Multipeak Fitting package from Igor Pro (Wavemetrics). Area versus time data for the internal standard, if not constant, was first analyzed to remove influence from WGM by eliminating positive outliers. It was visually confirmed in several cases that these outliers corresponded to WGM by using the Lara Offline software (Biral Inc.). (The use of an internal standard is necessary in the aerosol phase because the aerosol can change size during the experiment, and in the bulk phase because the required timescale of hours results in water evaporation.) The internal standard data were then fit to a linear equation to allow interpolation for missing data points from the removal of WGMs. Then, the kinetics data from the Raman band of interest (usually the C–C stretch, specifically the C–COOH peak, between 800 and 930 cm^{-1}) was normalized to this fit. The WGM interference from the kinetics data was also removed, and then the resulting dataset was fit to a $\ln(A/A_0)$ vs time function, where A is the peak area at a given time and A_0 is the initial peak area. We note that spectral frequencies labeled on figures are provided for convenience and may shift by a few wavenumbers between experiments due to differences in ionic strength, solution composition, or bulk vs aerosol phase. All post-Igor processing was carried out using custom MATLAB scripts.

The refractive index of solutions was measured with an ABBE-3L refractometer (Bausch & Lomb). About 0.5 mL of each solution was pipetted onto the refractometer prism and a sodium lamp was used to illuminate each sample for alignment. Pictures of the illuminated images were taken with a smartphone camera and processed in Inkscape to count the pixels per refractive index unit and calculate refractive index. In the AOT, refractive index was measured from the WGM

bands on the water O-H stretch at 650 nm. Since bulk measurements were performed at the standard 589 nm, the AOT refractive index was converted to this wavelength using Equation 5.3.[28]

$$n_a = n_b + D_1\left(\frac{1}{\lambda_a} - \frac{1}{\lambda_b}\right) + D_2\left(\frac{1}{\lambda_a} - \frac{1}{\lambda_b}\right)^2 \qquad 5.3$$

Here, n is refractive index, λ is wavelength, and D_1 and D_2 are the first and second dispersion terms, which are also measured by the AOT.

Surface tension data was obtained with an AquaPi tensiometer (Kibron) with Teflon sample cups. The tensiometer was calibrated with milliQ water to 72.8 ± 0.1 mN/m. Each pair of salt solution and salt solution + organic acid was measured repeatedly until measurements agreed, and the tensiometer was cleaned with milliQ water and a butane torch between measurements.

5.4 Results and Analysis

5.4.1 Experimental Results and Analysis

In order to quantify organic acid evaporation from aerosols, we first determined which Raman peaks were sensitive to the presence of the acid, the conjugate base, and both species. Peak assignments are given primarily based on previous studies.[29] In the case of lactic acid, which we consider first, the stretching mode of the carbon-carbon single bond adjacent to the carboxylic acid group (i.e. the C–COOH stretching mode) is strong in the Raman spectra. Its frequency is 830 cm^{-1} which is useful as it is well-resolved and there is a clear shift for the corresponding peak for the base (i.e. the $C–COO^-$ stretching mode) at 856 cm^{-1} (see Figure 5.2a). Therefore, this was the peak used for monitoring the presence of lactic acid in the aerosol without interference from lactate.[29] The 1730 cm^{-1} peak due to the protonated C=O in the carboxylic acid group (-COOH) is

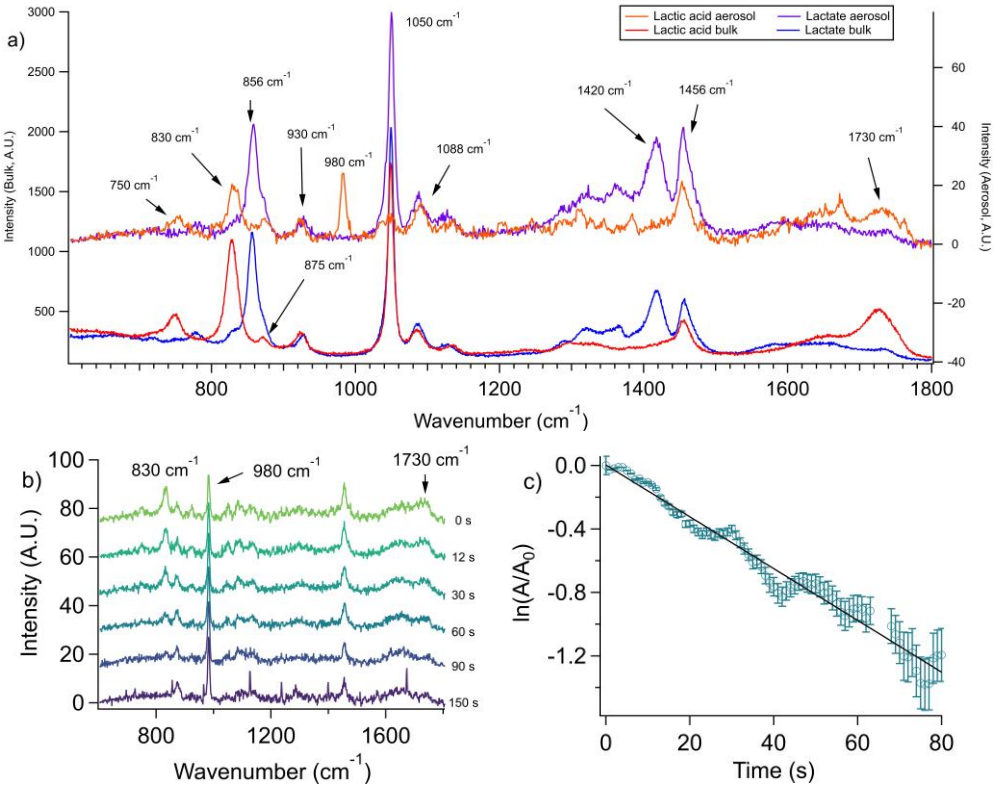

Figure 5.2: Lactic acid evaporation. (a) Comparison of aerosol (top traces) and bulk (bottom traces) Raman spectra. Bulk solutions were 1 m lactic acid, neutralized with KOH if lactate was needed, and aerosol solutions were created by nebulizing these solutions. Useful frequencies are labeled. (b) Aerosol spectra, where lactic acid evaporates in 150 s as indicated by the 830 cm^{-1} C-COOH peak. Sulfate (980 cm^{-1}) was used as the internal standard. Sharp frequencies in the bottom spectrum correspond to WGMs. (c) First-order kinetic fit to the loss of the C-COOH peak area in lactic acid at 830 cm^{-1}. The fit has a slope of -0.016 s^{-1} and an R^2 of 0.97.

broad and weak in the Raman spectrum and therefore difficult to use for kinetic analysis. Nevertheless it is qualitatively useful to corroborate lactic acid evaporation from the aerosol (see Figure 5.2b). We used sodium sulfate as our internal standard (980 cm^{-1} band), which in our pH range ($\geq$ 3.2) is non-volatile as a dianion and works well as a standard.[27]

Lactic acid evaporates very slowly from bulk solutions which is unsurprising given its boiling point is greater than that of water. Spectra were collected over a 13 hour timescale. After ca. 11 hours of evaporation, lactic acid begins to crystallize, complicating the kinetics. In addition,

water evaporation is significant on this timescale, which would increase the lactic acid concentration and hence the lactic acid signal. To account for this, we tracked the peak area of the C-COOH 830 cm^{-1} band normalized to the sulfate internal standard. By evaluating only data before lactic acid crystallization, the bulk evaporation rate for 1.5 m lactic acid in a 1.5 m NaCl solution was determined to be $4.8 \pm 0.3 * 10^{-6}$ s^{-1}.

Next, we performed experiments on the same solution but for micron-sized aerosol. Representative spectra are given in Figure 5.2b. The loss of the C-C peak area versus the internal standard peak area fit first-order kinetics well (Figure 5.2c). The slope of this graph gives a rate constant *k* for the initial loss of lactic acid. From replicate experiments, *k* was found to be $1.2 \pm 0.3 * 10^{-2}$ s^{-1}, which is $2.6 * 10^{3}$ faster than the corresponding bulk evaporation. The surface area to volume (hereafter S:V) ratio for the bulk system is ca. 3.1 cm^{-1}. The S:V ratio for a 4 micron aerosol is 7500 cm^{-1}. Thus, the aerosol S:V ratio is greater by a factor of $2.4 * 10^{3}$. This number is within the evaporation rate ratio of $2.6 \pm 0.7 * 10^{3}$ with propagated error.

To gain insight into the factors controlling the rate of organic evaporation from aerosols, we performed experiments varying the concentration of lactic acid and sodium chloride in the bulk solutions used to prepare the aerosols. The results are shown in Figure 5.3a. At a given [NaCl], when we decrease [lactic acid], the rate constant increases. This may seem surprising, given that first-order rate constants are insensitive to concentration. However, here, a large decrease in lactic acid substantially decreases the viscosity of the aerosol, which decreases the resistance experienced by a molecule moving through the aerosol and to the aerosol surface to evaporate. Our finding highlights an important feature of aerosol chemistry for atmospheric kinetics. The viscosity of aerosols can vary by orders of magnitude depending on the RH,[30,31] and viscosity can

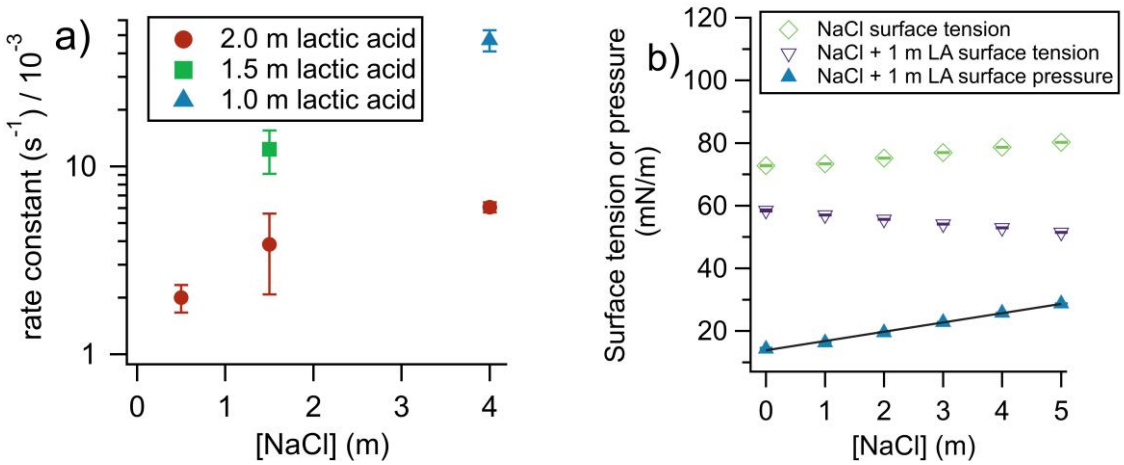

Figure 5.3: Impact of aerosol composition on reaction rate. (a) When [lactic acid] is increased, the rate decreases due to an increase in viscosity (*vide infra*). When NaCl is added there is a rate increase, due to a "salting-out" effect on lactic acid. (b) Surface tension and surface pressure of 1 m lactic acid (LA) solutions. The surface pressure data show the difference between the surface tension of NaCl solutions and NaCl solutions with added lactic acid (see Equation 4). The surface pressure fit shows how NaCl can drive lactic acid to the air-water interface for bulk solutions. The non-zero intercept of the surface pressure fit at 13.8 mN/m is expected because lactic acid has surface activity even in the absence of salt. The slope is 2.96 (mN/m)/m_{NaCl} and R^2 is 0.997. Error bars, smaller than the symbols, show standard deviation of replicates.

be sensitive to different parameters including biological activity in the ocean for sea spray aerosols.[32] Therefore, where possible, atmospheric kinetics modeling for partitioning processes should incorporate viscosity. We focused on aerosols at 80% RH, but future investigations could target lower RH conditions where viscosity is orders of magnitude larger and evaporation kinetics would be considerably slower. As an additional note, the viscosity analysis reveals that caution should be taken in comparing aerosol- and bulk-phase rates. For aerosols, as evaporation of a viscous organic occurs, the aerosol viscosity decreases, accelerating further evaporation. For the bulk, as water evaporates faster than the organic, viscosity increases, slowing further evaporation. Therefore, a comparison of the two is only semi-quantitative and should not be over interpreted as

evidence of unique surface effects of aerosols. Instead, multiple processes are occurring simultaneously which need to be taken into account.

Figure 5.3a also shows the changes in the rate of lactic acid evaporation from the aqueous aerosol as a function of sodium chloride concentration. Faster rates are found for higher concentrations of NaCl. This likely has to do with a "salting-out" effect where inorganic ions and organic molecules compete for hydration and organics are thus more easily lost from the aqueous phase.[33,34] The literature on salting out effects is complex. For NaCl, salting out has been observed for a wide range of molecules.[33,35] For pure acetic acid aerosols, however, it has been found that adding NaCl does not impact the rate of organic evaporation, probably due to the already very high volatility of acetic acid.[36] Theoretically, the equilibrium behavior caused by salting out can be quantified by Sechenov coefficients, but unfortunately these coefficients are scarce in the literature and not available for lactic acid.[37] To determine if salting out was occurring here, we measured the surface pressure, π, for a series of solutions of 1 m lactic acid with increasing [NaCl] (Figure 5.3b). Equation 5.4 provides a definition of π:

$$\pi = \gamma_0 - \gamma \qquad 5.4$$

where, γ_0 is the surface tension of an NaCl solution and γ is the surface tension of the same solution with 1 m lactic acid. The data show that NaCl increases the surface activity of lactic acid. In particular, in a solution with 4 m NaCl, the surface activity of lactic acid doubles compared to a solution with no NaCl. With this increased surface activity, the lactic acid is more likely to reside at the interface where it can readily evaporate from an aerosol. Furthermore, the increase in viscosity due to added NaCl is completely negated by the salting-out effect. Indeed, a 4 m NaCl solution has a viscosity of 1.35 cP,[38] while a 2 m lactic acid solution has a viscosity of ca. 1.31 cP.[39] Despite this substantial increase in viscosity, the rate of evaporation nevertheless increases

with increasing [NaCl], indicating that salting-out is a key factor for the prediction of organic partitioning.

To determine whether salting-out by NaCl is enhanced in the aerosol phase, ideally, the kinetics of bulk solutions and aerosols free of NaCl should be compared. In practice, we found NaCl-free lactic acid aerosols to be too unstable to provide reliable data. Instead, we extrapolated the 2 m lactic acid data shown in Figure 5.3a to a 0 m NaCl concentration and obtained a k of 1.8 $\pm$ 0.5 * 10^{-3} s^{-1}. The corresponding bulk kinetics experiment with 2 m lactic acid and no NaCl gave a k of 2.0 $\pm$ 0.7* 10^{-6} s^{-1}. This corresponds to an aerosol-phase enhancement of 900. Therefore, at least for the case of NaCl, salting-out appears to be enhanced in the aerosol phase and accelerates evaporation kinetics.

One of our goals was to determine timescales for this superbuffering effect of salt aerosols. To do this, we needed to show whether the acidification process of organic bases significantly contributes to the total time needed for organic acids to evaporate. Although acid-base chemistry is known to be very fast, phenomena such as concentration gradients could impact reaction rates.[4] To test this, we performed some experiments by trapping aerosols composed of lactic acid and others by trapping sodium lactate and acidifying the aerosol with HCl. For these acidification experiments, the same approach was applied as described above, and the rate at 95% confidence is 1.6 $\pm$ 0.6 * 10^{-2} s^{-1}. The large confidence interval is due to variability between experiments, since enrichment factors apply to both the initial aerosol and the coalescing aerosol, as well as variability in the size of the aerosol that coalesces with the trapped aerosol. Nevertheless, the titration (initial lactate aerosol) 95% confidence interval encompasses the non-titration (initial lactic acid aerosol) 95% confidence interval of 1.2 $\pm$ 0.3 * 10^{-2} s^{-1}. This is a key point because it indicates that the titration step does not impact the evaporation rate. The utility of this result is that other experiments

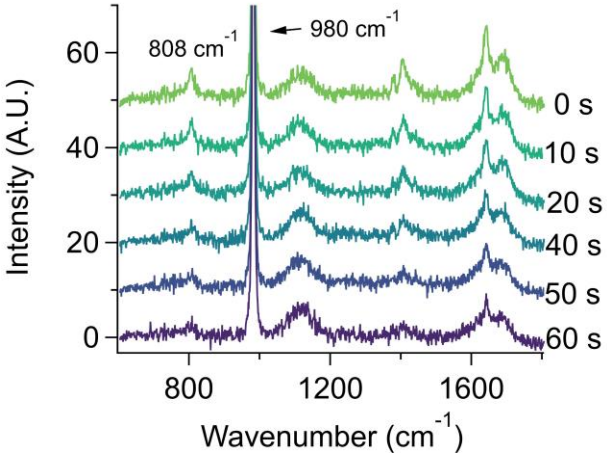

Figure 5.4: Raman spectra of aqueous salt aerosols containing 0.67 m methacrylic acid and 0.67 m sodium sulfate. The methacrylic acid evaporation over a 60 s time span is seen by the decrease in the 808 cm^{-1} peak, due to the C–COOH stretching mode. Traces show averages of the co-addition of 11 consecutive 1 second spectra each.

can be performed by trapping an aerosol that initially contains an acid and omitting the acidification step, which reduces sources of experimental variability.

The behavior of methacrylic acid was found to be similar to lactic acid. Unfortunately, due to solubility limitations and the requirement of high concentrations in the aerosol phase to obtain quantitative data with Raman spectroscopy, it was not practical to carry out concentration- or salt-dependent studies for methacrylic acid. However, we were able to obtain reproducible data for aerosols generated from bulk solutions of 0.67 m methacrylic acid and 0.67 m sodium sulfate at pH 2.9. Representative spectra are given in Figure 5.4, where the loss of the 808 cm^{-1} peak corresponds to the loss of methacrylic acid. From replicate experiments we obtained a first order rate constant of 0.029 ± 0.014 s^{-1}. The corresponding rate constant for a bulk solution is 3.69 ± 0.06 * 10^{-5} s^{-1}. This represents an aerosol-phase acceleration factor of ca. 800, which is fully accounted for by the difference in the S:V ratios.

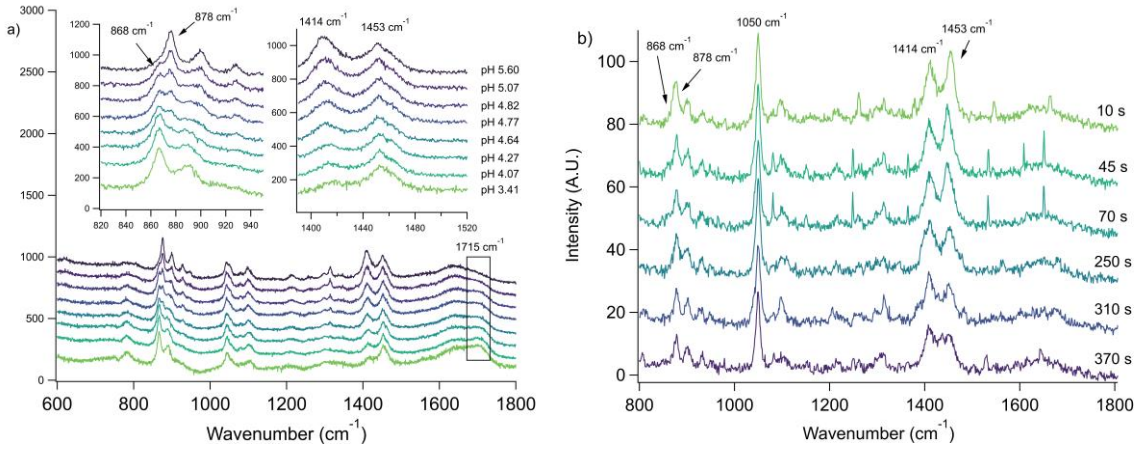

Figure 5.5: Raman spectra of butyric acid. (a) Confocal spectra with insets showing spectral differences at various pH levels. The broad boxed COOH band at 1715 cm^{-1} also shows pH-dependence. From top to bottom, the pH values are 5.60, 5.07, 4.82, 4.77, 4.64, 4.27, 4.07. and 3.41. The uncertainty for each is ± 0.04 pH units. (b) Aerosol phase traces (averages of 11 spectra each) showing butyric acid evaporation and pH increase. The sharp features correspond to WGMs.

We anticipate salting-out to be less important for methacrylic acid. Based on surface tension measurements, methacrylic acid has a higher π than lactic acid for the same concentration of sodium chloride. However, the slope of the π vs. [NaCl] plot is smaller, showing that methacrylic acid is less sensitive to salting out as [NaCl] increases. This illustrates the possibility that molecules which are more surface active on their own will be less sensitive to salting-out, which makes sense because more of the molecules would already have limited hydration spheres at the air-water interface.

Next, we consider aerosol evaporation data from two other carboxylic acids, namely acetic and butyric acid. The bulk Raman spectra for butyric acid is given in Figure 5.5a. The carbon-carbon symmetric stretch peaks observed for the C–COOH and C–COO^- groups in butyric acid and butyrate are at 868 and 878 cm^{-1}, respectively. There are also several peaks due to the symmetric and asymmetric bending modes of CH_2 and CH_3 groups in the 1400 to 1480 cm^{-1} range. Rather than resolve them individually, we simply note the ratio of the maxima at 1414 and 1453

cm^{-1} is sensitive to pH as shown in Figure 5.5a. An additional note for these experiments is that we chose sodium nitrate as the internal standard due to its very strong Raman band at 1050 cm^{-1} which is useful for experiments involving coalescence.

The C–COOH and C–COO^- stretching mode peaks at 868 and 878 cm^{-1}, respectively, can be resolved by peak fitting in confocal spectroscopy, but due to lower resolution of the Raman spectrometer in the aerosol optical tweezers, these peaks are found to be less reliable for quantitative analysis. The presence of butyric acid can be qualitatively seen by the 868 cm^{-1} shoulder which decreases in subsequent spectra as the acid evaporates. This phenomenon can be more clearly seen in the ratio of the 1414 and 1453 cm^{-1} maxima. When the aerosol is first trapped, the 1453 cm^{-1} peak has greater intensity, indicating the system contains more butyric acid than butyrate. After 70 seconds, the peaks have nearly equal intensity. At this point, there is a gap in the spectral data as the instrument grating was shifted to obtain the size and refractive index of the aerosol. Upon returning at 250 seconds, the 1414 cm^{-1} peak is now more intense, indicating an increase in pH.

There is significant uncertainty associated with the shoulder at 868 cm^{-1} due to peak overlap. There is also no guarantee that the 1414 to 1453 cm^{-1} peak ratio corresponds to the same numerical butyric acid to butyrate relationship as the bulk. Indeed, we have previously observed differences in broad peaks for bulk- and aerosol-phase Raman spectra,[27] which may be due to heterogeneous broadening.[40] For a 4-micron radius aerosol, at any moment in time, ca. 7.3% of the molecules are within 100 nm of the interface, while for the bulk phase in our conditions, only 0.003% are. This leads to more variations for bond environments in the aerosol phase. A clear example of the varying peak prominence between phases can be seen in Figure 5.5 in the 1715 cm^{-1} COOH peak, corresponding to butyric acid, which is only visible in the bulk phase.

Nevertheless, in order to determine a lower bound rate constant, we assumed the ratio of the peaks corresponded to the same acid to base ratio as the bulk and calculated a rate constant of 0.02 s^{-1}, with the understanding that the real-world rate could be an order of magnitude faster or more depending on the conditions. Comparing this to the bulk rate of 2.70 ± 0.05 * 10^{-5} s^{-1}, the aerosol evaporation rate is faster by a factor of ca. 10^3.

Acetic acid was found to evaporate even faster than butyric acid. We were unable to obtain individual spectra giving evidence that acetic acid was present in the aerosol phase, and the acidification of sodium acetate led to loss of all organic signal faster than the time required for the aerosol to stabilize (ca. 3 seconds). We therefore conclude that acetic acid evaporation likely occurs on the timescale of milliseconds or faster and that it is unlikely to be detected in atmospheric aerosols, consistent with predictions.[16] Acetic acid may be detected in aerosols with higher organic fractions and at lower RH conditions.[41]

To demonstrate that the observed evaporation was not a function of other experimental variables and conditions such as surrounding water vapor slowly replacing organics in the aerosol, we performed experiments with the dimethylammonium cation, DMAH, a charged protonated

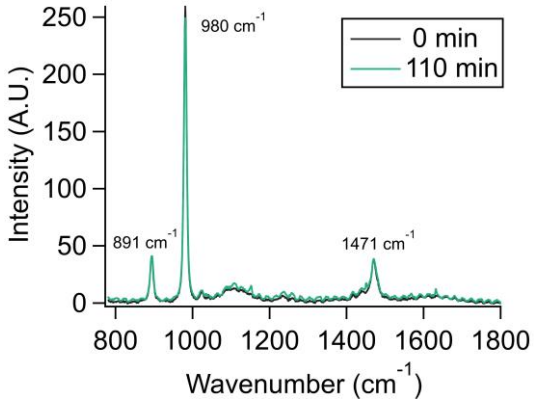

Figure 5.6: Aerosol spectra of dimethylammonium cation. Spectral bands do not significantly change over 110 minutes. Traces show an average of 70 spectra each to show peaks more clearly, which creates the oscillation-like artifact in the 110 min spectrum due to movement of WMGs.

species that does not evaporate from the aerosol or bulk solution, as a control experiment. Dimethylamine, DMA, has been observed as a significant component of particles and cloud water.[42,43] Given that the pK_a of DMA is ca. 10.7, it is expected to exist almost exclusively as DMAH in atmospheric aerosols.[9] We aerosolized a 2 m DMA/DMAH solution with an initial pH of 10.6, corresponding to slightly more DMAH than DMA in the initial solution. By comparison to the bulk spectrum of this mixture, it can be seen that DMAH but not DMA is present in the aerosol. We infer that DMA partitioned away during the nebulization process, leaving only DMAH in the aerosol phase. Over 110 minutes, the DMAH signal does not significantly change, indicating that this ion does not partition into the gas phase, nor does transient DMA (from the dynamic equilibrium of DMAH with DMA) escape at a fast enough rate to slowly deplete the aerosol of DMAH. Our finding is therefore consistent with the observation of DMAH in real atmospheres and cloud water.

5.4.2 Calculations

We have shown here that organic acids can partition from aerosols on fast timescales, often on the order of minutes, potentially contributing to multiphase buffering. To put this timescale in context, we calculated a theoretical rate of acidification for a 4-micron radius aqueous aerosol. We considered only ambient concentrations of the strong acids HCl at 1 ppb,[44] HNO_3 at 1 $\mu g/m^3$,[45] and H_2SO_4 at 10^6 molecules/cm^3.[46] We used a wind speed of 15 km/hr, just above the minimum associated with the formation of waves and hence e.g. sea spray aerosols.[47] This allowed the calculation of the number of acidic molecules the aerosol would collide with as it travels through a volume equal to the cylinder swept out by its area. Assuming no buffering, this creates an aerosol at pH 4.4 in 1 second and pH 2.3 in 2 minutes. This means that acidification can be slow enough that the evaporation of newly-protonated organic acids from aerosols can help buffer pH. Of

course, there may also be neutralization by bases such as ammonia, which ranges in concentration from < 0.2 to > 24 ppbv.[48] Using a value of 1.1 ppbv and assuming instant neutralization, we calculated a 1 second pH of 5.7 and a 2 minute pH of 3.7. We assumed accommodation coefficients of unity for this calculation, but if smaller coefficients were used, which have been observed even for strong acids,[49] then acidification would be even slower and organic evaporation would have more time to occur.

To gain further insight into the behavior of molecules evaporating from confinement in aerosol micro-compartments, we performed calculations on the rate of diffusion of lactic acid molecules. A convenient mathematical result is that, in spherical coordinates when only radial diffusion needs consideration, the mathematics are the same as for a one-dimension system.[50] We calculated the diffusion coefficient by extrapolating literature measurements,[51] resulting in a value of 7.3 to 7.6 * 10^{-6} cm^2/s for the concentration range of 1 to 2 m lactic acid. We calculated that for a single-point concentration allowed to diffuse outward, in just 1 second, the concentration at a distance of 4 microns is only 0.5% different than that at the origin.[50] Therefore, mixing occurs on the millisecond timescale, and would only be slow enough to limit the evaporation rate at a very low mole fraction of water, with a particle composed essentially entirely of lactic acid.[52]

We also performed calculations with a system of 10^5 particles randomly distributed across a 4 micron 1-dimensional distance. At each time step, the movement of each particle was carried out by multiplying a diffusion rate by the cosine of a randomly generated number between 0 and 2 pi (see Data Package for the MATLAB code). Particles that passed into a negative x-coordinate were reflected to the absolute value of their current location, and particles that passed the 4 micron threshold were irreversibly removed from the system and designated as evaporated. Using the diffusion coefficient as the diffusion rate, we initially obtained a first-order evaporation rate of 20

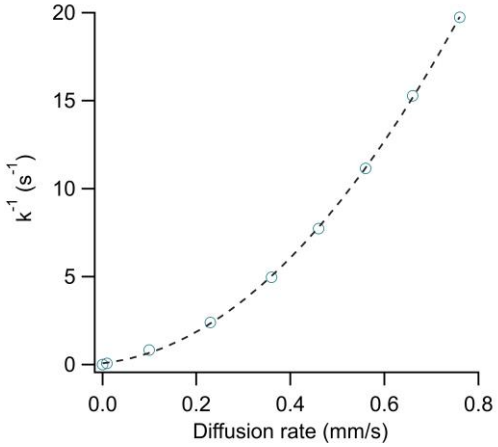

Figure 5.7: Sensitivity analysis for calculated evaporation rate constant at different diffusion rates. The top right data point corresponds to a rate equal to the diffusion coefficient with a 100% probability of escaping the aerosol upon arriving at the aerosol-air interface. Simulations were performed using 10^5 particles, as it was found that increasing the particles to 10^6 only changed *k* by 0.12% while greatly increasing computing cost. Data points fit $y = (30.3 \pm 0.6)x^2 + (2.8 \pm 0.5)x + (0.08 \pm 0.07)$ with $R^2 = 0.999$.

s^{-1}. For a real aerosol, as evaporation progresses, competing effects would start to impact the evaporation rate. Namely, evaporation rate would increase as the viscosity of the system decreased, but the evaporation rate would also decrease as the pH increased and a greater percentage of the lactic acid molecules became lactate. These effects are less important for our experiments, as we could only track lactic acid evaporation to the limit of quantitation, 0.36 m. At this point, for a system that started with 1.5 m lactic acid, the pH only would increase by 0.3 units and the percentage of lactic acid molecules in the form of lactate would only increase from 1.0 to 2.1%.

Based on a sensitivity analysis (Figure 5.7), the diffusion rate needs to be lower by a factor of ca. 50 in order to match our fastest experimental evaporation rate. This is partly due to the fact that real aerosols can have organic vapors condense back onto the aerosol. In addition, the energy barrier at the air-water interface must be overcome by the molecule before it evaporates, and thus this barrier reduces the probability of lactic acid exiting the aqueous phase. Mathematically this could be quantified by an evaporation coefficient (describing a decrease from the maximum

theoretical evaporation rate).[53] Calculations agree with experiments for an evaporation coefficient of 0.003, slightly below what is probable, indicating that salting-out or other factors contribute to accelerated evaporation.[54] The energy barrier itself is the enthalpy of vaporization (ΔH_v) which has been reported ranging from 58 to 69 kJ/mol for lactic acid.[55,56] Since a gas molecule always has a higher entropy in the gas phase compared to the condensed-phase, ΔH_v thermodynamically justifies why all aerosol components do not immediately become individual gases. Using a semi-empirical correlation, this ΔH_v value corresponds to a saturation concentration of $2.8 * 10^5$ μg/m^3, which follows from the fact that lactic acid is both volatile (b.p. = 122 °C) and miscible in water.[57,58]

To highlight the importance of enhanced partitioning, we next compared our experimental findings to predictions from E-AIM Model III.[59–61] We used the ratio of moles from each bulk solution and an RH of 80%. Lactic acid was input as a singly dissociating acid using a pK_a of 3.86 and a Henry's Law constant of $7.1 * 10^7$ mol/(kg*atm).[62,63] For our systems, E-AIM predicted (molality-based) pH values ranging from 1.43 to 1.71. This is striking, given that this is an equilibrium model, and our data indicates that the majority of lactic acid partitions away by the time the aerosol reaches equilibrium. Even assuming no further lactic acid evaporates past our limit of detection (which is unlikely), the aerosol pH would be at least as high as 2.4 and could theoretically even be neutral. The situation is similar for methacrylic acid, with an E-AIM predicted pH of 2.5 and a minimum experimental pH of 2.8. This demonstrates that thermodynamic models can underestimate pH when Henry's Law and volatility are both high. While E-AIM is likely predicting a pH close to what would be observed in a bulk solution with the majority of lactic acid remaining in the aqueous phase, we have found that lactic acid can be efficiently salted out of aerosols and therefore is primarily present in the gas phase. Thus, care

should be taken when assessing the final composition of aerosols with large fractions of volatile components. Indeed, while equilibrium partitioning may describe the formation of organic-containing aerosols well, the properties of the formed aerosol can be quite different from equilibrium predictions.[64]

5.5 Conclusions and Implications

We have shown that small organic acids evaporate rapidly from aqueous salt aerosols in conditions of low gas phase concentrations over timescales ranging from milliseconds to minutes depending on the specific organic acid. Evaporation rate can be slowed by increases in viscosity but, despite the fact that increases in NaCl increase viscosity, evaporation rate is accelerated by NaCl due to salting-out effects. Given the lifetime of typical atmospheric particles, small organic acids leave very quickly.[65] This illustrates the possibility of a distinct type of titration that can occur for aqueous aerosols. In a typical aqueous solution bulk-phase titration of a conjugate base, as acid is added, the pH decreases and the organic fraction remains constant. For an aerosol composed of conjugate base, however, the pH actually remains constant as the organic fraction decreases since the organic acid partitions rapidly into the gas phase. The released organic acids could then react with atmospheric amines to form secondary organic aerosols.[43]

Using our data, we can categorize the lifetime of an aerosol based on its pH. Using sea spray aerosols as an example, these particles are rapidly acidified to pH 2-4 within minutes.[11,12] At this point, the aerosol pH drops below the pK_a value of many organic acids and their volatilization causes multiphase buffering, preventing the aerosol pH from dropping further. Buffering from nonvolatile species such as charged amino acids may help maintain the aerosol pH of ca. 2.[66,67] This can explain how both fresh and aged sea spray aerosols have similar pH levels. Neutralization by ammonia may also occur, although depending on the aerosol liquid water content, due to

partitioning, the peak buffering capacity of the ammonia/ammonium system may be at an acidic pH.[18] Over many days, the multiphase buffering capacity may eventually be exhausted, allowing aerosols to equilibrate with strong acids in the atmosphere and reach pH < 0.[9] Thus, for areas producing aerosols with a high fraction of small organic acid molecules, the pH can be expected to remain near the average pK_a of these acids for most of the aerosol's lifetime since organic partitioning is so fast that the process will rarely be kinetically limited. For aerosols with a low fraction of these organic acids or their conjugate bases, the particle will more quickly drop to a very acidic pH and have more harmful effects on human health.

Our findings give some additional insights into experimental methods that utilize small organic molecules. Some mass spectrometry and liquid jet methods rely on organics as solvents for analytes.[68] The fast evaporation of these organics, and the resulting concentration of the analytes, should be accounted for when considering the data. Recently, the phenomenon of reaction acceleration in the aerosol phase has been a topic of considerable interest.[68,69] We have shown that organic acids can evaporate from aqueous salt aerosols faster than would be predicted from a S:V or viscosity analysis alone, with salting-out likely contributing to this enhancement. Therefore, salting-out effects should be quantified when comparing reaction rates in aerosols or liquid jets to bulk solutions.

5.6 Acknowledgements

Chapter 5, in part, contains original research that will has been submitted for publication to Environmental Science: Atmospheres in: Angle, Kyle; Nowak, Christopher; Grassian, Vicki, Organic Acid Evaporation Kinetics From Aqueous Aerosols: Implications for Aerosol Buffering Capacity in the Atmosphere in 2022. The dissertation author was the primary investigator and author of this paper.

This work was supported by the National Science Foundation (Grant CHE-1801971). The authors thank Dr. Gil Nathanson and Mariana Rivas for helpful discussions, and Alexis Wright and Justin Wang for assistance with sample preparation and measurements. The authors thank Paul Smith (Biral, Inc.) for assistance with the AOT.

5.7 References

(1) Luo, M.; Wauer, N. A.; Angle, K. J.; Dommer, A. C.; Song, M.; Nowak, C. M.; Amaro, R. E.; Grassian, V. H. Insights into the Behavior of Nonanoic Acid and Its Conjugate Base at the Air/Water Interface through a Combined Experimental and Theoretical Approach. *Chem. Sci.* **2020**, *11* (39), 10647–10656.

(2) Angle, K. J.; Nowak, C. M.; Davasam, A.; Dommer, A. C.; Wauer, N. A.; Amaro, R. E.; Grassian, V. H. Amino Acids Are Driven to the Interface by Salts and Acidic Environments. *J. Phys. Chem. Lett.* **2022**, *13* (12), 2824–2829.

(3) Hung, H. M.; Hsu, M. N.; Hoffmann, M. R. Quantification of SO_2 Oxidation on Interfacial Surfaces of Acidic Micro-Droplets: Implication for Ambient Sulfate Formation. *Environ. Sci. Technol.* **2018**, *52* (16), 9079–9086.

(4) Angle, K. J.; Neal, E. E.; Grassian, V. H. Enhanced Rates of Transition-Metal-Ion-Catalyzed Oxidation of S(IV) in Aqueous Aerosols: Insights into Sulfate Aerosol Formation in the Atmosphere. *Environ. Sci. Technol.* **2021**, *55* (15), 10291–10299.

(5) Farmer, D. K.; Cappa, C. D.; Kreidenweis, S. M. Atmospheric Processes and Their Controlling Influence on Cloud Condensation Nuclei Activity. *Chem. Rev.* **2015**, *115* (10), 4199–4217.

(6) Duan, J.; Lyu, R.; Wang, Y.; Xie, X.; Wu, Y.; Tao, J.; Cheng, T.; Liu, Y.; Peng, Y.; Zhang, R.; He, Q.; Ga, W.; Zhang, X.; Zhang, Q. Particle Liquid Water Content and Aerosol Acidity Acting as Indicators of Aerosol Activation Changes in Cloud Condensation Nuclei (CCN) during Pollution Eruption in Guangzhou of South China. *Aerosol Air Qual. Res.* **2019**, *19*, 2662–2670.

(7) Kim, K. H.; Kabir, E.; Kabir, S. A Review on the Human Health Impact of Airborne Particulate Matter. *Environ. Int.* **2015**, *74*, 136–143.

(8) De Gouw, J.; Jimenez, J. L. Organic Aerosols in the Earth's Atmosphere. *Environ. Sci. Technol.* **2009**, *43* (20), 7614–7618.

(9) Pye, H. O. T.; Nenes, A.; Alexander, B.; Ault, A. P.; Barth, M. C.; Clegg, S. L.; Collett, J. L.; Fahey, K. M.; Hennigan, C. J.; Herrmann, H.; Kanakidou, M.; Kelly, J. T.; Ku, I.-T.; Mcneill, V. F.; Riemer, N.; Schaefer, T.; Shi, G.; Tilgner, A.; Walker, J. T.; Wang, T.; Weber, R.; Xing, J.; Zaveri, R. A.; Zuend, A. The Acidity of Atmospheric Particles and

Clouds. *Atmos. Chem. Phys.* **2020**, *20*, 4809–4888.

(10) Hennigan, C. J.; Izumi, J.; Sullivan, A. P.; Weber, R. J.; Nenes, A. A Critical Evaluation of Proxy Methods Used to Estimate the Acidity of Atmospheric Particles. *Atmos. Chem. Phys.* **2015**, *15* (5), 2775–2790.

(11) Angle, K. J.; Crocker, D. R.; Simpson, R. M. C.; Mayer, K. J.; Garofalo, L. A.; Moore, A. N.; Mora Garcia, S. L.; Or, V. W.; Srinivasan, S.; Farhan, M.; Sauer, J. S.; Lee, C.; Pothier, M. A.; Farmer, D. K.; Martz, T. R.; Bertram, T. H.; Cappa, C. D.; Prather, K. A.; Grassian, V. H. Acidity across the Interface from the Ocean Surface to Sea Spray Aerosol. *Proc. Natl. Acad. Sci.* **2020**, *118* (2), e2018397118.

(12) Fridlind, A. M.; Jacobson, M. Z. A Study of Gas-Aerosol Equilibrium and Aerosol pH in the Remote Marine Boundary Layer during the First Aerosol Characterization Experiment (ACE 1). *J. Geophys. Res. Atmos.* **2000**, *105* (D13), 17325–17340.

(13) Mircea, M.; Facchini, M. C.; Decesari, S.; Cavalli, F.; Emblico, L.; Fuzzi, S.; Vestin, A.; Rissler, J.; Swietlicki, E.; Frank, G.; Andreae, M. O.; Maenhaut, W.; Rudich, Y.; Artaxo, P. Importance of the Organic Aerosol Fraction for Modeling Aerosol Hygroscopic Growth and Activation: A Case Study in the Amazon Basin. *Atmos. Chem. Phys.* **2005**, *5* (11), 3111–3126.

(14) Schmedding, R.; Rasool, Q. Z.; Zhang, Y.; Pye, H. O. T.; Zhang, H.; Chen, Y.; Surratt, J. D.; Lopez-Hilfiker, F. D.; Thornton, J. A.; Goldstein, A. H.; Vizuete, W. Predicting Secondary Organic Aerosol Phase State and Viscosity and Its Effect on Multiphase Chemistry in a Regional-Scale Air Quality Model. *Atmos. Chem. Phys.* **2020**, *20* (13), 8201–8225.

(15) Zhang, Q.; Jimenez, J. L.; Canagaratna, M. R.; Ulbrich, I. M.; Ng, N. L.; Worsnop, D. R.; Sun, Y. Understanding Atmospheric Organic Aerosols via Factor Analysis of Aerosol Mass Spectrometry: A Review. *Anal. Bioanal. Chem.* **2011**, *401* (10), 3045–3067.

(16) Meng, Z.; Seinfeld, J. H.; Saxena, P. Gas/Aerosol Distribution of Formic and Acetic Acids. *Aerosol Sci. Technol.* **1995**, *23* (4), 561–578.

(17) Paulot, F.; Wunch, D.; Crounse, J. D.; Toon, G. C.; Millet, D. B.; Decarlo, P. F.; Vigouroux, C.; Deutscher, N. M.; Abad, G. G.; Notholt, J.; Warneke, T.; Hannigan, J. W.; Warneke, C.; De Gouw, J. A.; Dunlea, E. J.; De Mazière, M.; Griffith, D. W. T.; Bernath, P.; Jimenez, J. L.; Wennberg, P. O. Importance of Secondary Sources in the Atmospheric Budgets of Formic and Acetic Acids. *Atmos. Chem. Phys.* **2011**, *11* (5), 1989–2013.

(18) Zheng, G.; Su, H.; Wang, S.; Andreae, M. O.; Pöschl, U.; Cheng, Y. Multiphase Buffer Theory Explains Contrasts in Atmospheric Aerosol Acidity. *Science* **2020**, *369* (6509), 1374–1377.

(19) Li, L.-F.; Chen, Z.; Liu, P.; Zhang, Y.-H. Direct Measurement of pH Evolution in Aerosol Microdroplets Undergoing Ammonium Depletion: A Surface-Enhanced Raman Spectroscopy Approach. *Environ. Sci. Technol.* **2022**.

(20) Kohli, R. K.; Davies, J. F. Measuring the Chemical Evolution of Levitated Particles: A Study on the Evaporation of Multicomponent Organic Aerosol. *Anal. Chem.* **2021**, *93* (36), 12472–12479.

(21) McGloin, D.; Burnham, D. R.; Summers, M. D. Trapping Solid Aerosols with Optical Tweezers: A Comparison between Gas and Liquid Phase Optical Traps. *Opt. Express* **2008**, *16* (11), 7739–7747.

(22) Friedman, B.; Farmer, D. K. SOA and Gas Phase Organic Acid Yields from the Sequential Photooxidation of Seven Monoterpenes. *Atmos. Environ.* **2018**, *187*, 335–345.

(23) Wilson, J.; Imre, D.; Beránek, J.; Shrivastava, M.; Zelenyuk, A. Evaporation Kinetics of Laboratory-Generated Secondary Organic Aerosols at Elevated Relative Humidity. *Environ. Sci. Technol.* **2015**, *49* (1), 243–249.

(24) O'Meara, S.; Topping, D. O.; McFiggans, G. The Rate of Equilibration of Viscous Aerosol Particles. *Atmos. Chem. Phys.* **2016**, *16* (8), 5299–5313.

(25) Wallace, B. J.; Preston, T. C. Water Uptake and Loss in Viscous Aerosol Particles with Concentration-Dependent Diffusivities. *J. Phys. Chem. A* **2019**, *123* (15), 3374–3382.

(26) Rafferty, A.; Gorkowski, K.; Zuend, A.; Preston, T. C. Optical Deformation of Single Aerosol Particles. *Proc. Natl. Acad. Sci. U. S. A.* **2019**, *116* (40), 19880–19886.

(27) Coddens, E. M.; Angle, K. J.; Grassian, V. H. Titration of Aerosol pH through Droplet Coalescence. *J. Phys. Chem. Lett.* **2019**, *10* (15), 4476–4483.

(28) Cotterell, M. I.; Willoughby, R. E.; Bzdek, B. R.; Orr-Ewing, A. J.; Reid, J. P. A Complete Parameterisation of the Relative Humidity and Wavelength Dependence of the Refractive Index of Hygroscopic Inorganic Aerosol Particles. *Atmos. Chem. Phys* **2017**, *17*, 9837–9851.

(29) Cassanas, G.; Morssli, M.; Fabrègue, E.; Bardet, L. Vibrational Spectra of Lactic Acid and Lactates. *J. Raman Spectrosc.* **1991**, *22* (7), 409–413.

(30) Galeazzo, T.; Valorso, R.; Li, Y.; Camredon, M.; Aumont, B.; Shiraiwa, M. Estimation of Secondary Organic Aerosol Viscosity from Explicit Modeling of Gas-Phase Oxidation of Isoprene and α-Pinene. *Atmos. Chem. Phys.* **2021**, *21* (13), 10199–10213.

(31) Ushijima, S. B.; Huynh, E.; Davis, R. D.; Tolbert, M. A. Seeded Crystal Growth of Internally Mixed Organic-Inorganic Aerosols: Impact of Organic Phase State. *J. Phys. Chem. A* **2021**, *125* (39), 8668–8679.

(32) Tumminello, P. R.; James, R. C.; Kruse, S.; Kawasaki, A.; Cooper, A.; Guadalupe-Diaz, I.; Zepeda, K. L.; Crocker, D. R.; Mayer, K. J.; Sauer, J. S.; Lee, C.; Prather, K. A.; Slade, J. H. Evolution of Sea Spray Aerosol Particle Phase State across a Phytoplankton Bloom. *ACS Earth Sp. Chem.* **2021**, *5* (11), 2995–3007.

(33) Kampf, C. J.; Waxman, E. M.; Slowik, J. G.; Dommen, J.; Pfaffenberger, L.; Praplan, A. P.; Prévoît, A. S. H.; Baltensperger, U.; Hoffmann, T.; Volkamer, R. Effective Henry's Law Partitioning and the Salting Constant of Glyoxal in Aerosols Containing Sulfate. *Environ. Sci. Technol.* **2013**, *47* (9), 4236–4244.

(34) Werner, J.; Dalirian, M.; Walz, M. M.; Ekholm, V.; Wideqvist, U.; Lowe, S. J.; Öhrwall, G.; Persson, I.; Riipinen, I.; Björneholm, O. Surface Partitioning in Organic-Inorganic Mixtures Contributes to the Size-Dependence of the Phase-State of Atmospheric Nanoparticles. *Environ. Sci. Technol.* **2016**, *50* (14), 7434–7442.

(35) Shah, D. J.; Tlwari, K. K. Effect of Salt on the Distribution of Acetic Acid between Water and Organic Solvent. *J. Chem. Eng. Data* **1981**, *26*, 57.

(36) Häkkinen, S. A. K.; McNeill, V. F.; Riipinen, I. Effect of Inorganic Salts on the Volatility of Organic Acids. *Environ. Sci. Technol.* **2014**, *48* (23), 13718–13726.

(37) Sander, R. Compilation of Henry's Law Constants (Version 4.0) for Water as Solvent. *Atmos. Chem. Phys* **2015**, *15*, 4399–4981.

(38) Kestin, J.; Khalifa, H. E.; Correia, R. J. Tables of the Dynamic and Kinematic Viscosity of Aqueous NaCl Solutions in the Temperature Range 20-150 °C and the Pressure Range 0.1-35 MPa. *J. Phys. Chem. Ref. Data* **1981**, *10*, 71.

(39) Troupe, R. A.; Aspy, W. L.; Schrodt, P. R. Viscosity and Density of Aqueous Lactic Acid Solutions. *Ind. Eng. Chem.* **1951**, *43* (5), 1143–1146.

(40) Reggente, M.; Dillner, A. M.; Takahama, S. Analysis of Functional Groups in Atmospheric Aerosols by Infrared Spectroscopy: Systematic Intercomparison of Calibration Methods for US Measurement Network Samples. *Atmos. Meas. Tech.* **2019**, *12* (4), 2287–2312.

(41) Lv, S.; Wang, F.; Wu, C.; Chen, Y.; Liu, S.; Zhang, S.; Li, D.; Du, W.; Zhang, F.; Wang, H.; Huang, C.; Fu, Q.; Duan, Y.; Wang, G. Gas-to-Aerosol Phase Partitioning of Atmospheric Water-Soluble Organic Compounds at a Rural Site in China: An Enhancing Effect of NH3 on SOA Formation. *Environ. Sci. Technol.* **2022**, *56* (7), 3915–3924.

(42) Youn, J. S.; Crosbie, E.; Maudlin, L. C.; Wang, Z.; Sorooshian, A. Dimethylamine as a Major Alkyl Amine Species in Particles and Cloud Water: Observations in Semi-Arid and Coastal Regions. *Atmos. Environ.* **2015**, *122*, 250–258.

(43) Yin, R.; Yan, C.; Cai, R.; Li, X.; Shen, J.; Lu, Y.; Schobesberger, S.; Fu, Y.; Deng, C.; Wang, L.; Liu, Y.; Zheng, J.; Xie, H.; Bianchi, F.; Worsnop, D. R.; Kulmala, M.; Jiang, J. Acid-Base Clusters during Atmospheric New Particle Formation in Urban Beijing. *Environ. Sci. Technol.* **2021**, *55* (16), 10994–11005.

(44) Brimblecombe, P. *Air Composition and Chemistry*; Cambridge University Press: Cambridge, 1996.

(45) Lindqvist, F. Determination of Nitric Acid in Ambient Air by Gas

Chromatography/Photoionization Detection after Collection in a Denuder. *J. Air Pollut. Control Assoc.* **1985**, *35* (1), 19–23.

(46) Beck, L. J.; Schobesberger, S.; Sipilä, M.; Kerminen, V.-M.; Kulmala, M. Estimation of Sulfuric Acid Concentration Using Ambient Ion Composition and Concentration Data Obtained with Atmospheric Pressure Interface Time-of-Flight Ion Mass Spectrometer. *Atmos. Meas. Tech* **1957**, *15*.

(47) Pant, V.; Deshpande, C. G.; Kamra, A. K. On the Aerosol Number Concentration–Wind Speed Relationship during a Severe Cyclonic Storm over South Indian Ocean. *J. Geophys. Res. Atmos.* **2008**, *113* (D2), 2206.

(48) Nair, A. A.; Yu, F. Quantification of Atmospheric Ammonia Concentrations: A Review of Its Measurement and Modeling. *Atmos. 2020, Vol. 11, Page 1092* **2020**, *11* (10), 1092.

(49) Li, M.; Su, H.; Li, G.; Ma, N.; Pöschl, U.; Cheng, Y. Relative Importance of Gas Uptake on Aerosol and Ground Surfaces Characterized by Equivalent Uptake Coefficients. *Atmos. Chem. Phys* **2019**, *19*, 10981–11011.

(50) Crank, J. *The Mathematics of Diffusion*, 2nd ed.; Clarendon Press, Oxford, 1975.

(51) Ribeiro, A. C. F.; Lobo, V. M. M.; Leaist, D. G.; Natividade, J. J. S.; Veríssimo, L. P.; Barros, M. C. F.; Cabral, A. M. T. D. P. V. Binary Diffusion Coefficients for Aqueous Solutions of Lactic Acid. *J. Solut. Chem. 2005 349* **2005**, *34* (9), 1009–1016.

(52) Booth, A. M.; Murphy, B.; Riipinen, I.; Percival, C. J.; Topping, D. O. Connecting Bulk Viscosity Measurements to Kinetic Limitations on Attaining Equilibrium for a Model Aerosol Composition. *Environ. Sci. Technol.* **2014**, *48* (16), 9298–9305.

(53) Julin, J.; Winkler, P. M.; Donahue, N. M.; Wagner, P. E.; Riipinen, I. Near-Unity Mass Accommodation Coefficient of Organic Molecules of Varying Structure. *Environ. Sci. Technol.* **2014**, *48* (20), 12083–12089.

(54) Saleh, R.; Shihadeh, A.; Khlystov, A. Determination of Evaporation Coefficients of Semi-Volatile Organic Aerosols Using an Integrated Volume-Tandem Differential Mobility Analysis (IV-TDMA) Method. *J. Aerosol Sci.* **2009**, *40* (12), 1019–1029.

(55) Emel'yanenko, V. N.; Verevkin, S. P.; Schick, C.; Stepurko, E. N.; Roganov, G. N.; Georgieva, M. K. The Thermodynamic Properties of S-Lactic Acid. *Russ. J. Phys. Chem. A 2010 849* **2010**, *84* (9), 1491–1497.

(56) Yaws, C. L. Physical, Thermodynamic and Transport Properties for 5,000 Organic Chemical Compounds. In *Yaws' handbook of thermodynamic and physical properties of chemical compounds*; Knovel: New York, 2003.

(57) Epstein, S. A.; Riipinen, I.; Donahue, N. M. A Semiempirical Correlation between Enthalpy of Vaporization and Saturation Concentration for Organic Aerosol. *Environ. Sci. Technol.* **2010**, *44* (2), 743–748.

(58) Lactic Acid. GESTIS-Stoffdatenbank https://gestis.dguv.de/data?name=013000&lang=en (accessed May 27, 2022).

(59) Wexler, A. S.; Clegg, S. L. Atmospheric Aerosol Models for Systems Including the Ions H^+, NH_4^+, Na^+, SO_4^{2-}, NO_3^-, Cl^-, Br^-, and H_2O. *J. Geophys. Res. Atmos.* **2002**, *107* (14), ACH 14-1.

(60) Clegg, S. L.; Pitzer, K. S.; Brimblecombe, P. Thermodynamics of Multicomponent, Miscible, Ionic Solutions. 2. Mixtures Including Unsymmetrical Electrolytes. *J. Phys. Chem.* **1992**, *96* (23), 9470–9479.

(61) Clegg, S. L.; Brimblecombe, P.; Wexler, A. S. Thermodynamic Model of the System H^+-NH_4^+-Na^+-SO_4^{2-}-NO_3^--Cl^--H_2O at 298.15 K. *J. Phys. Chem. A* **1998**, *102* (12), 2155–2171.

(62) National Center for Biotechnology Information: PubChem Annotation Record for Lactic Acid https://pubchem.ncbi.nlm.nih.gov/source/hsdb/800 (accessed May 26, 2022).

(63) Dawson, R. M. C.; Elliott, D. C.; Elliott, W. H.; Jones, K. M. *Data for Biochemical Research*, 3rd ed.; Clarendon Press: Oxford, 1989.

(64) Cappa, C. D.; Wilson, K. R. Evolution of Organic Aerosol Mass Spectra upon Heating: Implications for OA Phase and Partitioning Behavior. *Atmos. Chem. Phys.* **2011**, *11* (5), 1895–1911.

(65) Haszpra, T. Intricate Features in the Lifetime and Deposition of Atmospheric Aerosol Particles. *Chaos An Interdiscip. J. Nonlinear Sci.* **2019**, *29* (7), 071103.

(66) Bertram, T. H.; Cochran, R. E.; Grassian, V. H.; Stone, E. A. Sea Spray Aerosol Chemical Composition: Elemental and Molecular Mimics for Laboratory Studies of Heterogeneous and Multiphase Reactions. *Chem. Soc. Rev.* **2018**, *47* (7), 2374–2400.

(67) Barbaro, E.; Zangrando, R.; Moret, I.; Barbante, C.; Cescon, P.; Gambaro, A. Free Amino Acids in Atmospheric Particulate Matter of Venice, Italy. *Atmos. Environ.* **2011**, *45* (28), 5050–5057.

(68) Wei, Z.; Li, Y.; Cooks, R. G.; Yan, X. Accelerated Reaction Kinetics in Microdroplets: Overview and Recent Developments. *Annu. Rev. Phys. Chem.* **2020**, *71* (1), 31–51.

(69) Rovelli, G.; Jacobs, M. I.; Willis, M.; Rapf, R. J.; Prophet, A. M.; Wilson, K. R. A Critical Analysis of Electrospray Techniques for the Determination of Accelerated Rates and Mechanisms of Chemical Reactions in Droplets. *Chem. Sci.* **2020**, *11* (48), 13026.

CHAPTER 6 DIRECT QUANTIFICATION OF NITRATE AND CHLORIDE DEPLETION KINETICS FROM SINGLE LEVITATED AEROSOLS

6.1 Abstract

The hygroscopicity and pH of aerosols control their impacts on human health and the climate. Nitrate and chloride depletion are processes that appear to be unique to the aerosol phase and influence both hygroscopicity and pH. Despite many field observations and laboratory tests, uncertainties remain about these processes. While acid evaporation has been observed during dehydration there is a question as to the rate of acid evaporation and whether this occurs in fully hydrated particles. Here, we analyze Raman spectra from single, levitated aerosols to directly elucidate the kinetics of nitrate and chloride depletion. Using glycine as a novel in-situ pH probe, we are able to measure nitrate and chloride depletion over timescales of hours in fully hydrated particles at 80% RH. We find, in agreement with previous studies, that chloride depletion is faster than nitrate depletion. In addition, from the calculated rate constants, we infer depletion is limited by the formation of HCl/HNO_3 at the air-water interface.

6.2 Introduction

Aerosols are ubiquitous in the atmosphere and have profound effects on global climate and human health. The chemical content of an aerosol, including organic fraction and salts such as nitrates and sulfates, determine its hygroscopicity, which in turn controls aerosol size.[1,2] Another parameter, aerosol acidity, can influence cloud condensation nucleus activity, aerosol surface chemistry, and particle interactions with the lungs.[3–5] Aerosol pH and chemical composition are both sensitive to multiphase buffering, as acids and bases can partition out of aerosol into the surrounding environment.[6]

Two particular types of acid evaporation that are highly important to aerosol pH are nitrate and chloride depletion, which are shown in Equations 6.1 through 6.4.

$$HA\,(aq) + NO_3^-(aq) \rightarrow HNO_3(aq) + A^-\,(aq) \quad (6.1)$$

$$HA\,(aq) + Cl^-(aq) \rightarrow HCl\,(aq) + A^-(aq) \quad (6.2)$$

$$HNO_3(aq) \rightarrow HNO_3(g) \quad (6.3)$$

$$HCl\,(aq) \rightarrow HCl\,(g) \quad (6.4)$$

In the first two reactions, *HA* is generally used to refer to other acid molecules, often organic acids. These processes, hereafter termed "depletion", are typically not thermodynamically favorable in bulk solutions since HNO_3 and HCl are strong acids. However, both of these acids are highly volatile, and therefore likely to partition into the surrounding atmosphere once formed if they are able to access the solution-air interface. While the equilibria of Equations 6.3 and 6.4 are controlled by Henry's Law, the kinetics of aerosol and acid evaporation can vary substantially depending on factors such as concentration.[7]

Depletion has been observed in various field and laboratory studies, and occurs to a great enough extent to impact hygroscopicity and source apportionment considerations.[2,8–11] Several aspects of the depletion process remain unclear. Since HNO_3 or HCl must form at or diffuse to the surface in order to partition into the atmosphere, one might assume that depletion would be greater for smaller aerosols with higher surface area to volume ratios. Indeed, differences in depletion between fine and coarse aerosols have been observed.[12] Two reports from the Laskin group, however, have shown no statistically-significant size-dependence for substrate-deposited aerosols.[13,14] While most studies have focused on aerosols, there has also been observation of larger rainwater droplets containing less chloride than corresponding bulk solutions.[15] One important consideration for the size-dependence of depletion is that depletion can create a negative

feedback loop. As depletion occurs, aerosol pH is increased and fewer nitrate or chloride ions remain in the aerosol, presumably decreasing the probability of further HNO_3 or HCl from forming. Therefore, the extent of depletion observed in field studies may vary depending on the initial amount of nitrate or chloride salts contained in the particle, which would vary with aerosol size. Further, organic coatings on aerosols could inhibit depletion, preventing complete depletion from occurring even for long atmospheric lifetimes.[11,16] Detailed studies on the kinetics of depletion could resolve complications relating to size-dependence.

An additional area of ongoing investigation is the cause of depletion. In some studies, depletion is attributed to inorganic acids such as sulfuric acid (i.e. chloride or nitrate are replaced by sulfate).[17] Other reports have indicated that dicarboxylic acids can account for a significant fraction of depletion.[18,19] Acetic acid, by contrast, has been associated with little depletion.[9] Another mechanism involves joint loss with ammonia.[20] A further complication is that chloride depletion can be caused by other chemical reactions including reactions with ozone and the OH radical.[21] In general, atmospheric aerosols contain numerous components, making identification of the drivers of depletion challenging. For field studies, coalescence and agglutination of droplets adds yet another degree of complexity to tracking chloride or nitrate depletion.[8] For laboratory-generated aerosols that are deposited for days before analysis, the volatilization of aerosol components or the action of dehydration could convolute the analysis of the same processes.

To provide insight on nitrate and chloride depletion, we performed experiments with optically levitated single aerosols. The absence of a substrate allows HNO_3 or HCl to escape from any portion of the full surface area of the aerosol, more environmentally realistic in contrast with substrate-deposited aerosols. The technique we used also allows monitoring of aerosol size and relative humidity. Most importantly, we are able to obtain Raman spectra every second, giving

insights into the kinetics of depletion from an aerosol over time on seconds to hours timescales. By comparing our results to past studies and theoretical considerations, we highlight several key aspects necessary for depletion to occur and illustrate a method for future investigations of depletion.

6.3 Methods

All samples were created using milliQ water with resistivity > 18.1 MΩ. Sodium chloride and sodium sulfate were baked at 200 °C in an oven for at least 48 hours to help remove organic impurities. Glycine (> 98.5%) and sodium nitrate (> 99.0%) were used without additional purification. Adjustments to pH were made with concentrated sulfuric acid, and the pH of bulk solutions was measured with a pH meter (OAKTON Instruments).

A commercial Aerosol Optical Tweezers 100 (Biral Inc.) was used as previously described.[22] Briefly, samples were aerosolized by an ultrasonic nebulizer (MicroAIR U22, OMRON) resulting in aerosols ca. 3.5 ± 1 microns in radius. We note that this aerosol distribution contains particles with a variety of concentrations, probably due to the action of the vibrating mesh and water loss between particle generation and laser trapping. The trapping laser had a wavelength of 532 nm and was operated at 50 mW. Relative humidity (RH) was maintained at 80 ± 8% by controlled flow of wet and dry nitrogen gas (total flow 30 sccm). Raman spectra were acquired every second at 1200 g/millimeter setting, with the grating centered either at 570 nm to track the glycine, sulfate, and nitrate peaks, or at 645 nm to track size and refractive index. Each Raman peak location is reported as the same number between different experiments to minimize confusion; Raman maxima for a given experiment can shift by a few wavenumbers (± 4 cm^{-1}) due to differences in the chemical matrix. Bulk-phase refractive index measurements were performed

using an ABBE-3L refractometer (Bausch & Lomb) as described in Chapter 2 of this thesis, and the refractive indices of glycine solutions are given in Figure 6.5.

Calculations required parameters from the E-AIM model.[23,24] For these model runs, malonic acid was used in place of glycine. This is because these molecules have similar pK_{a1} values and calculations with glycine are not feasible. If glycine is input as an acid, the protonated form is uncharged and the deprotonated form is an anion, which makes correct ion balance impossible. If glycine is input as an amine, there are no significant issues from the viewpoint of charge balance, but the first pK_a of glycine falls outside the possible range of amine dissociation constants permissible by E-AIM. Other than this substitution, the E-AIM model is run with default settings.

6.4 Results and Analysis

6.4.1 Glycine as a Probe of Aerosol pH

Conjugate acid/base pairs can be used to monitor aerosol pH via Raman spectral peaks. Previously, Craig *et al.* employed various conjugate acid/base pairs for pH measurement in substrate-deposited aerosols.[25] Among the possibilities given at acidic pH were acetic acid, oxalic acid, bisulfate, and nitric acid itself. The nitric acid and nitrate conjugate pair should be avoided for long term pH measurements since the nitric acid can deplete over time. In past work, we have seen only weak, diffuse spectral signatures of bisulfate in our AOT spectra.[26] Oxalic acid generates significantly overlapping Raman peaks and has relatively poor solubility despite its small size.[25,27] Finally, acetic acid is highly volatile and likely to evaporate from aerosols.[28] To avoid these issues, we used glycine, an organic molecule with high solubility, distinct Raman peaks, and that would be charged in both its protonated and deprotonated forms so that it would not partition from the aerosol.

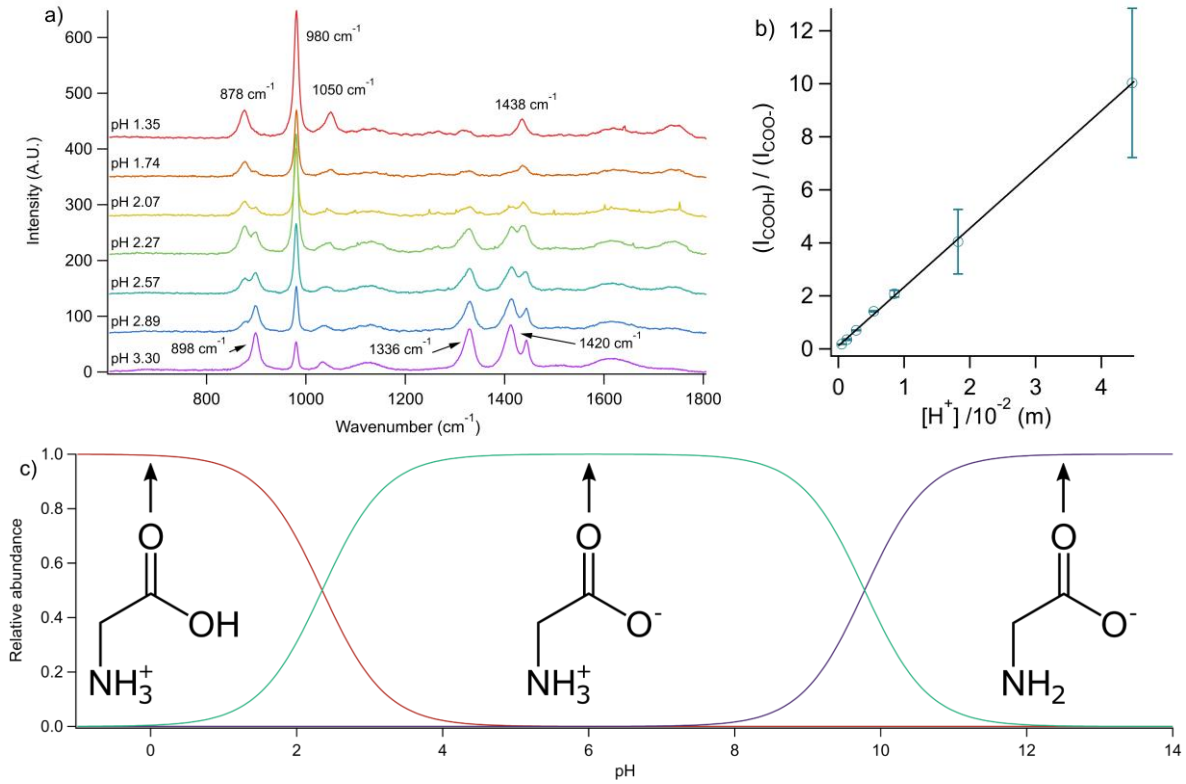

Figure 6.1: (a) Spectra of aerosols produced from bulk solutions of varying pH. Minimal acidification is expected upon nebulization as the solutions are already more acidic than CO_2, are buffered by 1 m glycine, and do not contain volatile acids. As pH increases, the C-COOH peak (878 cm^{-1}) decreases and the C-COO^- peak (898 cm^{-1}) increases. Bulk solutions were acidified by adding the appropriate amount of H_2SO_4, so the sulfate peak (980 cm^{-1}) is more intense at lower pH. Traces show the averages of 100 spectra each. (b) Calibration curve relating the peak intensity ratio of the C-C stretch for the protonated to deprotonated form, C-COOH to C-COO^-, to determine the aerosol H^+ concentration. (c) Speciation diagram of glycine showing the relative abundance of the cation (red), the zwitterion (teal), and the anion (blue).

We prepared an AOT calibration curve of glycine aerosols at various pH levels as shown in Figure 6.1. The annotated spectra list pH values corresponding to the bulk solutions from which the glycine aerosols were generated. We anticipate that these pH values are very similar to the pH of the aerosols as we have previously seen minimal acidification upon nebulization for acidic aerosols.[22] This is likely due to the fact that these aerosols are already at an acidic pH, eliminating titration by CO_2, and airborne for a short enough time for acidification by other trace gases to be

minimal. In addition, an increase in pH is often associated with the water loss that aerosols experience. Here, we maintained RH just above 85% to minimize water loss while still having a relative humidity reading with reasonable precision. Finally, although individual traces are shown, triplicate experiments were performed at each pH to verify the peak ratios were similar, with variability between aerosols shown in Figure 6.1b.

The spectra in Figure 6.1a show that the ratio of the 878 and 898 cm^{-1} peaks can be used to monitor aerosol acidity. These peaks correspond to the C-C stretch of the only two carbon atoms in glycine molecules, and due to the small size of glycine, the change in protonation state shifts the peak enough that they are reasonably well-resolved.[29] The appearance of the 1336 cm^{-1} (NH_3^+ and CH_2 twist) and 1420 cm^{-1} (NH_3^+ wag) peaks can independently give a qualitative indication of a pH increase, which is useful in the aerosol phase since WGMs can temporarily obscure the 878 and/or 898 cm^{-1} peaks. Figure 6.1b shows how the ratio of these peaks can be quantitatively converted to pH and was used for calculation of AOT aerosol acidity elsewhere in this chapter. Finally, Figure 6.1c shows a speciation diagram of glycine.

6.4.2 Analysis of Depletion from Single Aerosols via Raman Spectroscopy

With the pH-dependence of the glycine peaks as a direct probe of changes of pH within the aerosol, we now consider Raman spectra from single aerosols containing a mixture of nitrate, glycine, and sulfate (as an internal standard). The nitrate (NO_3^-) ion has a strong Raman signal at 1050 cm^{-1} assigned to the symmetric stretch, while sulfate (SO_4^{2-}) has a peak at ca. 980 cm^{-1} also assigned to the symmetric stretch. The sulfate peak is not expected to deplete over time, since it is in equilibrium with HSO_4^-, which is also charged. Sulfuric acid itself is highly acidic, more soluble, and is less volatile than HCl and HNO_3.[30] The sulfate peak could increase in intensity, however, if the starting pH were below 3 and pH increases, as bisulfate converts to sulfate. This pH increase

could come from nitrate depletion, which would lead to a decrease in the nitrate peak relative to the sulfate peak. We note that the loss of bisulfate in a bulk solution would lead to a decrease in intensity in the 1050 cm^{-1} region, however, for the AOT we have observed bisulfate signal to be weak and diffuse and therefore only a minor contributor to the overall peak area in that spectral region.[26]

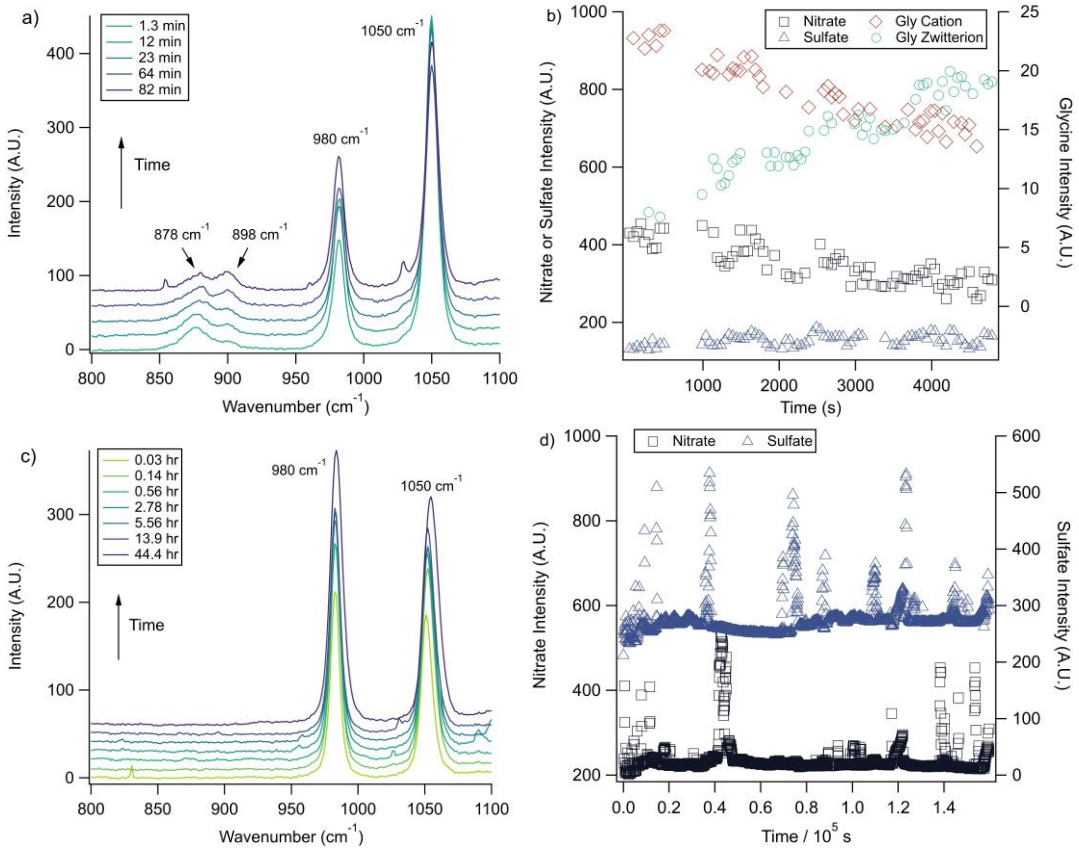

Figure 6.2: (a) An aerosol was trapped from a solution of 2 m glycine and 0.1 m $NaNO_3$ titrated to pH 1.8 with sulfuric acid. Spectra show via the glycine $COOH:COO^-$ ratio that the pH of the aerosol increases over time while the nitrate peak (1050 cm^{-1}) decreases. (b) Intensity values from this aerosol plotted over time. Note that separate y-axes are used to show the changes in the glycine (cation and zwitterion) peaks compared to the inorganic ion peaks. Error bars are omitted for visual clarity and are typically less than 10% of the data point value. (c) An aerosol was trapped from a solution of 1 m $NaNO_3$ and 1 m Na_2SO_4. The change in the nitrate peak area over time matched the change in the internal standard (sulfate), indicating no nitrate depletion occurred in this aerosol (acidity unadjusted). Traces show averages of 100 spectra each and are offset for clarity. (d) Intensity values for the aerosol in (c), with no net change for nitrate compared to sulfate over time. WGM data is included to show WGM relative intensity.

Sample spectra from a glycine, nitrate, and sulfate aerosol as a function of time are given in Figure 6.2a. A substantial pH change can be observed from the glycine peaks in just 82 minutes due to a pH change from ca. 1.6 to 2.4. In addition, the nitrate peak decreases by 33% while the sulfate peak increases by 9.4% (the intensities are plotted in Figure 6.2b). The change for the nitrate peak is expected to be smaller than the sulfate peak, since it has a substantially smaller concentration and therefore experiences a larger percent change from a given concentration change in molality units. To verify this pH change is due to nitrate depletion and not occurring due to dilution of the droplet by the surrounding RH flow, we trapped a separate aerosol composed only of sodium sulfate and sodium nitrate (pH unadjusted). For over 44 hours, the peaks did not change relative to each other as shown in Figure 6.2c and 6.2d. We note that the pH of the aerosol was not measured, so the lack of depletion may be due to the higher starting pH (likely close to the bulk solution value of 5.4). We also performed a nitrate depletion experiment with an aerosol containing only sulfate and nitrate generated from a bulk solution at pH 1.7, and this aerosol did exhibit nitrate depletion (see Figure 6.7). Therefore, we conclude that the total amount of acidity, rather than the presence of an organic acid, likely drives depletion. In general, either inorganic or organic acids can serve as *HA* in Equations 6.1 and 6.2, and future work with advanced aerosol pH measurement could target differences in depletion rate for organic-containing and organic-free aerosols at the same level of total acidity.

The nitrate depletion results demonstrate that either a Raman intensity directly corresponding to the species of interest (such as NO_3^-) or the pH of the aerosol can be used to measure depletion. The latter is convenient because the chloride ion cannot be detected with Raman spectroscopy. Therefore, the non-evaporating glycine pH indicator is used to track chloride depletion in individual aerosols. A sample result is given in Figure 6.3a. As before, the initially

acidic aerosol increases in pH over time as indicated by the glycine peak ratio. The process is also faster compared to nitrate depletion, so the spectra were averaged in smaller batches making the Whispering Gallery Modes (WGM's) are more apparent.

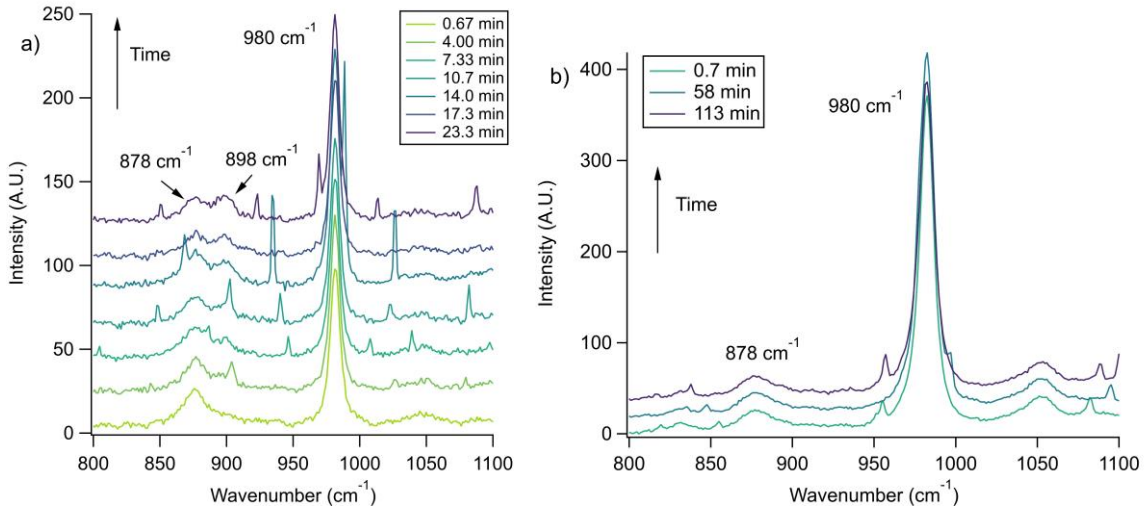

Figure 6.3: (a) An aerosol was trapped from a solution of 2 m glycine and 1 m NaCl titrated to pH 1.7 using H_2SO_4. The ratio of the COOH (878 cm^{-1}) and COO^- (898 cm^{-1}) peaks quickly changes, illustrating an increase in pH that corresponds to chloride depletion. The small, unmarked peaks are WGM's, characteristically identifiable by their changing locations in between spectra. Traces shown here are averages of 11 spectra each. (b) Control AOT experiment using an aerosol created from a 1 m glycine 2 m Na_2SO_4 bulk solution acidified to pH 2 with sulfuric acid. No pH increase was observed (no COO^- Gly peak grows in at 898 cm^{-1}) since no inorganic species depletes from the aerosol over time. Traces are offset for clarity, show averages of 120 spectra each, and small unmarked peaks correspond to WGM's.

Since we rely on the pH change shown by the glycine peaks to infer chloride depletion, it is important to verify that these changes do not occur due to other experimental factors. We tested this by trapping an aerosol containing only glycine and sodium sulfate, with Raman spectra shown in Figure 6.3b. No pH change is observed over ca. 2 hours, which is as expected since there is no chloride or nitrate available for depletion (initial aerosol pH was controlled with sulfuric acid). We note that no pH change is expected when RH is maintained constant as in the AOT; for substrate-deposited aerosols in environments of changing pH, the glycine peak ratio may be impacted by concentration or dilution even in the absence of depletion. To further demonstrate the utility of the

glycine peaks in measuring chloride depletion, we performed an experiment with an initially neutral aerosol, coalesced in HCl to lower the pH, and observed a return to a higher pH. The spectra are given in the Appendix in Figure 6.6.

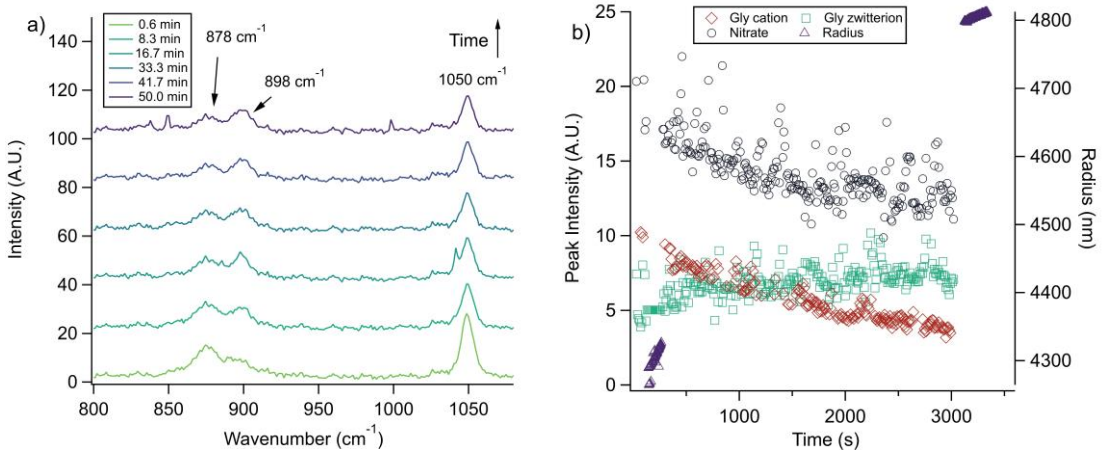

Figure 6.4: Results from an experiment at 80% RH with a growing aerosol. (a) Sample spectra show a decrease in the nitrate peak and a pH change is indicated by the glycine peak ratio. Traces show averages of 100 spectra each and are offset for clarity. (b) Scatter of peak area and radius data from the same experiment. The nitrate and cation glycine ($GlyH^+$) peak areas trend down over time, while the glycine peak (Gly) increases. Data near the beginning of the experiment indicate the aerosol started at a radius of ca. 4.3 μm and data at the end measure at ca. 4.8 μm. It is expected that the aerosol was increasing in size in between these sets of measurements due to the hygroscopicity of this particular particle.

These experiments were all carried out at 80% RH. Previous work on nitrate and chloride depletion has emphasized results for dehydrating aerosols.[31] Thermodynamically, depletion is driven by volatility and the partial pressure of HNO_3 or HCl in the surrounding environment, so there is not a strict theoretical requirement for dehydration.[32] Even so, multiple factors promote more depletion when there is dehydration. These include acidification of the aerosol, making the formation of HNO_3 or HCl more likely, as well as changes in gas phase properties such as the decreasing uptake coefficient of HNO_3 with increasing RH above 45% RH.[21] Given these considerations, we now highlight a contrasting example where depletion is observed even as the aerosol increases in size. Since radius data requires different grating settings, simultaneous radius

and nitrate peak data was not possible to obtain. Instead, we were able to size the aerosol early in the experiment, track nitrate depletion, and then size again at the end of the experiment. Results are shown in Figure 6.4. Nitrate depletion is clearly seen in the spectra and the peak intensity trends, which illustrate that this process can occur even for a particle that is not dehydrating and losing water.

A summary of AOT nitrate and chloride experiments is given in Table 6.1. After outliers corresponding to WGM's were removed (the impact of WGM's on intensity can be seen in Figure 6.2d), peak intensity over time was fit to first-order kinetics in order to obtain rate constants, *k*, as previously described.[22] The *k* values for chloride depletion are an order of magnitude larger than those of nitrate depletion. This is consistent with previous attributions of chloride depletion to nitric acid.[33] In addition, HCl is smaller than HNO_3, so once transient HCl is formed, it may be able to translate more quickly to the interface and evaporate before dissociating again. Finally, there is evidence that Cl^- is enriched at the interface of aerosols compared to the core, which would also make transient formation of HCl more likely.[34] A larger absolute uncertainty in the *k* values for chloride depletion comes in part from the fact that two glycine peaks, which exhibit overlap, must both be fit precisely to correctly track pH and calculate a rate, with each additional step adding to propagated error (see Appendix section 6.7.2).[35]

Table 6.1: Summary of single aerosol depletion experiments and first-order rate constants *k*.

Experiment type	# trials	k (s^{-1})	Chemicals present [Initial pH]
NO_3^- depletion (with glycine)	5	$1.3 \pm 0.4 * 10^{-4}$	$NaNO_3$, Gly, Na_2SO_4 [1.3-1.7]
NO_3^- depletion (no glycine)	1	$1.9 \pm 0.1 * 10^{-4}$	$NaNO_3$, Na_2SO_4 [1.7*]
Cl^- depletion	3	$1.0 \pm 0.1 * 10^{-3}$	NaCl, Gly, Na_2SO_4 [1.4-1.7]
NO_3^- control	1	N/A	$NaNO_3$, Na_2SO_4 [5.4*]
Cl^- control	1	N/A	Gly, Na_2SO_4 [1.3]

* The pH of the bulk solution, used since this aerosol had no glycine for pH measurement.

6.4.3 Comparison of Results to Models and Experiments

The kinetics of depletion have recently been discussed at a theoretical level by Chen et al.[32] They assumed that all of the depleting species (HNO_3 or HCl) is instantly formed and then calculated characteristic depletion times from a diffusion-limited mass-transfer equation.[36] The characteristic time, *t**, and an associated constant, *k*, are given in Equations 6.5 and 6.6

$$t^* = \frac{r_0^2}{k} \qquad 6.5$$

$$k = \frac{D * P}{R * T * C}\left(1 + \frac{V_n}{V_d}\right) \qquad 6.6$$

Here, *D* is diffusion coefficient, *P* is the partial pressure at the aerosol surface, and *C* is the concentration of HCl or HNO_3 in a droplet containing only the depleting solute. The V_n and V_d variables refer to the initial volume taken up by the nonvolatile and depleting species, respectively, while *R* is the gas constant, *T* is the temperature, and r_0 is the initial radius. A thermodynamic model such as E-AIM is used to calculate *P*, V_n and V_d for a given system.

While this formulation yields useful insights on the upper limit rate at which these processes can occur, these reactions will likely proceed more slowly for real aerosols. It has been previously shown that, while HNO_3 is 20% more stable near the air-water interface compared to the bulk, it will still dissociate in approximately 0.3 nanoseconds.[37] Therefore, rather than forming instantly in large quantities that diffuse to the surface for evaporation, it is likely HNO_3 or HCl occasionally forms transiently in the solution, and deplete only when they form in the interfacial region where then at the air/water interface evaporation into the gas phase occurs before dissociation.

To put our results in context with this upper limit, we performed calculations with the model of Chen et al. and E-AIM using malonic acid in place of glycine (see Methods).[32] We found

that a 4 μm radius aerosol has a characteristic depletion time of ca. 200 seconds. This is significantly faster than our rate constants, indicating that the kinetics we observed are not diffusion limited but are instead due to the probability of the depleting species associating near the interface. Our timescales also make more intuitive sense considering aerosol lifetime. Atmospheric particles can remain airborne across a wide range of times, depending on size and wind among other factors, but often have lifetimes on the order of days.[38,39] Given that total depletion is rarely observed for environmental aerosols, characteristic times of hours seem more reasonable than a few minutes.

Very recently, Jing *et al*. showed an approach for tracking pH change and hence chloride depletion in mixed sodium chloride and oxalic acid droplets.[34] Their data were reported as pH change over time, so in order to make a direct comparison, we analyzed their 80% RH data with first-order kinetics and obtained a chloride depletion rate constant of 7.0 ± 0.9 s^{-1} at 95% confidence for substrate-deposited aerosols with radii of ca. 9 μm. This rate is below what we found for both chloride and nitrate depletion, which we attribute to differences in the partial pressure of gases maintained above the droplets and the fact that their droplets were substrate-deposited, giving less surface area from which HCl could escape. More importantly, however, their findings are considerably slower than the theoretical rates discussed above, which they also attribute to differences in partial pressures. Thus, this comparison highlights both the differences in depletion rates that can be obtained by different techniques and the importance of using experiments to demonstrate the extent to which theoretical predictions are representative of real particles.

Rate measurements have also been recently reported for the depletion of ammonium.[40] For this process, the pH of the solution decreases over time as NH_4^+ dissociates to release acidic

protons and NH_3, which can escape as a gas. In this case, the data were analyzed in terms of a characteristic lifetime τ using Equation 6.7.

$$\frac{\mathrm{pH(t)} - \mathrm{pH}_\infty}{\mathrm{pH}_0 - \mathrm{pH}_\infty} = \mathrm{e}^{(\frac{-\mathrm{t}}{\tau})} \tag{6.7}$$

Here, $pH(t)$ is the pH at a given time, pH_∞ is the pH value the experiment approaches for long reaction times, pH_0 is the initial pH, and t is time. At 80% RH, values of τ for malonic or succinic acid droplets ranged ca. 10 to 20 minutes for nanoparticle-containing droplets with average radii of μm.[40] Using a similar analysis on an experiment where we kept an aerosol suspended for a protracted period of time, we calculated a τ of 8.6 minutes for chloride depletion. Once again, this comparison illustrates that the reactions proceed more slowly than the maximum diffusion-limited speed predicted by Chen *et al.*, but fast enough to occur at rates relevant to the atmosphere.[32]

6.5 Conclusions

We measured nitrate and chloride depletion rates from individual, levitated aerosols using Raman spectral peaks and glycine as an in-situ pH probe. First-order rates constants at 80% RH were found to be ca. 10^{-3} to 10^{-4} s^{-1}. These rates indicate that appreciable depletion can be expected during an aerosol's lifetime. Even for rapidly evaporating secondary organic aerosols, which could lose half of their volume in less than 100 minutes, loss of 60% of the initial nitrate could occur, leading to a net decrease in concentration even with a decrease in aerosol volume.[41] We emphasize that we have measured initial depletion rates here. For most atmospheric aerosols, as pH increases and nitrate or chloride concentrations decrease, the depletion rate would slow.

We have also demonstrated that there are few requirements for depletion to take place. We measured depletion at high relative humidity and for a growing aerosol, suggesting that that dehydration is not a necessary driver of the reaction. In addition, we saw depletion for aerosols with glycine as the only organic present, showing that other acids besides dicarboxylic acids can

play a role. We posit that the total acidity of the particle is one of the key factors that drives depletion. The volatility of dicarboxylic acids is low, similar to glycine, indicating they will remain in aerosols and provide acidic protons to nitrate or chloride for depletion.[42] Acetic acid, on the other hand, is highly volatile and expected to be found predominantly in the gas phase.[28] Therefore, acetic acid and similar low molecular weight monocarboxylic acids likely partition away from aerosols before appreciable depletion occurs. Our demonstration that glycine can cause depletion is useful because amino acids have been found to be greatly enriched in aerosols.[43,44] It is also noteworthy because glycine is not highly surface active, demonstrating that the acid in equations 6.1 and 6.2 does not have to reside at the surface.[4] In addition, future laboratory investigations of depletion can use glycine to add a non-evaporating molecule to the aerosols while increasing the viscosity to a lesser extent than if a longer chain organic acid was used.[45–47]

Overall, our results show the kinetics of depletion can be precisely determined from individual aerosols. Given the variability of enrichment factors that aerosols experience from nebulization, and the variability of concentrations in the atmosphere, additional studies may yield useful insights into the relationship between aerosol composition and depletion rate. Likely, the limiting factor is formation of the depleting species near the air/water interface. Whether organic acids explicitly assist with this formation by lowering the energy barrier of re-protonation of NO_3^- or Cl^- could be investigated further with computational methods. Ultimately, research in this area will help with aerosol source apportionment and predictions of aerosol hygroscopicity and pH.

6.6 Acknowledgements

Chapter 6, in full, contains original research that will be submitted for publication to Communications Chemistry in: Angle, Kyle; Li, Meng; Grassian, Vicki, Direct Quantification of

Nitrate and Chloride Depletion Kinetics from Single Levitated Aerosols in 2023. The dissertation author was the primary investigator and author of this paper.

This material is based upon work supported by the Air Force Office of Scientific Research award FA9550-22-1-0199. The authors thank Meng Li for helpful discussions and Christopher Nowak for assistance in sample preparation.

6.7 Appendix

6.7.1 Supporting Figures

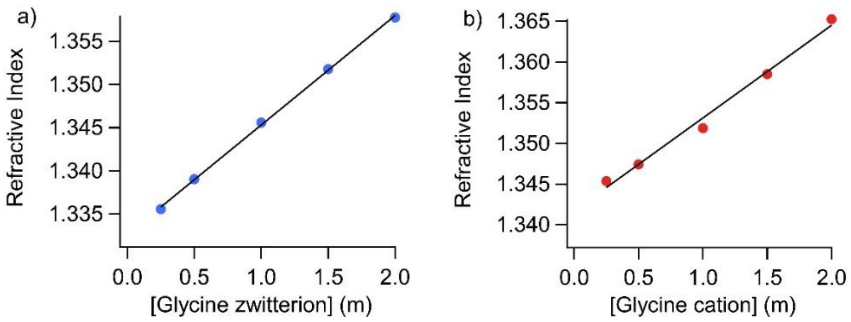

Figure 6.5: Refractive index data for glycine. (a) Refractive index for glycine solutions dissolved in pure water. (b) Refractive index for glycine solutions acidified with 6 N HCl such that > 99% of the glycine was cationic (ca. pH 0.6). Note that the intercept is higher than (a) due to the effect of the added acid.

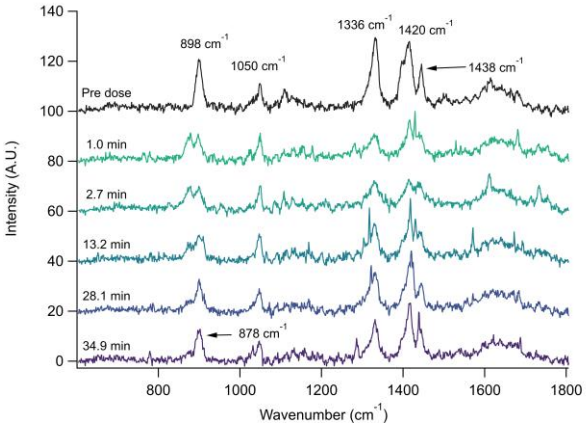

Figure 6.6: Chloride depletion spectra after a coalescence event. An aerosol was trapped from a solution of 2 m glycine, 2 m NaCl and 0.1 m $NaNO_3$. The spectrum labeled "Pre dose" is recorded for the trapped aerosol and is stabilized (ca. 8 minutes). The aerosol is then titrated with 1 m HCl and acidified, at which point we set time = 0 minutes. Subsequently, aerosol pH increases as shown in the remaining spectra. This increase is faster than would occur for nitrate depletion, highlighting that chloride depletion is faster than nitrate depletion. Traces show averages of 10 spectra each and sharp, unmarked peaks correspond to WGMs.

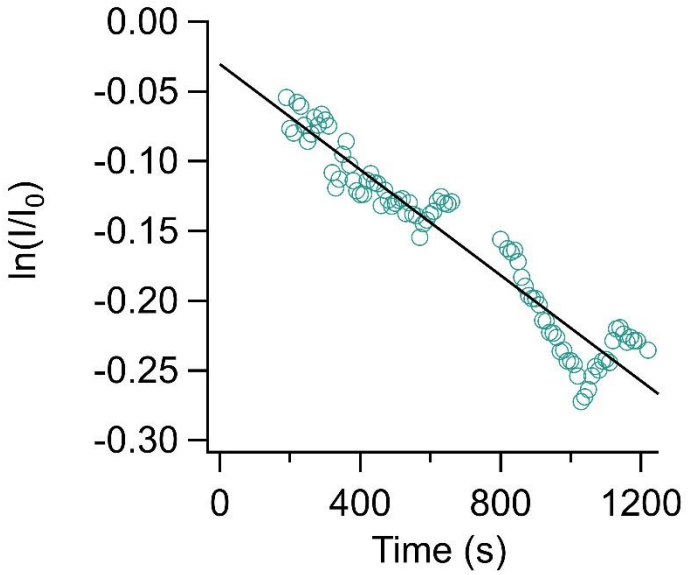

Figure 6.7: Nitrate depletion for an aerosol without organics. A bulk solution of 1 m $NaNO_3$ and 1.2 m Na_2SO_4 adjusted to pH 1.7 with H_2SO_4 was prepared. The aerosol was nebulized into a high RH environment (ca. 92 ± 8%) to reduce additional acidification from concentration. Spectra were collected for 152 minutes. During the first 21 minutes, nitrate depletion was observed via normalization of the nitrate peak to the sulfate peak. The first-order kinetics fit of this portion of the data is shown. The absolute value of the slope, which is *k*, is 1.9 ± 0.1 * 10^{-4} s^{-1}, and R^2 is 0.92. While the pH of this aerosol could not be directly measured, the data illustrates that depletion can occur in the absence of an organic when there is sufficient acidity present.

6.7.2 Error Propagation

Here, we will analyze the error associated with the chloride depletion experiment with the most uncertainty to illustrate the scope of our method. At 95% confidence, the slope *m* of the calibration curve given in Figure 6.1b is 222 ± 6 m^{-1}, and the intercept *b* is 0.1 ± 0.1. For a particular chloride depletion experiment, due to the overlap of the C-COOH and $C\text{-}COO^-$ peaks, the average uncertainties in their peak intensities from Gaussian peak fitting are 10% and 19%, respectively. Terming the peak ratio *y*, based on Figure 6.1b we have

$$\mathrm{pH} = -\log([\mathrm{H}^+]) = -\log\left(\frac{\mathrm{y}-\mathrm{b}}{\mathrm{m}}\right) \tag{6.8}$$

Since *y* is determined from a ratio of peak intensities, we propagate its uncertainty via percentages. This uncertainty must then be converted back into an absolute uncertainty to propagate with *b*,

which can be accomplished by using the average *y* value of 1.72 which we will term a_y, and then we once again convert to a percentage to propagate by division with *m*. Therefore, we get an error *e* according to the following:

$$e = \sqrt{\left[\frac{\sqrt{\left\{\sqrt{\left(\frac{s_{C-COOH}}{a_{C-COOH}}\right)^2 + \left(\frac{s_{C-COO-}}{a_{C-COO-}}\right)^2} * a_y\right\}^2 + s_b^2}}{a_y}\right]^2 + \left(\frac{s_m}{a_m}\right)^2} \quad (6.9)$$

In this equation, *s* refers to the 95% confidence error of a given component, *a* refers to a given value (a slope, intercept, or average value from peak intensities) and different style brackets are used for visual clarity only (all work as parentheses). Above we reported 95% values as percentages for ease of reading, but taking *s* divided by *a* yields decimal answers, which are appropriate for error propagation.[35] For our high-error chloride depletion, *e* is 22%, which unsurprisingly is dominated by the uncertainty in the glycine peak intensities. As a point of comparison, the 95% confidence interval for the slope of the first-order kinetics fit for the same experiment is $1.05 \pm 0.06 * 10^{-3}$ s^{-1}, which carries an uncertainty of only 6%. In general, first-order fits were found appropriate for the initial depletion rates, with nitrate and chloride depletion having average R^2 values of 0.84 and 0.96, respectively. Finally, for the chloride depletion reported in Table 6.1, the standard deviation is 13%, which while within error propagation, may also be in part due to variability between trials from nebulization enrichment and hence different starting pH values. Overall, error propagation demonstrates the potential utility of future substrate-deposited experiments, where greater Raman signal will decrease the uncertainty in the overlapping glycine peaks, which currently dominate error for *individual* experiments. For uncertainty between different experiments, ideally enrichment would be better constrained, which could potentially be achieved with the development of new nebulization methods. As a final note, we used peak

intensities instead of peak area in this study because we found both approaches gave similar average depletion *k* values, but using intensities led to significantly less uncertainty for chloride depletion. As long as the data points where a WGM directly overlaps with the peak of interest can be removed, using peak intensities gives a greater number of useful data points than peak areas, since in practice the travelling of WGM's across the small glycine C-COOH and C-COO^- peaks led to substantial peak area uncertainty in our Igor fits. For chloride depletion, using peak intensities gave $k = 1.0 \pm 0.1 * 10^{-3}$ s^{-1}, while using peak areas gave $k = 1.4 \pm 0.8 * 10^{-3}$ s^{-1}. For nitrate depletion, the *k* values were $1.3 \pm 0.4 * 10^{-4}$ s^{-1} and $1.4 \pm 0.4 * 10^{-4}$ s^{-1}, respectively. Less error is found for nitrate depletion, likely because the Raman nitrate peak has a strong intensity and is well-defined for peak fitting.

6.8 References

(1) Huang, S.; Wu, Z.; Wang, Y.; Poulain, L.; Höpner, F.; Merkel, M.; Herrmann, H.; Wiedensohler, A. Aerosol Hygroscopicity and Its Link to Chemical Composition in a Remote Marine Environment Based on Three Transatlantic Measurements. *Environ. Sci. Technol.* **2022**, *56* (13), 9613–9622.

(2) Jing, B.; Wang, Z.; Tan, F.; Guo, Y.; Tong, S.; Wang, W.; Zhang, Y.; Ge, M. Hygroscopic Behavior of Atmospheric Aerosols Containing Nitrate Salts and Water-Soluble Organic Acids. *Atmos. Chem. Phys.* **2018**, *18* (7), 5115–5127.

(3) Duan, J.; Lyu, R.; Wang, Y.; Xie, X.; Wu, Y.; Tao, J.; Cheng, T.; Liu, Y.; Peng, Y.; Zhang, R.; He, Q.; Ga, W.; Zhang, X.; Zhang, Q. Particle Liquid Water Content and Aerosol Acidity Acting as Indicators of Aerosol Activation Changes in Cloud Condensation Nuclei (CCN) during Pollution Eruption in Guangzhou of South China. *Aerosol Air Qual. Res.* **2019**, *19*, 2662–2670.

(4) Angle, K. J.; Nowak, C. M.; Davasam, A.; Dommer, A. C.; Wauer, N. A.; Amaro, R. E.; Grassian, V. H. Amino Acids Are Driven to the Interface by Salts and Acidic Environments. *J. Phys. Chem. Lett.* **2022**, *13* (12), 2824–2829.

(5) Kleinman, M. T.; Phalen, R. F.; Mautz, W. J.; Mannix, R. C.; McClure, T. R.; Crocker, T. T. Health Effects of Acid Aerosols Formed by Atmospheric Mixtures. *Environ. Health Perspect.* **1989**, *79*, 137.

(6) Zheng, G.; Su, H.; Wang, S.; Andreae, M. O.; Pöschl, U.; Cheng, Y. Multiphase Buffer Theory Explains Contrasts in Atmospheric Aerosol Acidity. *Science* **2020**, *369* (6509), 1374–1377.

(7) Rizzuto, A. M.; Cheng, E. S.; Lam, R. K.; Saykally, R. J. Surprising Effects of Hydrochloric Acid on the Water Evaporation Coefficient Observed by Raman Thermometry. *J. Phys. Chem. C* **2017**, *121* (8), 4420–4425.

(8) Francisco, K. C. A.; Costa, M. A. M.; Cardoso, A. A. Temporal Variations, Transport, and Regional Impacts of Atmospheric Aerosol and Acid Gases Close to an Oil and Gas Trading Hub. *Int. J. Environ. Sci. Technol. 2022* **2022**, 1–14.

(9) Laskin, A.; Moffet, R. C.; Gilles, M. K.; Fast, J. D.; Zaveri, R. A.; Wang, B.; Nigge, P.; Shutthanandan, J. Tropospheric Chemistry of Internally Mixed Sea Salt and Organic Particles: Surprising Reactivity of NaCl with Weak Organic Acids. *J. Geophys. Res. Atmos.* **2012**, *117* (15).

(10) Dang, C.; Segal-Rozenhaimer, M.; Che, H.; Zhang, L.; Formenti, P.; Taylor, J.; Dobracki, A.; Purdue, S.; Wong, P. S.; Nenes, A.; Sedlacek, A.; Coe, H.; Redemann, J.; Zuidema, P.; Howell, S.; Haywood, J. Biomass Burning and Marine Aerosol Processing over the Southeast Atlantic Ocean: A TEM Single-Particle Analysis. *Atmos. Chem. Phys.* **2022**, *22* (14), 9389–9412.

(11) Bondy, A. L.; Wang, B.; Laskin, A.; Craig, R. L.; Nhliziyo, M. V.; Bertman, S. B.; Pratt, K. A.; Shepson, P. B.; Ault, A. P. Inland Sea Spray Aerosol Transport and Incomplete Chloride Depletion: Varying Degrees of Reactive Processing Observed during SOAS. *Environ. Sci. Technol.* **2017**, *51* (17), 9533–9542.

(12) Johansen, A. M.; Hoffmann, M. R. Chemical Characterization of Ambient Aerosol Collected during the Northeast Monsoon Season over the Arabian Sea: Anions and Cations Cations. *J. Geophys. Res* **2004**, *109*, D05305.

(13) Ghorai, S.; Wang, B.; Tivanski, A.; Laskin, A. Hygroscopic Properties of Internally Mixed Particles Composed of NaCl and Water-Soluble Organic Acids. *Environ. Sci. Technol.* **2014**, *48* (4), 2234–2241.

(14) Wang, B.; Laskin, A. Reactions between Water-Soluble Organic Acids and Nitrates in Atmospheric Aerosols: Recycling of Nitric Acid and Formation of Organic Salts. *J. Geophys. Res. Atmos.* **2014**, *119* (6), 3335–3351.

(15) Huang, Q.; Vikesland, P. J. In Situ pH Measurement of Water Droplets Using Flash-Freeze Surface-Enhanced Raman Spectroscopy. *Environ. Sci. Technol. Lett.* **2022**, *2022*, 459–465.

(16) Su, B.; Zhuo, Z.; Fu, Y.; Sun, W.; Chen, Y.; Du, X.; Yang, Y.; Wu, S.; Xie, Q.; Huang, F.; Chen, D.; Li, L.; Zhang, G.; Bi, X.; Zhou, Z. Individual Particle Investigation on the Chloride Depletion of Inland Transported Sea Spray Aerosols during East Asian Summer Monsoon. *Sci. Total Environ.* **2021**, *765*, 144290.

(17) Sharma, B.; Jia, S.; Polana, A. J.; Ahmed, M. S.; Haque, R. R.; Singh, S.; Mao, J.; Sarkar, S. Seasonal Variations in Aerosol Acidity and Its Driving Factors in the Eastern Indo-Gangetic Plain: A Quantitative Analysis. *Chemosphere* **2022**, *305*, 135490.

(18) Ma, S.; Li, Q.; Zhang, Y. A Comprehensive Study on Hygroscopic Behaviour and Nitrate Depletion of NaNO3 and Dicarboxylic Acid Mixtures: Implications for Nitrate Depletion in Tropospheric Aerosols. *Atmos. Chem. Phys.* **2022**, *22* (16), 10955–10970.

(19) Shao, X.; Wu, F. M.; Yang, H.; Pang, S. F.; Zhang, Y. H. Observing HNO_3 Release Dependent upon Metal Complexes in Malonic Acid/Nitrate Droplets. *Spectrochim. Acta Part A Mol. Biomol. Spectrosc.* **2018**, *201*, 399–404.

(20) Pathak, R. K.; Yao, X.; Chan, C. K. Sampling Artifacts of Acidity and Ionic Species in PM2.5. *Environ. Sci. Technol.* **2004**, *38* (1), 254–259.

(21) Su, B.; Wang, T.; Zhang, G.; Liang, Y.; Lv, C.; Hu, Y.; Li, L.; Zhou, Z.; Wang, X.; Bi, X. A Review of Atmospheric Aging of Sea Spray Aerosols: Potential Factors Affecting Chloride Depletion. *Atmos. Environ.* **2022**, *290*, 119365.

(22) Angle, K. J.; Neal, E. E.; Grassian, V. H. Enhanced Rates of Transition-Metal-Ion-Catalyzed Oxidation of S(IV) in Aqueous Aerosols: Insights into Sulfate Aerosol Formation in the Atmosphere. *Environ. Sci. Technol.* **2021**, *55* (15), 10291–10299.

(23) Clegg, S. L.; Brimblecombe, P.; Wexler, A. S. Thermodynamic Model of the System H^+-NH_4^+-Na^+-SO_4^{2-}-NO_3^--Cl^--H_2O at 298.15 K. *J. Phys. Chem. A* **1998**, *102* (12), 2155–2171.

(24) Clegg, S. L.; Brimblecombe, P.; Wexler, A. S. Extended AIM aerosol thermodynamics model http://www.aim.env.uea.ac.uk/aim/aim.php (accessed May 27, 2020).

(25) Craig, R. L.; Nandy, L.; Axson, J. L.; Dutcher, C. S.; Ault, A. P. Spectroscopic Determination of Aerosol pH from Acid–Base Equilibria in Inorganic, Organic, and Mixed Systems. *J. Phys. Chem. A* **2017**, *121* (30), 5690–5699.

(26) Coddens, E. M.; Angle, K. J.; Grassian, V. H. Titration of Aerosol pH through Droplet Coalescence. *J. Phys. Chem. Lett.* **2019**, *10* (15), 4476–4483.

(27) Zhang, H.; Xie, C.; Liu, Z.; Gong, J.; Bao, Y.; Zhang, M.; Hao, H.; Hou, B.; Yin, Q. X. Identification and Molecular Understanding of the Odd-Even Effect of Dicarboxylic Acids Aqueous Solubility. *Ind. Eng. Chem. Res.* **2013**, *52* (51), 18458–18465.

(28) Meng, Z.; Seinfeld, J. H.; Saxena, P. Gas/Aerosol Distribution of Formic and Acetic Acids. *Aerosol Sci. Technol.* **1995**, *23* (4), 561–578.

(29) Sjöberg, B.; Foley, S.; Cardey, B.; Enescu, M. An Experimental and Theoretical Study of the Amino Acid Side Chain Raman Bands in Proteins. *Spectrochim. Acta Part A Mol. Biomol. Spectrosc.* **2014**, *128*, 300–311.

(30) Sander, R. Compilation of Henry's Law Constants (Version 4.0) for Water as Solvent.

Atmos. Chem. Phys **2015**, *15*, 4399–4981.

(31) Chen, Z.; Liu, P.; Liu, Y.; Zhang, Y. H. Strong Acids or Bases Displaced by Weak Acids or Bases in Aerosols: Reactions Driven by the Continuous Partitioning of Volatile Products into the Gas Phase. *Acc. Chem. Res.* **2021**, *54* (19), 3667–3678.

(32) Chen, Z.; Liu, P.; Su, H.; Zhang, Y.-H. Displacement of Strong Acids or Bases by Weak Acids or Bases in Aerosols: Thermodynamics and Kinetics. *Environ. Sci. Technol.* **2022**, *2022*, 12937–12944.

(33) Zhuang, H.; Chan, C. K.; Fang, M.; Wexler, A. S. Formation of Nitrate and Non-Sea-Salt Sulfate on Coarse Particles. *Atmos. Environ.* **1999**, *33* (26), 4223–4233.

(34) Jing, X.; Chen, Z.; Huang, Q.; Liu, P.; Zhang, Y.-H. Spatiotemporally Resolved pH Measurement in Aerosol Microdroplets Undergoing Chloride Depletion: An Application of In Situ Raman Microspectrometry.

(35) Skoog, D. A.; Crouch, S. R.; Holler, F. J. *Principles of Instrumental Analysis, 7th Edition*; 2016.

(36) Ray, A. K.; Davis, E. J.; Ravindran, P. Determination of Ultra-low Vapor Pressures by Submicron Droplet Evaporation. *J. Chem. Phys.* **2008**, *71* (2), 582.

(37) Anglada, J. M.; Martins-Costa, M. T. C.; Francisco, J. S.; Ruiz-Lópezlópez, M. F. Reactivity of Undissociated Molecular Nitric Acid at the Air−Water Interface. *J. Am. Chem. Soc* **2021**, *143*, 59.

(38) Haszpra, T. Intricate Features in the Lifetime and Deposition of Atmospheric Aerosol Particles. *Chaos An Interdiscip. J. Nonlinear Sci.* **2019**, *29* (7), 071103.

(39) Toossi, R.; Novakov, T. The Lifetime of Aerosols in Ambient Air: Consideration of the Effects of Surfactants and Chemical Reactions. *Atmos. Environ.* **1985**, *19* (1), 127–133.

(40) Li, L.-F.; Chen, Z.; Liu, P.; Zhang, Y.-H. Direct Measurement of pH Evolution in Aerosol Microdroplets Undergoing Ammonium Depletion: A Surface-Enhanced Raman Spectroscopy Approach. *Environ. Sci. Technol.* **2022**, *56* (10), 6274–6281.

(41) Vaden, T. D.; Imre, D.; Beránek, J.; Shrivastava, M.; Zelenyuk, A. Evaporation Kinetics and Phase of Laboratory and Ambient Secondary Organic Aerosol. *Proc. Natl. Acad. Sci. U. S. A.* **2011**, *108* (6), 2190–2195.

(42) Price, C. L.; Kaur Kohli, R.; Shokoor, B.; Davies, J. F. Connecting the Phase State and Volatility of Dicarboxylic Acids at Elevated Temperatures. *J. Phys. Chem. A* **2022**, *2022*, 6972.

(43) Triesch, N.; Van Pinxteren, M.; Salter, M.; Stolle, C.; Pereira, R.; Zieger, P.; Herrmann, H. Sea Spray Aerosol Chamber Study on Selective Transfer and Enrichment of Free and Combined Amino Acids. *ACS Earth Sp. Chem.* **2021**, *5* (6), 1564–1574.

(44) Barbaro, E.; Zangrando, R.; Moret, I.; Barbante, C.; Cescon, P.; Gambaro, A. Free Amino Acids in Atmospheric Particulate Matter of Venice, Italy. *Atmos. Environ.* **2011**, *45* (28), 5050–5057.

(45) Tadkalkar, A. P.; Bichile, G. K. Excess Parameters of Glycine in Aqueous Sodium Chloride. *Adv. Appl. Sci. Res.* **2012**, *3* (6), 3629–3632.

(46) Gervasi, N. R.; Topping, D. O.; Zuend, A. A Predictive Group-Contribution Model for the Viscosity of Aqueous Organic Aerosol. *Atmos. Chem. Phys.* **2020**, *20* (5), 2987–3008.

(47) Parmar, M. L.; Guleria, M. K. Viscosities of Oxalic Acid and Its Salts in Water and Binary Aqueous Mixtures of Tetrahydrofuran at Different Temperatures. *J. Chem. Sci* **2005**, *117* (4), 351–357.

CHAPTER 7 AMINO ACIDS ARE DRIVEN TO THE INTERFACE BY SALTS AND ACIDIC ENVIRONMENTS

7.1 Abstract

Amino acids (AAs), the building blocks of proteins, are enriched by several orders of magnitude in sea spray aerosols compared to ocean waters. This suggests that AAs may reside at the air-water interface and be highly surface active. Using surface tension measurements, infrared reflection-absorption spectroscopy, and molecular dynamics simulations, we show that AAs are surface active and that salts and low pH environments are drivers of surface activity. At typical sea spray salt concentrations and pH values, we determine that the surface coverage of hydrophobic AAs increases by approximately one order of magnitude. Additionally, divalent cations such as Ca^{2+} and Mg^{2+} can further increase AA surface propensity, particularly at neutral pH. Overall, these results indicate that AAs are likely to be found at elevated concentrations at the surface of sea spray aerosols, where they can impact cloud activation properties of the aerosol as well as enhanced peptide formation under certain conditions.

7.2 Introduction

Amino acids (AAs) are the building blocks of proteins and thus critical to life. In ocean waters, dissolved free AAs are an important source of nitrogen and carbon for marine life, particularly bacteria.[1] Despite being present in concentrations of only 1 to 3000 nM, AAs are able to be transferred efficiently across the air/water interface from ocean waters into aerosols.[1–4] Most notably, Triesch *et al.* recently demonstrated that AAs are enriched into sea spray aerosols (SSA) by up to *seven orders* of magnitude, with greater enrichment identified for smaller aerosols.[5] While the selective transfer of longer chain fatty acids across the ocean-air interface has been well-

established, AAs are a relatively understudied in marine aerosol chemistry.[6] Their presence in SSA is important, as it has been shown that AAs impact the hygroscopicity and phase state of aerosols.[7] In addition, AAs can contribute to new particle formation in the atmosphere.[8]

The chemical environment within SSA is complex. Within minutes of emission from the ocean, SSA can be rapidly acidified from slightly alkaline ocean levels to acidic pH values between 2 to 4, and can further drop to below pH 0 with atmospheric aging.[9,10] Additionally, SSA have much higher ionic strengths than the ocean (ca. 0.7 m), containing up to 5 m sodium chloride.[11] It has also been shown that calcium can be greatly enriched into SSA.[6,12,13] Magnesium, the other main divalent cation in seawater, is enriched relative to sodium in SSA as well.[13]

These low pH, high salt, and high divalent cation conditions could have an important impact on the behavior of AAs within SSA. In near neutral aqueous solutions, many AAs are zwitterions, containing cationic amine and anionic carboxylate groups. At highly acidic pH levels, the carboxylate ion becomes protonated and the AA becomes cationic. This can impact the solubility of the AA and whether it dissolves more readily in the core of the SSA or at the air-water interface. In fact, Herboth *et al.* used molecular dynamics simulations to show that phenylalanine (Phe) and valine (Val) have greater affinity for the interface at low pH, while glycine (Gly) did not.[14] It has also been shown that salts can either drive proteins to or away from the air-water interface.[15–17] Determining whether AAs reside at SSA interfaces is important because the surface of an aerosol impacts its properties of water uptake, morphology, and heterogeneous chemical transformations.[18–20] It is also essential to determine the behavior of AAs and peptides in aerosols as they are used in food and medicine, including trileucine as a medicinal aerosol dispersibility enhancer.[21]

To quantify the surface propensity of AAs in SSA-like environments, we applied surface tension measurements and infrared reflection-absorption spectroscopy (IRRAS) for six different AAs. Leucine (Leu) and isoleucine (Ile) were chosen as they are the most hydrophobic AAs at the low pH of SSA.[22] Phe, Val, and Gly were chosen to expand on the simulation work by Herboth *et al*.[14] Finally, methionine (Met) was chosen since its side chain contains a sulfur atom which displays strong reactivity with atmospherically-relevant species such as hypochlorous acid.[23] To further gain insight into the interfacial orientation and energetics of AAs, we applied potential of mean force (PMF) calculations to Leu, one of the most hydrophobic AAs. The overall goal was to quantify enhancement in surface concentration of AAs due to the low pH and high ionic strength conditions typical of SSA to better understand how these key biological building blocks behave in the marine atmosphere.

7.3 Methods

A full description of experimental and computational methods can be found in the SI of the publication corresponding to this chapter (see Appendix). In this chapter, "pH 1" and "pH 6" are used to succinctly refer to highly acidic (pH 0.55) solutions and unadjusted solutions at the isoelectric point of the AA (ca. pH 5.8 to 6.1), respectively. These pH values were chosen to isolate different protonation states of the AAs. The pH 1 solutions caused > 97% of the AA to be in the cationic form (with lower pH solutions not being possible due to equipment corrosion) and the pH 6 solutions caused > 99% of the AA to be in the zwitterionic form (see Table 1).

Table 7.1: Amino acid speciation data and aerosol enrichment factors.

AA	Aerosol Enrichment Factor*	pKa_1[24]	Cation Fraction Present at "pH 1"	Zwitterion Fraction Present at "pH 6"
Leu	6.6E+02 – 1.3E+06	2.32	0.983	1.000
Ile	9.7E+03 – 1.8E+06	2.26	0.981	1.000
Val	5.1E+03 – 7.4E+06	2.27	0.981	1.000
Phe	4.1E+03 – 3.4E+06	2.18	0.977	0.999
Met	N/A	2.16	0.976	0.999
Gly	4.2E+04 – 3.5E+07	2.34	0.984	1.000

* = Aerosol Enrichment Factors are taken from the range of size-separated values measured by Triesch *et al.*[5] N/A = Data analysis in Triesch *et al.* did not include Met.

7.4 Results and Analysis

In order to determine the impact of ions on the surface propensity of AAs, the surface pressure of AA solutions as a function of bulk concentration was first determined for each pH condition (see Figure 7.4). Surface pressure, π, was calculated by Equation 7.1

$$\pi = \gamma_0 - \gamma \tag{7.7}$$

Here, γ_0 is the surface tension of a solution at a given pH and salt concentration, and γ is the surface tension of the same solution with the added AA. For the hydrophobic AAs studied here, π increases with AA concentration, since the surface activity of the AAs lowers the surface tension of water. A linear regression was performed on each data set, and the resulting slope was used to calculate the surface excess concentration, Γ, as defined by the Gibbs adsorption equation (Equation 7.2).[25]

$$\Gamma = -\frac{C}{RT} * (\frac{\partial \pi}{\partial C})_T \tag{7.8}$$

For Equation 7.2, C is AA concentration, R is the gas constant, and T is temperature. At a bulk concentration of 65 millimolal, the Γ values for the hydrophobic amino acids we studied ranged from 0.1 to 0.8 μmol/m^2. This is below the Γ values typical of fatty acids and comparable

to high mole fractions of methanol, which makes sense given that AAs, on their own, are only weakly surface active.[26,27]

Next, the impact of each salt on π was determined by measuring a series of solutions where only the salt concentration changed. Measurements were made across the range of solubility for NaCl, $MgCl_2$ and $CaCl_2$, and the resulting data were typically linear.[28] Note that the non-zero intercepts obtained by linear regression of these data are expected, since the AA solutions exhibit π even in the absence of added salts. From these data, it is clear that these 65 millimolal AA solutions in the presence of high salt concentrations exhibit π comparable to pure AA solutions of significantly higher concentrations. For example, in the case of Phe, the π values at high concentrations correspond to monolayers of Phe with packing densities greater than 15 $Å^2$/molecule.[29] To quantify the salt-driven π enhancement, we defined a surface enhancement factor, SEF (Equation 7.3).

$$SEF = \frac{\pi_s}{(\frac{\partial \pi}{\partial C})_T * C_s} \tag{7.9}$$

Here, π_s and C_s are the surface pressure and AA concentrations at the salt concentration of interest, which we chose to be 5 m, a concentration observed for NaCl in SSA.[11] A comparison of SEF values for various AA, salt, and pH conditions is given in Figure 7.1. These SEF values represent the minimum surface enhancement expected for AAs in the given conditions.

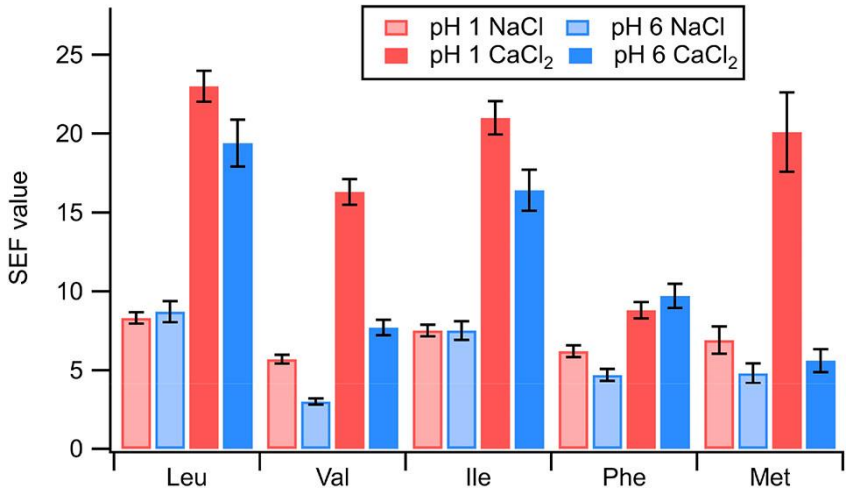

Figure 7.1: Comparison of SEF values for various aqueous phase conditions of pH and different salts. Data show the average of replicate experiments and error bars reflect one standard deviation.

The data show that surface enhancement at pH 1 is consistently either greater than or equal to that at pH 6 within the margin of error. This is consistent with recent data showing that the cationic form of surface-active AAs has the greatest affinity for the air-water interface.[14] The effect is particularly apparent for $CaCl_2$ solutions with the branched chain AAs along with Met. The exception is Phe, which shows no statistically significant difference for pH 1 and pH 6 $CaCl_2$ solutions. This may be due to π-stacking effects making side chain interactions more dominant than interactions between the carboxylic acid or carboxylate group with salts.[30] Regardless of the cause, the data is also consistent with the findings of Griffith and Vaida, who found the equilibrium surface pressures of Phe solutions at low and neutral pH levels to be identical within experimental error.[31] We also obtained data for solutions with both the cationic and zwitterionic forms of the AA present at pH 3, where the average surface pressure results are in between the pH 1 and pH 6 surface pressures.

In addition, the data in Figure 7.1 show the enhancement in π in the presence of $CaCl_2$ to be greater than that of NaCl. For pH 6, we attribute this to the greater affinity of Ca^{2+} for binding with the COO- group compared to the Na^+ cation. For pH 1, this is likely due to the increased concentrations of Cl^- that can screen positive charges at the interface to allow more efficient surface packing.[32] The relationship between surface pressure and [Cl^-] is nearly identical for NaCl and $CaCl_2$ at pH 1 whereas there is a noticeable distinction for the two salts at pH 6. This indicates the identity of the cation is more important at pH 6 while the amount of anion is more important at pH 1.

To probe the impact of the identity of the cation on AA surface pressure, we compared measurements of samples in $CaCl_2$ and $MgCl_2$ solutions (Figure 7.5). We observed that, at pH 1, there was no statistically significant difference between the π measurements. This corroborates our hypothesis that the salt-driven surface activity is dominated by the anion in acidic solutions. At pH 6, by contrast, the π values from $CaCl_2$ solutions are consistently higher than those of $MgCl_2$ solutions for the branched chain AAs. Since the side chains of these AAs are hydrophobic, it is likely that they are "sticking up" into the air at the interface, leaving the zwitterionic groups in the water. The strong ability of Ca^{2+} to screen these adjacent charges may contribute to stabilization at the interface.[33] We note again that Phe is the exception, possibly due to the aromatic side chains causing a different orientation at the interface.[30]

For a point of contrast, we also measured the π of Gly solutions at pH 1 and 6 in the presence of NaCl and $CaCl_2$. As the smallest AA and one that is substantially more soluble than the other AAs measured here, we expected Gly to exhibit less surface activity. Indeed, negative π values indicate Gly behaves more like a solute than a surfactant in the presence of NaCl. Interestingly, as the concentration of $CaCl_2$ increases, π gradually transitions from negative to

positive, indicating that highly concentrated calcium solutions can change the role of Gly from a solute to a surfactant. This is noteworthy, since Gly is expected to always reside in the bulk solution away from the interface due to its solubility.[34] However, these new data presented here indicate under certain conditions this may not be the case, although we emphasize the effect is small.

To confirm our hypothesis that salts increase the surface propensity of AAs, we used IRRAS to measure AA solutions with and without salts present. A representative result is given in Figure 7.2 where several (negative) peaks show greater intensity in the presence of 3 vs 0 m $CaCl_2$. It has been demonstrated that IRRAS band intensities are not expected to increase linearly with surface concentration due to exciton delocalization and the loss of many small bands in the IRRAS baseline.[35] As a result, and due to the potential impact of different cations on the interfacial structure of water, we have not attempted to use IRRAS in a quantitative way to compare the efficacy of different salts in driving AAs to the surface. Nevertheless, our data corroborate our π measurements by showing that AA peaks exhibit enhancement in the presence of salts.

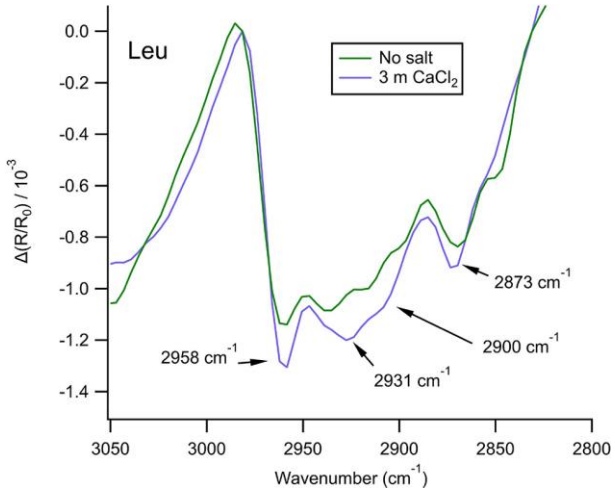

Figure 7.2: Representative IRRAS spectra for Leu pH 1 solutions with 0 and 3 m $CaCl_2$ concentrations. Enhancements in C–H stretches are apparent (note peaks are negative).

To aid in the explanation of these experimental data and to better understand the behavior of AAs at the air-water interface, we turned to molecular dynamics (MD) pulling simulations combined with umbrella sampling. These were performed as described by Herboth *et al.*[14] From these simulations, we were able to calculate the potential of mean force of pulling Leu from a salt solution into the gas phase. Representative results for Leu are given in Figure 7.3 (left) and an image of Leu cation at the air/water interface is also shown. The energy minimum corresponds to the air-water interface and is seen to be 8 ± 2 kJ/mol lower for the cation than the zwitterion. Additionally, while we observed that the COOH group of the Leu cation occasionally faced the gas phase at the air water interface, the COO^- group of the zwitterion rarely did so (Figure 7.6). This is consistent with our experimental determination that the identity of the salt cation is less important for highly acidic solutions, where interfacial carboxylic groups may be less likely to interact with aqueous ions.

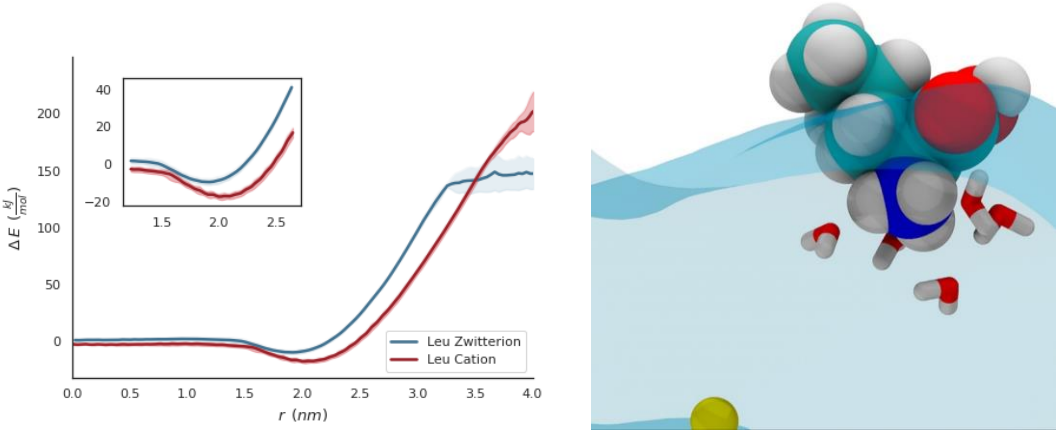

Figure 7.3: (left) Potential of mean force profile and energy well comparison for a Leu zwitterion and cation. The inset shows an expanded view of the energy minimum; (right) representative image of Leu cation at the air/water interface.

Surface propensity of AAs at the air/water interface are shown to be increased under high salt, and low pH conditions as well as in the presence of divalent cations. These conditions are highly relevant to SSAs as it has been shown that these aerosols undergo rapid acidification after

emission from the ocean.[9] In addition, water loss after emission causes concentration of existing components such as NaCl and $CaCl_2$. Therefore, while AAs may have low surface activity under most conditions and be most energetically stable in the bulk solution, the combination of acidification and increased concentrations of salts and AAs will drive them to the aerosol-air interface. At the interface, they can more readily undergo chemical reactions, including peptide formation under certain conditions, which is of interest from an origin of life perspective.[36] AAs can be a factor in aerosol hygroscopicity and cloud formation.[37] For example, Marsh *et al.* found that AAs are more hygroscopic than predicted by models, likely because their zwitterionic form makes them behave more like salts than other organics.[38] Therefore, when investigating water uptake or even aerosol morphology with the assumption that the aerosol is coated with organics, it is important to consider whether AAs driven to the surface as part of this coating behave more like salts or disrupt the structure of existing monolayers.[39] In terms of heterogeneous chemistry, in addition to the aforementioned reaction of Met with HOCl,[23] there are likely a wide range of interfacial reactions possible with AAs including acid-base chemistry, given the diversity of their side chains and the presence of both amine and carboxylate groups. Combined with the recent demonstration of the 10^3 to 10^7 enrichment of AAs from the ocean into sea spray aerosols,[5] our data showing that AAs are driven to the surface by salts and low pH conditions indicate that AAs may be more important components of marine aerosol interfacial chemistry than has been previously realized. These results can also provide insights into the behavior of free AAs in different environments where air-water interfaces are present.

7.5 Acknowledgements

Chapter 7, in part, is a reprint of the material published by the Journal of Physical Chemistry Letters in: Angle, Kyle; Nowak, Christopher; Davasam, Aakash; Dommer, Abigail; Wauer, Nicholas; Amaro, Rommie; Grassian, Vicki, Amino Acids Are Driven to the Interface by Salts and Acidic Environments in 2022. The dissertation author was the primary investigator and author of this paper.

The authors thank Dr. Mark Young for assistance with IRRAS measurements. The authors thank Dr. Andy Goetz for assistance in developing PMFs. The authors thank Dr. Malin Wohlert and Radost Herboth for assistance in applying a flat bottom potential and Dr. Justin Lemkul for providing a user-friendly umbrella sampling tutorial. This work used the PSC Bridges-2 supercomputer through Extreme Science and Engineering Discovery Environment (XSEDE) allocation TG-CHE060073 provided to R.E.A., which is supported by National Science Foundation Grant ACI-1548562. This work was supported by the National Science Foundation (Grant CHE-1801971).

7.6 Appendix

Supporting discussions, methods, calculations, figures, and tables can be found free of charge in the Supporting Information of the publication corresponding to this chapter.[40]

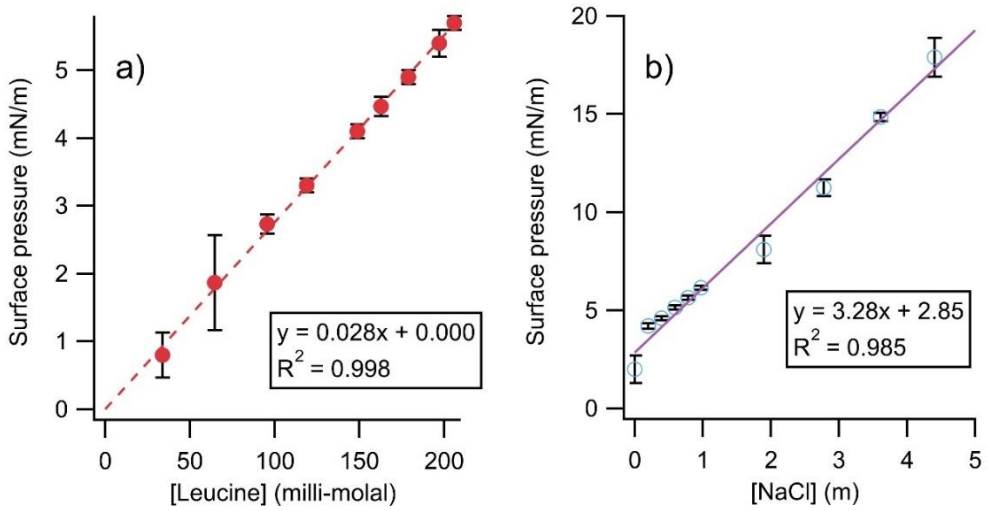

Figure 7.4: Representative linear fits for surface pressure measurements. (a) concentration-dependence curve for leucine at pH 1 (no salt). (b) surface pressure as a function of NaCl concentration for 65 millimolal leucine solutions at pH 1. For both, data points reflect the average of triplicate measurements and error bars show one standard deviation.

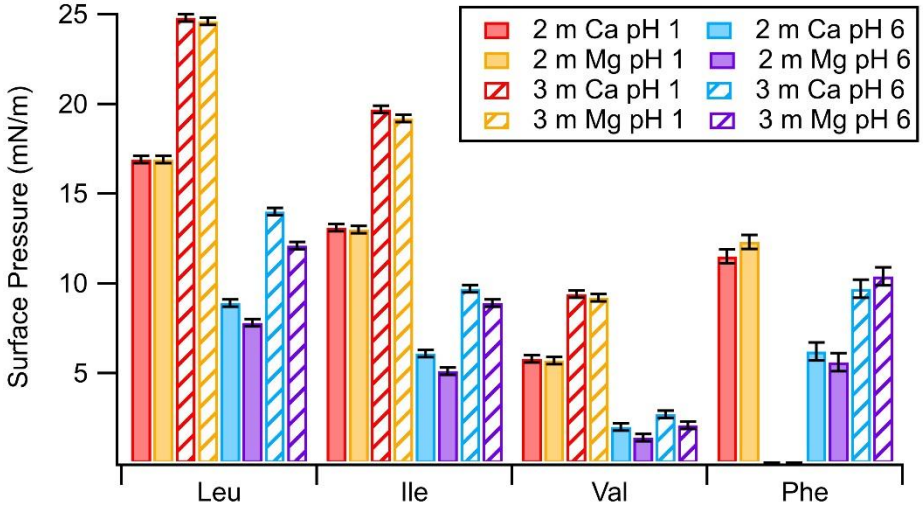

Figure 7.5: Comparison of surface pressure measurements for $CaCl_2$ and $MgCl_2$ solutions. At pH 1, the identity of the cation appears to have little impact on surface pressure. At pH 6, solutions of $CaCl_2$ exhibit greater surface pressure than solutions of $MgCl_2$ for the branched chain amino acids. Error bars show one standard deviation of multiple trials. The 3 m pH 1 Phe solutions could not be measured due to insolubility.

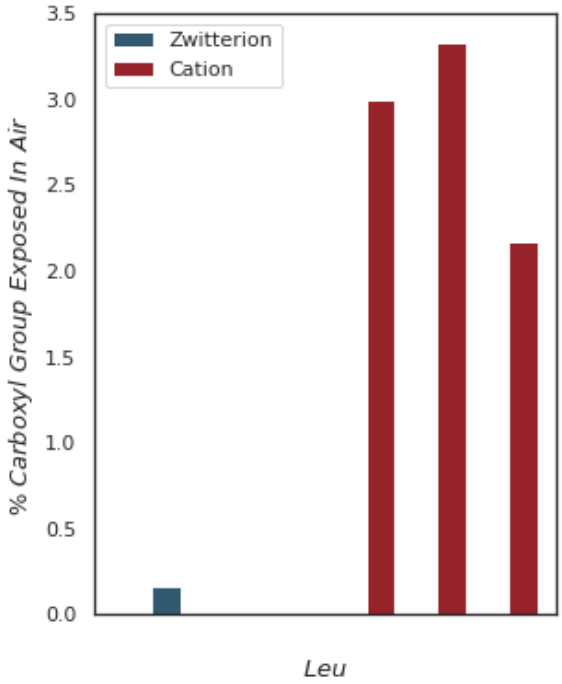

Figure 7.6: Comparison of carboxyl group orientation for zwitterion and cation Leu simulations. To determine if the carboxyl group was in the air, the average height of the two O atoms in the group was determined and compared to the average height of the O atoms of the water molecules. If this value was greater than 2.6 nm, the carboxyl group was assumed to be in the air. To eliminate frames where the amine group was also in the air, frames were excluded if the difference between the nitrogen atom height and the average water O atom height was greater than 2.6 nm. Using these rules, 2 out of 3 zwitterion simulations contained no frames where the carboxyl group was in the air and the amine was not, with the remaining replicate having a single frame satisfying these conditions. By contrast, there were 51 total frames where these conditions were met for the cation, showing that the COOH group is more likely to be in the air.

7.7 References

(1) Fuhrman, J. A.; Ferguson, R. L. Nanomolar Concentrations and Rapid Turnover of Dissolved Free Amino Acids in Seawater: Agreement between Chemical and Microbiological Measurements. *Mar. Ecol. Ser.* **1986**, *33*, 237–242.

(2) Hubberten, U.; Lara, R. J.; Kattner, G. Amino Acid Composition of Seawater and Dissolved Humic Substances in the Greenland Sea. *Mar. Chem.* **1994**, *45* (1–2), 121–128.

(3) Barbaro, E.; Zangrando, R.; Moret, I.; Barbante, C.; Cescon, P.; Gambaro, A. Free Amino Acids in Atmospheric Particulate Matter of Venice, Italy. *Atmos. Environ.* **2011**, *45* (28), 5050–5057.

(4) Triesch, N.; Van Pinxteren, M.; Engel, A.; Herrmann, H. Concerted Measurements of Free

Amino Acids at the Cabo Verde Islands: High Enrichments in Submicron Sea Spray Aerosol Particles and Cloud Droplets. *Atmos. Chem. Phys.* **2021**, *21* (1), 163–181.

(5) Triesch, N.; Van Pinxteren, M.; Salter, M.; Stolle, C.; Pereira, R.; Zieger, P.; Herrmann, H. Sea Spray Aerosol Chamber Study on Selective Transfer and Enrichment of Free and Combined Amino Acids. *ACS Earth Sp. Chem.* **2021**, *5* (6), 1564–1574.

(6) Cochran, R. E.; Jayarathne, T.; Stone, E. A.; Grassian, V. H. Selectivity across the Interface: A Test of Surface Activity in the Composition of Organic-Enriched Aerosols from Bubble Bursting. *J. Phys. Chem. Lett.* **2016**, *7* (9), 1692–1696.

(7) Luo, Q.; Hong, J.; Xu, H.; Han, S.; Tan, H.; Wang, Q.; Tao, J.; Ma, N.; Cheng, Y.; Su, H. Hygroscopicity of Amino Acids and Their Effect on the Water Uptake of Ammonium Sulfate in the Mixed Aerosol Particles. *Sci. Total Environ.* **2020**, *734*, 139318–139327.

(8) Liu, J.; Liu, L.; Rong, H.; Zhang, X. The Potential Mechanism of Atmospheric New Particle Formation Involving Amino Acids with Multiple Functional Groups. *Phys. Chem. Chem. Phys.* **2021**, *23* (17), 10184–10195.

(9) Angle, K. J.; Crocker, D. R.; Simpson, R. M. C.; Mayer, K. J.; Garofalo, L. A.; Moore, A. N.; Mora Garcia, S. L.; Or, V. W.; Srinivasan, S.; Farhan, M.; Sauer, J. S.; Lee, C.; Pothier, M. A.; Farmer, D. K.; Martz, T. R.; Bertram, T. H.; Cappa, C. D.; Prather, K. A.; Grassian, V. H. Acidity across the Interface from the Ocean Surface to Sea Spray Aerosol. *Proc. Natl. Acad. Sci.* **2020**, *118* (2), e2018397118.

(10) Keene, W. C.; Pszenny, A. A. P.; Maben, J. R.; Sander, R. Variation of Marine Aerosol Acidity with Particle Size. *Geophys. Res. Lett.* **2002**, *29* (7), 5.1-5.4.

(11) Bertram, T. H.; Cochran, R. E.; Grassian, V. H.; Stone, E. A. Sea Spray Aerosol Chemical Composition: Elemental and Molecular Mimics for Laboratory Studies of Heterogeneous and Multiphase Reactions. *Chem. Soc. Rev.* **2018**, *47* (7), 2374–2400.

(12) Salter, M. E.; Hamacher-Barth, E.; Leck, C.; Werner, J.; Johnson, C. M.; Riipinen, I.; Nilsson, E. D.; Zieger, P. Calcium Enrichment in Sea Spray Aerosol Particles. *Geophys. Res. Lett.* **2016**, *43* (15), 8277–8285.

(13) Jayarathne, T.; Sultana, C. M.; Lee, C.; Malfatti, F.; Cox, J. L.; Pendergraft, M. A.; Moore, K. A.; Azam, F.; Tivanski, A. V.; Cappa, C. D.; Bertram, T. H.; Grassian, V. H.; Prather, K. A.; Stone, E. A. Enrichment of Saccharides and Divalent Cations in Sea Spray Aerosol During Two Phytoplankton Blooms. *Environ. Sci. Technol.* **2016**, *50* (21), 11511–11520.

(14) Herboth, R.; Gopakumar, G.; Caleman, C.; Wohlert, M. Charge State Dependence of Amino Acid Propensity at Water Surface: Mechanisms Elucidated by Molecular Dynamics Simulations. *J. Phys. Chem. A* **2021**, *125* (22), 4705–4714.

(15) Li, Y.; Shrestha, M.; Luo, M.; Sit, I.; Song, M.; Grassian, V. H.; Xiong, W. Salting Up of Proteins at the Air/Water Interface. *Langmuir* **2019**, *35* (43), 13815–13820.

(16) Lindman, S.; Xue, W. F.; Szczepankiewicz, O.; Bauer, M. C.; Nilsson, H.; Linse, S. Salting the Charged Surface: pH and Salt Dependence of Protein G B1 Stability. *Biophys. J.* **2006**, *90* (8), 2911–2921.

(17) Yuan, G.; Kienzle, P. A.; Satija, S. K. Salting Up and Salting Down of Bovine Serum Albumin Layers at the Air–Water Interface. *Langmuir* **2020**, *36* (50), 15240–15246.

(18) Nguyen, Q. T.; Kjær, K. H.; Kling, K. I.; Boesen, T.; Bilde, M. Impact of Fatty Acid Coating on the CCN Activity of Sea Salt Particles. *Tellus B Chem. Phys. Meteorol.* **2017**, *69* (1), 1304064–1304078.

(19) Ovadnevaite, J.; Zuend, A.; Laaksonen, A.; Sanchez, K. J.; Roberts, G.; Ceburnis, D.; Decesari, S.; Rinaldi, M.; Hodas, N.; Facchini, M. C.; Seinfeld, J. H.; O' Dowd, C. Surface Tension Prevails over Solute Effect in Organic-Influenced Cloud Droplet Activation. *Nature* **2017**, *546* (7660), 637–641.

(20) Zhang, C.; Bu, L.; Fan, F.; Ma, N.; Wang, Y.; Yang, Y.; Größ, J.; Yan, J.; Wiedensohler, A. Surfactant Effect on the Hygroscopicity of Aerosol Particles at Relative Humidity Ranging from 80% to 99.5%: Internally Mixed Adipic Acid-Ammonium Sulfate Particles. *Atmos. Environ.* **2021**, 118725–118736.

(21) Ordoubadi, M.; Gregson, F. K. A.; Wang, H.; Carrigy, N. B.; Nicholas, M.; Gracin, S.; Lechuga-Ballesteros, D.; Reid, J. P.; Finlay, W. H.; Vehring, R. Trileucine as a Dispersibility Enhancer of Spray-Dried Inhalable Microparticles. *J. Control. Release* **2021**, *336*, 522–536.

(22) Sereda, T. J.; Mant, C. T.; Sönnichsen, F. D.; Hodges, R. S. Reversed-Phase Chromatography of Synthetic Amphipathic Alpha-Helical Peptides as a Model for Ligand/Receptor Interactions. Effect of Changing Hydrophobic Environment on the Relative Hydrophilicity/Hydrophobicity of Amino Acid Side-Chains. *J. Chromatogr. A* **1994**, *676* (1), 139–153.

(23) Armesto, X. L.; Canle L., M.; Fernández, M. I.; García, M. V.; Santaballa, J. A. First Steps in the Oxidation of Sulfur-Containing Amino Acids by Hypohalogenation: Very Fast Generation of Intermediate Sulfenyl Halides and Halosulfonium Cations. *Tetrahedron* **2000**, *56* (8), 1103–1109.

(24) Properties of Amino Acids. In *CRC Handbook of Chemistry and Physics*; Rumble, J. R., Ed.; Taylor and Francis Ltd.: Boca Raton, FL, 2021.

(25) Costanza, J.; Arshadi, M.; Abriola, L. M.; Pennell, K. D. Accumulation of PFOA and PFOS at the Air−Water Interface. *Environ. Sci. Technol. Lett* **2019**, *6*, 487–491.

(26) Luo, M.; Wauer, N. A.; Angle, K. J.; Dommer, A. C.; Song, M.; Nowak, C. M.; Amaro, R. E.; Grassian, V. H. Insights into the Behavior of Nonanoic Acid and Its Conjugate Base at the Air/Water Interface through a Combined Experimental and Theoretical Approach. *Chem. Sci.* **2020**, *11* (39), 10647–10656.

(27) Chodzińska, A.; Zdziennicka, A.; Jańczuk, B. Volumetric and Surface Properties of Short Chain Alcohols in Aqueous Solution–Air Systems at 293 K. *J. Solution Chem.* **2012**, *41* (12), 2226–2245.

(28) Bretti, C.; Giuffrè, O.; Lando, G.; Sammartano, S. Modeling Solubility and Acid–Base Properties of Some Amino Acids in Aqueous NaCl and $(CH_3)_4NCl$ Aqueous Solutions at Different Ionic Strengths and Temperatures. *Springerplus* **2016**, *5* (1), 1–21.

(29) Petelska, A. D.; Naumowicz, M.; Figaszewski, Z. A. The Equilibrium of Phosphatidylcholine–Amino Acid System in Monolayer at the Air/Water Interface. *Cell Biochem. Biophys.* **2010**, *60* (3), 155–160.

(30) Perkins, R. J.; Kukharchuk, A.; Delcroix, P.; Shoemaker, R. K.; Roeselová, M.; Cwiklik, L.; Vaida, V. The Partitioning of Small Aromatic Molecules to Air–Water and Phospholipid Interfaces Mediated by Non-Hydrophobic Interactions. *J. Phys. Chem. B* **2016**, *120* (30), 7408–7422.

(31) Griffith, E. C.; Vaida, V. Ionization State of L-Phenylalanine at the Air–Water Interface. *J. Am. Chem. Soc.* **2013**, *135* (2), 710–716.

(32) Qazi, M. J.; Schlegel, S. J.; Backus, E. H. G.; Bonn, M.; Bonn, D.; Shahidzadeh, N. Dynamic Surface Tension of Surfactants in the Presence of High Salt Concentrations. *Langmuir* **2020**, *36* (27), 7956–7964.

(33) Tang, N.; Skibsted, L. H. Calcium Binding to Amino Acids and Small Glycine Peptides in Aqueous Solution: Toward Peptide Design for Better Calcium Bioavailability. *J. Agric. Food Chem.* **2016**, *64* (21), 4376–4389.

(34) Mocellin, A.; Gomes, A. H. de A.; Araújo, O. C.; Brito, A. N. de; Björneholm, O. Surface Propensity of Atmospherically Relevant Amino Acids Studied by XPS. *J. Phys. Chem. B* **2017**, *121* (16), 4220–4225.

(35) Carter-Fenk, K. A.; Carter-Fenk, K.; Fiamingo, M. E.; Allen, H. C.; Herbert, J. M. Vibrational Exciton Delocalization Precludes the Use of Infrared Intensities as Proxies for Surfactant Accumulation on Aqueous Surfaces. *Chem. Sci.* **2021**, *12* (24), 8320–8332.

(36) Lambert, J.-F.; Sodupe, M.; Ugliengo, P.; Danger, G. G.; Plasson, R.; Pascal, R. Pathways for the Formation and Evolution of Peptides in Prebiotic Environments. *Chem. Soc. Rev.* **2012**, *41* (16), 5416–5429.

(37) Griffith, E. C.; Vaida, V. In Situ Observation of Peptide Bond Formation at the Water-Air Interface. *Proc. Natl. Acad. Sci.* **2012**, *109* (39), 15697–15701.

(38) Marsh, A.; Miles, R. E. H.; Rovelli, G.; Cowling, A. G.; Nandy, L.; Dutcher, C. S.; Reid, J. P. Influence of Organic Compound Functionality on Aerosol Hygroscopicity: Dicarboxylic Acids, Alkyl-Substituents, Sugars and Amino Acids. *Atmos. Chem. Phys.* **2017**, *17* (9), 5583–5599.

(39) Saha, A.; SenGupta, S.; Kumar, A.; Naik, P. D. Interaction of L-Phenylalanine with Lipid Monolayers at Air–Water Interface at Different pHs: Sum-Frequency Generation Spectroscopy and Surface Pressure Studies. *J. Phys. Chem. C* **2018**, *122* (7), 3875–3884.

(40) Angle, K. J.; Nowak, C. M.; Davasam, A.; Dommer, A. C.; Wauer, N. A.; Amaro, R. E.; Grassian, V. H. Amino Acids Are Driven to the Interface by Salts and Acidic Environments. *J. Phys. Chem. Lett.* **2022**, *13* (12), 2824–2829.

CHAPTER 8 CONCLUSIONS AND FUTURE PERSPECTIVES

8.1 Conclusions

Aqueous aerosols are unique and atmospherically ubiquitous reaction sites. The combination of large surface area to volume ratios, high ionic strength conditions, and possibility of chemical gradients give aerosols distinct properties from bulk solutions. Among the many important characteristics of these particles, pH is particularly important as it controls the health impacts, climate interactions, and chemical reaction rates associated with the aerosol. Although direct measurement of pH is challenging, recent innovations in colorimetric and spectroscopic methods as well as improvements to thermodynamic models have increased the practicality of assessing the acidity of aqueous aerosols.

In Chapter 3, the acidity of fresh sea spray aerosols (SSA) was discussed. Within two minutes of emission from the ocean, SSA can be acidified by four to six orders of magnitude. One factor contributing to this acidification is titration by acidic gases. Since individual SSA volume is on the order of femtoliters to picoliters, part-per-billion levels of gases are sufficient to lower SSA pH substantially as the aerosols travel through the air. A potential source of these acidic gases is HCl generated from other SSA (as discussed in Chapter 6), where organic acids "react" with NaCl to produce HCl. This is not a zero sum, as the organic acids typically have pK_a values > 2, indicating they ordinarily would not dissociate at submicron SSA pH levels. A second source of acidity could be the enhanced dissociation of other organic acids, such as fatty acids, when Na^+ or other cations compete with H^+ to bind with the organic anion. This hypothesis was reinforced in Chapter 7, where data showed interactions with cations impacts the surface propensity of amino acids, indicating organic anion to inorganic cation interactions may be strong under the right

conditions. Finally, the decrease in RH that SSA experience after emission from the sea surface further concentrates these existing acid sources, lowering particle pH. Overall, this chapter closed the knowledge gap on the acidity of nascent SSA, which were inaccessible to field studies due to the mixing of fresh and aged SSA in the environment.

In Chapter 4, the rate of aqueous S(IV) oxidation was measured in both the bulk and aerosol phases. This reaction both has pH dependence and, depending on the S(IV) source, can change the pH of the medium in which the reaction occurs. It was revealed that under a wide range of conditions the reaction is 1-2 orders of magnitude faster in aerosols compared to the bulk. Analysis of aerosol enrichment was critical in producing a fair comparison between these phases, underscoring the importance of enrichment for calculations of rate enhancement. In this case, increased salt concentrations generally lowered the reaction rate, making it even more striking that S(IV) oxidation is accelerated in aerosols. The rate enhancement was thus attributed to surface access and the distribution of species within the aerosol. Based on diffusion calculations, reagents in the aerosol can sample the surface dozens of times before reacting, while the majority of bulk reagents do not have the opportunity to sample the surface even once. The propensity of reacting radicals for the interface while inhibiting ions preferentially accumulate in the bulk is also likely an important phenomenon that warrants future study. Regardless of the cause of oxidation acceleration, this chapter adds another piece to the puzzle of determining why larger than expected sulfate formation is observed in megacities during pollution events and provides evidence of reaction acceleration in aqueous aerosols.

In Chapter 5, a new type of titration based on the partitioning of organic acids was introduced. When acid is added to an aerosol containing the conjugate bases of volatile organic acids, rather than lowering the pH, the acid can protonate these bases and cause a decrease in

organic fraction while pH remains constant. Whether this occurs in a given part of the atmosphere would depend on the concentration of the organic acids in the surrounding atmosphere and the rate of evaporation of the acids from aerosols. Lactic acid was used as a model system for studying this phenomenon, allowing exploration of the impacts of salt and organic concentration on evaporation rate. It was found that high organic concentrations decrease evaporation rate by changing the particle viscosity. This is a key insight, as evaporation is a first-order process and hence the rate constant would typically be inferred as independent of initial concentration. These assumptions come from bulk kinetics of dilute systems, however, while aerosols can be highly concentrated. It was also found that, despite the fact that adding NaCl increases aerosol viscosity, adding NaCl actually increases the evaporation rate. This is due to salting out, where inorganic ions outcompete organic molecules for hydration in highly concentrated systems. Once again, this chapter points to the importance of considering aerosols as non-ideal matrices where molecular interactions are distinctly different from low concentration bulk systems.

In Chapter 6, attention was turned to inorganic acids that also can partition from aqueous aerosols. Despite the fact that HCl and HNO_3 are strong acids, there have been numerous observations of chloride and nitrate depletion from both real world and laboratory generated aerosols. They key mechanism is the volatility of the acids, which thermodynamically drives them into the gas phase. The rates of depletion processes, however, have scarcely been studied. Thus, this chapter introduced a new approach of using glycine as a non-evaporating in-situ pH probe for continuous aerosol pH measurement. This allowed measurement of chloride depletion, which previously was elusive due to the absence of a Raman signal for chloride, and the approach also complimented the tracking of nitrate depletion via the nitrate Raman band. It was found that chloride depletion is an order of magnitude faster than nitrate depletion. In addition, the rates of

both processes were considerably slower than diffusion-limited predictions, indicating that the rate is controlled by the transient formation of HCl or HNO_3 near the air-water interface.

In Chapter 7, the impact of pH and salts on the surface propensity of amino acids was examined. Amino acids can be enriched from the ocean into SSA by several orders of magnitude, but whether they subsequently reside at the air-water interface or in the core of the SSA particle remained unknown. A combination of experiments and simulations revealed that salts drive hydrophobic amino acids to the air-water interface, both in the cation and zwitterion form. The surface propensity was greater at lower pH and with higher salt concentrations. These factors thus synergize with conditions typical of an aerosol losing water due to a decrease in RH, implying that greater surface activity may be expected over time as an SSA travels through the atmosphere. The simulations also gave insight into amino acid orientation at the air-water interface, revealing that the COOH group may reside in the air while the COO^- group rarely does so. These findings agreed with experiments showing that the identity of the salt cation is important at neutral, but not highly acidic, pH, probably due to interaction with the carboxylic functional group. In conclusion, low pH and divalent cation salts can push even amino acids with shorter chain side groups to the interface, where they may impact aerosol morphology or participate in heterogeneous atmospheric chemistry.

The above findings may be combined and presented from the perspective of an individual SSA particle. The SSA is created from a bursting bubble, launching water from the ocean (including the sea surface microlayer) that had an initial pH near 8 into the atmosphere. Immediately, the SSA begins interacting with trace acidic gases as it travels through the atmosphere, and as it travels farther from the sea surface, it loses water as it occupies a lower RH environment. Within a few minutes, the SSA has changed noticeably from its source waters,

having a lower pH and becoming significantly more concentrated. This decrease in pH and increase in salt concentration begins to drive species such as amino acids to the air-water interface. Simultaneously, any small conjugate bases that have been protonated to form neutral acids have diffused rapidly inside the aerosol, with a significant fraction partitioning out of the SSA. Despite the initial rapid drop in pH, the acidity of the SSA now remains constant for hours, as multiphase buffering and chloride depletion prevent excessive accumulation of acid. While acidic, several chemical reactions may happen either within or on the surface of the SSA, including oxidation of SO_2. After days, the chloride content is largely depleted, but the aerosol continues accommodating trace acidic gases, and eventually the pH drops further, potentially below 0. The SSA is now one of billions of microscopic, highly acidic particles produced from a massive alkaline body of ocean water. The final fate of this particular SSA is uncertain. It may be inhaled, serve as a cloud seed, coalesce with another aerosol, deposit onto land, or return to the sea.

8.2 Future Perspectives

Many aspects of aerosol chemistry warrant further study. While further measures of aerosol pH may be insightful, it will be important to remember that two different techniques may measure different phenomena despite both calling them "pH". Indeed, there is no guarantee that two arbitrary chemical compositions that cause the same Raman spectral signatures of an acid-base pair will cause a paper of indicator dyes to turn the same color. There is also no guarantee that experiments and thermodynamic models measure the same property, as the former more frequently is representative of sample reactivity or speciation, while the latter essentially measures ion and molecule activity. Additional development of thermodynamic models to incorporate inorganic depletion and zwitterions may be useful in some cases. Improvements have been suggested over time for the PSC formulation.[1] Given how widely these models are used, renewed attention to the

determination of activity coefficients using modern analytical tools may be useful in improving understanding of molecular interactions in highly concentrated solutions. Ultimately, careful analysis of aerosol pH can shed light on atmospheric chemistry and the extent to which emission controls can be effective in mitigating air quality problems from pollution.[2]

Reaction acceleration is another topic that warrants additional, careful research, in part due to current controversies. The extent of an electric field at an air-water interface, and the degree to which this field can generate hydroxyl radicals or assist redox chemistry, will be important to constrain to improve understanding of the ubiquitous air-water interface.[3] Equilibrium assumptions may be invalid for aerosols, which are metastable with respect to their surroundings, but kinetics remain important in assessing the speed of chemical reactions in the atmosphere as well as potentially in industrial applications. Timescales are also important in understanding virus viability and how indoor chemistry impacts human health.

One class of reactions that may yield useful insights is the hydrolysis of esters. Given that the reaction involves an ester and water as the reagents, the inputs into the aerosol phase can be constrained more readily compared to reactions that require two enrichment factors to be managed. In addition, ester hydrolysis can exhibit acid- and base-catalyzed behavior.[4,5] Hydrolysis could thus be switched "on" and "off" via a series of titrations. The products of the ester are smaller and hence more volatile, assuming they remain uncharged. Therefore, like aerosol-phase organic base titration, ester hydrolysis is a reaction that could lead to a decrease in organic fraction over time as the products partition out of the aerosol into the surrounding atmosphere.

More generally, reactions with differing surface propensity of reactants versus products may shed light on the importance of surface sampling for aerosol kinetics. If the reactants have a significantly greater surface propensity or hydrophobicity, they may be softly confined to the outer

layer of the particle, increasing their effective concentration, while products disperse throughout the aerosol core. Conversely, if the reactants have significantly less surface propensity, the reaction may not initially be noticeably accelerated within error, but the products could be removed through evaporation (via surface heating if necessary), thus removing products and by Le Chatelier's principle continuously driving the reaction forward.

For as long as the sea sprays and organisms exhale, aqueous aerosols will abound. The silent worlds inside each of these aerosols present both mystery and opportunity for exploration.

8.3 References

(1) Zaveri, R. A.; Easter, R. C.; Wexler, A. S. A New Method for Multicomponent Activity Coefficients of Electrolytes in Aqueous Atmospheric Aerosols. *J. Geophys. Res. Atmos.* **2005**, *110* (D2), 1–23.

(2) Zhou, M.; Zheng, G.; Wang, H.; Qiao, L.; Zhu, S.; Huang, D.; An, J.; Lou, S.; Tao, S.; Wang, Q.; Yan, R.; Ma, Y.; Chen, C.; Cheng, Y.; Su, H.; Huang, C. Long-Term Trends and Drivers of Aerosol pH in Eastern China. *Atmos. Chem. Phys* **2022**, *22*, 13833–13844.

(3) Xing, D.; Yuan, X.; Liang, C.; Jin, T.; Zhang, S.; Zhang, X. Spontaneous Oxidation of I^- in Water Microdroplets and Its Atmospheric Implications. *Chem. Commun.* **2022**.

(4) Pierce, O. R.; Gorin, G. Acid-Catalyzed Hydrolysis of Ethyl Acetate. *J. Am. Chem. Soc.* **1953**, *75* (7), 1749–1750.

(5) Tsujikawa, H.; Inoue, H. The Reaction Rate of the Alkaline Hydrolysis of Ethyl Acetate. *Bull. Chem. Soc. Jpn.* **1966**, *39* (9), 1837–1842.

APPENDIX A: PROGRAMS USED FOR DATA ANALYSIS

The following MATLAB (Mathworks, version R2019B) codes were used to assist with data analysis. Since many of the projects were collaborative, the priority of the programs was ease of explanation to a newcomer to the project, rather than using the fewest lines of code or maximizing computational efficiency. No tools exclusive to MATLAB are used, so the reader should be able to recreate these programs in other coding languages if necessary. Note that routine use frequently does *not* require all sections of the programs to be run. Therefore, the reader is encouraged to determine what each section of the program does before beginning. Readily usable versions of these programs as MATLAB (.m) and text (.txt) files are available at this link: https://drive.google.com/drive/folders/13Kv1gOW6O4rssegZqoiiQk1WFQ54dH9W

Confocal Intensity Collecting

The aim of this program is to collect all output data from the confocal Raman spectrometer for analysis. The files should be in order; if they are not in order, then program 9.1.2 or something similar should be used instead. Note that the initialization of the *intensities* variable as "intensities = zeros(9260, length(myFiles));" is written with a hard-coded number of rows to decrease the chance that the results are pasted into an Excel template with mismatching wavenumbers. If spectra were collected across a different Raman range or with a different groove setting, this number will need to be changed accordingly.

AOT Kinetics

The aim of this program is to collect all Raman spectra from the Aerosol Optical Tweezers 100 (Biral, Inc.) and perform background subtraction, baseline correction, and averaging to assist with kinetics calculations. An example of default AOT output is "2022-04-20-Fri_1", for the first

file, “2022-04-20-Fri_2” for the second file, and so on. As a result, some sorting algorithms would place the 10th file before the 2nd file due to the “1” digit coming before the “2”. To fix this, files for the command “natsortfiles” were downloaded from the internet and added to the MATLAB path, and the reader would also need to do this for the program to work as intended.

AOT Refractive Index and Radius Calculator

The aim of this program is to help the user visualize the data contained in the "Results_full" file that is generated by the AOT, ultimately allowing a reasonable determination of the refractive index and radius of an aerosol for a given range of time.

AOT Molality Solver

The aim of this program is to calculate aerosol-phase molality from refractive index data. Note that the refractive index should be at the correct wavelength; if data is at a different wavelength, it may be converted as described in Chapter 5. The calculator works best for an aerosol composed of a single binary salt. When more components are present, rather than a single solution, there will be a set of solutions described by a line, or a plane, etc. Therefore, independent measures of concentration are needed for all but one component. Even in the case of a single binary salt, the equations have no analytical solution. Thus, the program checks physically realistic concentrations in small steps and keeps the solution with the least error.

Whispering Gallery Mode Removal

The aim of this program is to assist in the detection and removal of Whispering Gallery Modes (WGMs, also called Mie resonances) from AOT data and fit the resulting data to a line. As an optically-trapped aerosol changes size, the WGMs change location on the Raman spectra. This results in frequent overlaps with analyte peaks. Therefore, a graph of analyte peak area vs time will have positive outliers corresponding to these overlap events. This program searches for

positive outliers and can remove them from the data. There are several parameters that can be tuned based on the concentration of the analyte in the aerosol. Note that there is no guarantee every possible combination of parameters will result in proper removal of WGMs. Therefore, it is recommended the user visualize the outliers being removed and check against the actual spectra, such as by using the LARA OFFLINE software (Biral), if there is uncertainty.

Automatic Peak Fitting for Igor

The aim of this program is to generate commands to fit peaks to Gaussian curves in the program Igor (Wavemetrics). The dissertation author found Igor's peak fitting to be robust and useful for visually demonstrating to others how peaks were fit. Igor commands are typed in a separate language, however, not learned by the majority of collaborators. Therefore, the solution applied here is to use MATLAB to generate commands that can be copy-pasted into Igor. While there are more efficient ways to perform this task, the individual steps here may help those new to this procedure to see what is being done. Note that these commands are valid for Igor version 8. Updates to Igor may result in a more user-friendly automatic peak fitting environment within Igor, making this MATLAB program obsolete. Note also that it would be impractical to list every possible combination of constraints in the "Generating constraints" section. Thus, a few examples have been provided, and the reader is reminded that peak location and intensity can vary with matrix effects such as concentrations, ionic strength, and pH.

RH Calculator for Environmental Cell

The aim of this program is to calculate the real relative humidity inside the environmental cell associated with the confocal Raman spectrometer based on the cell temperature and dew point as reported by the in-line hygrometer. The constants in the program were determined empirically and may need to be changed for instruments in other labs.

Automatic Confocal Spectral Acquisition

The aim of this program is to allow automatic acquisition of spectra at defined time intervals for a non-internet-connected computer. The program starts a cycle where it moves the mouse to a particular location on the screen and clicks at defined time intervals. The position should be adjusted to the location the user desires to click. The recommended usage is to set the cycle to occur a very large number of times, then use CTRL+C to interrupt the loop when enough data has been obtained and the user desires the clicking to reach the end.